Tampere University

Muhammad Huzaifa Awais

ATOMIC LAYER DEPOSITION OF TITANIUM DIOXIDE ON ACTIVATED CARBON FOR NEGATIVE ELECTRODE IN SUPERCAPACITOR

Faculty of Engineering and Natural Sciences
Master's Thesis
December 2025

ABSTRACT

Muhammad Huzaifa Awais: Atomic Layer Deposition of Titanium Dioxide on Activated Carbon for negative electrode in supercapacitor
Master's Thesis
Tampere University
Materials Science and Engineering
December 2025

Supercapacitors have emerged as a critical energy storage technology due to their high-power density, rapid charge-discharge capabilities, and long cycle life. However, their energy density remains a limiting factor for widespread application. To address this, researchers have explored advanced electrode materials, particularly carbon-based structures such as graphene, carbon nanotubes, and activated carbon (AC). To enhance capacitance and stability, these carbon structures have been modified with metal oxides. Titanium dioxide (TiO_2) has gained attention due to its pseudocapacitive behavior and chemical stability. Atomic layer deposition (ALD) offers a precise and conformal method for depositing TiO_2 on porous carbon substrates, enabling controlled modification of electrochemical properties. This thesis focuses on the synthesis of TiO_2-coated AC via ALD on industrially available YP-80F carbon (Kuraray) for application as a negative electrode in supercapacitors. The study aims to investigate the influence of ALD parameters (such as deposition temperature and number of cycles) on the electrochemical performance of TiO_2-coated AC electrodes. The resulting TiO_2-AC electrodes are then evaluated against unmodified YP-80F using cyclic voltammetry, galvanostatic charge-discharge, and capacitance retention tests. Subsequently, different material characterization techniques (FESEM, EDX, XRD, Raman spectroscopy, and ellipsometry) are employed to investigate the structure and morphology of the fabricated electrodes and ALD

Based on the work conducted, the electrochemical improvement provided by ALD TiO_2 coating was minimal. In device configuration, the best-performing sample (140°C–40 Cycles) showed only a 4.5% increase in specific capacitance (27.9 F/g) compared to bare YP-80F (26.7 F/g), while three-electrode CV revealed an 18.3% improvement for the 100°C-10 Cycles sample (89.9 F/g versus 76.0 F/g for bare AC). Capacitance retention improved marginally from 95.7% for bare AC to 101.3% for 100°C-10 Cycles and 97.8% for 120°C-40 Cycles after 10,000 cycles. EDX weight percentage results showed a successful ALD operation, but without confirming coating conformality or morphology. Raman and XRD analyses indicated the deposited TiO_2 was amorphous. Thus, this work tentatively suggests that TiO_2 ALD provides only minimal performance enhancement. However, this cannot be considered an established conclusion due to insufficient sample replication, inconsistent electrochemical testing conditions, and limited advanced structural characterization.

Keywords: Supercapacitor, Atomic Layer Deposition, Titanium Dioxide, Activated Carbon

USE OF AI IN THESIS

I have utilised AI tools in my thesis:

☐ No
☒ Yes

The AI tools utilised in my thesis and their purposes are described below:

Names and versions of AI tools: MS Copilot, Litemaps, Quillbot

Purpose of using AI tools: Litemaps was used for literature review. Quillbot and MS CoPilot were used for paraphrasing purposes

Sections where AI tools were used: Litemaps was used in Chapter 2 and 3. Quillbot and MS CoPilot were used in every chapter except Chapter 4, 5 and 6.

I acknowledge that I am fully responsible for the entire content of my thesis, including the parts generated by AI, and accept accountability for any violations of ethical standards in publications.

PREFACE

This thesis has been conducted as a part of ARMS project funded by the European Commission's Horizon Europe programme, is part of the Graphene Flagship initiative which works to advance technologies that rely on graphene and other 2D materials. Part of the research uses Research Council of Finland Research Infrastructure 'Printed Intelligence Infrastructure' (PII-FIRI, Grant Number 358618). The experimental work for the thesis has been carried out using the infrastructure of Tampere University Laboratory for Future Electronics (LFE). I extend my gratitude to Dr. Hamed Pourkheirollah for his supervision, conceptualization, and administration of the work, as well as for his guidance in methodology, validation, and resources. I also wish to extend my sincere thanks to Prof. Matti Mäntysalo for his examination and provision of resources, and for his critical review. My appreciation also goes to all project partners and my colleagues at LFE for their involvement and assistance. I would also like to thank Mr. Isaac Remuel M. Vitto for his guidance in improving my research techniques in the laboratory.

Finally, I would like to express my deepest gratitude to my parents and my sister, Noor Fatima, for their unwavering support and encouragement in every stage of life.

Tampere, December 2025

Muhammad Huzaifa Awais

CONTENTS

LIST OF FIGURES

LIST OF SYMBOLS AND ABBREVIATIONS

Abbreviation	Full Form
AC	Activated Carbon
ALD	Atomic Layer Deposition
BET	Brunauer–Emmett–Teller (surface area analysis)
BJH	Barrett–Joyner–Halenda (pore size distribution
CMC	Carboxymethyl Cellulose
CNT	Carbon Nanotube
CV	Cyclic Voltammetry
DI	Deionized (water)
EDLC	Electric Double-Layer Capacitor
EDX	Energy-Dispersive X-ray Spectroscopy
EIS	Electrochemical impedance spectroscopy
ESR	Equivalent Series Resistance
FESEM	Field Emission Scanning Electron Microscopy
GCD	Galvanostatic Charge–Discharge
GCS	Gouy-Chapman-Stern (model)
GIXRD	Grazing-Incidence X-ray Diffraction
GPC	Growth Per Cycle
GO	Graphene Oxide
HK	Horvath–Kawazoe (pore size method)
HR-TEM	High-Resolution Transmission Electron Microscopy
IHP	Inner Helmholtz Plane
OHP	Outer Helmholtz Plane
OLC	Onion-like carbons
PET	Polyethylene Terephthalate

SEI	Solid-electrolyte interphase
SPR	Styrene–Butadiene Rubber
SC	Supercapacitor
TMO	Transition Metal Oxide
XPS	X-ray Photoelectron Spectroscopy
XRD	X-ray Diffraction

Symbol	Description
A	Area (m^2)
Å	Ångstrom (0.1 nm)
C	Capacitance (F)
C_s	Specific capacitance (F/g)
C_0	Total double-layer capacitance
C_{stern}	Stern layer capacitance
C_D	Diffuse layer capacitance
E	Energy (J)
H	Radius of solvated ions (m)
ID/IG	Intensity ratio of D-band to G-band
M	Mass of active material (g)
N	Order of reflection
P	Power density (W/kg)
Q	Specific capacity (mAh/g)
r_p	Reflection coefficient for p-polarization
r_s	Reflection coefficient for s-polarization
T	Time (s)
V	Voltage (V)
ΔV	Voltage window (V)

V	Scan rate (mV/s)
ε_0	Vacuum permittivity (F/m)
ε_r	Relative permittivity
Θ	Angle (degrees)
Ψ	Ellipsometry amplitude ratio
Δ	Ellipsometry phase shift
P	Ratio of reflection coefficients

1. INTRODUCTION

The global transition toward renewable energy sources and the proliferation of portable electronics, electric vehicles, and grid-scale storage systems have intensified the demand for advanced energy storage technologies that deliver both high power and high energy density [1], [2], [3]. Among electrochemical energy storage systems, supercapacitors have emerged as a critical bridging technology, offering exceptional power densities (1-10 kW/kg) [4], ultrafast charge–discharge capabilities, and long cyclability (>10^5) [5]. For industrial applications demanding long-term reliability, including self-powered WSNs, energy-autonomous IoT devices, and flexible wearable electronics, supercapacitors (SCs) have emerged as the preferred energy storage solution [6], [7], [8].

The electrochemical performance of supercapacitors is fundamentally governed by electrode architecture and the nature of charge storage mechanisms. Electric double-layer capacitors (EDLCs), the most common supercapacitor type, rely on the electrostatic separation of charges at the electrode–electrolyte interface. This physical adsorption process, while enabling rapid energy delivery and exceptional reversibility, is inherently limited by the available surface area and the interfacial capacitance. [9]

Activated carbons (AC) have become the most common electrode material of choice for EDLCs due to its large specific surface area, hierarchical pore structure, good electrical conductivity, chemical resistivity to various electrolytes and cost-effectiveness [10]. YP-80F is a commercial, coconut-shell derived AC and the industry standard for high-performance EDLCs, designed for higher power capabilities while exhibiting excellent performance, reliability, and stable quality in aqueous symmetric supercapacitors [11], [12]. Nevertheless, the purely electrostatic nature of charge storage in AC-based EDLCs imposes a limitation on energy density that cannot be overcome through structural optimization alone [13]. The functional groups on AC can also promote detrimental side reactions with the electrolyte, resulting in capacity loss, increased leakage current, and a limited voltage window [14].

To overcome this limitation in AC-based supercapacitors, approaches center around introducing Faradaic reactions to increase energy storage. This involves integrating pseudocapacitive materials like metal oxides, into the carbon framework, along with functionalization for improved wettability [15]. Pseudocapacitance, unlike EDLC, arises from

fast and reversible Faradaic redox reactions at or near the electrode surface. Pseudocapacitors can exhibit a capacitance 10–100 times greater than that of EDLCs. The combination of Faradaic processes with EDL charging significantly boosts an electrode's specific capacitance. [16]

Transition metal oxides (TMOs) represent a particularly promising class of pseudocapacitive materials, offering multiple oxidation states that enable efficient electron transfer and proton-coupled charge storage mechanisms [17]. Among TMOs, titanium dioxide (TiO_2) has garnered significant attention for supercapacitor applications due to its natural abundance, low toxicity, exceptional chemical stability [18], and versatile pseudocapacitive behavior rooted in the Ti^{4+}/Ti^{3+} redox couple [19], [20]. The ability to fabricate TiO_2 in various nanostructural forms 0D nanoparticles [21], 1D nanotubes [22], 2D nanosheets [23], and 3D composites [24] further enhances its adaptability to diverse electrode designs.

However, the practical application of TMOs is severely limited by intrinsic issues, primarily their low electrical conductivity. This creates hurdles for charge carrier exchange between the electrode and electrolyte restricts electron transfer rates, and results in low power density. Furthermore, TMOs suffer from poor cyclability caused by structural instability, particle swelling, agglomeration, and morphological degradation during charge-discharge cycles. [25] [26]

To overcome these limitations, a common strategy is to integrate TMOs with conductive carbon substrates [27]. Research has concentrated on utilizing high-porosity, three-dimensional (3D) carbon nanostructures like AC. By depositing TMOs onto these frameworks, the electrode-electrolyte interfacial area is enlarged and ion diffusion paths are shortened, enabling rapid charge diffusion and transportation [28]. However, conventional TMO deposition methods often lead to non-uniform dispersions, poor interfacial contact, and excessive material loading, while thick oxide layers can block ion pathways within the porous carbon network, counterproductively reducing the accessible surface area [29] [30]. These issues highlight the need for precise control over oxide deposition, both in terms of thickness and conformality, to achieve the optimum effect where the carbon scaffold provides rapid electron transport and the ultrathin oxide contributes pseudocapacitance without impeding ion diffusion or blocking pores.

Atomic layer deposition (ALD) has emerged as an exceptional thin-film deposition technology due to its Angstrom-scale thickness control and perfectly uniform, conformal coatings on complex 3D structures [31]. For supercapacitor electrodes, this means the deep pores of a high-surface-area carbon substrate can be uniformly coated with an

ultra-thin, continuous oxide layer. This precision could enable exact tuning of the pseudocapacitive material, optimizing the balance between added charge storage and the preservation of the carbon's intrinsic double-layer capacity.

While ALD has proven highly successful in enhancing energy storage materials by widening voltage windows with dielectric coatings and boosting capacitance with pseudocapacitive oxides [32], the systematic exploration of ALD-TiO_2 on industrially relevant, commercial ACs remains limited. Further investigation is needed to understand how ALD parameters affect coating properties and electrochemical performance within these complex porous structures. Initial work by Vitto et al. reported on the development of an ALD process for TiO_2 on porous AC and investigated the influence of precursor pulse duration and film thickness on deposition behavior within the AC structure [33]. However, their study evaluated the performance of TiO_2 in positive voltage window with symmetric supercapacitor configurations.

Building upon this foundation, this research aims to extend the investigation by examining the performance of the TiO_2-AC composite as a negative electrode. To systematically explore this application, the study examines key ALD parameters, i.e. deposition temperature and number of cycles, and comprehensively evaluates the resulting morphological, structural, and electrochemical properties. Critically, the composite is tested in asymmetric supercapacitor devices, contrasting with the symmetric configurations previously used. This research is motivated by the hypothesis that ultrathin, conformal TiO_2 coatings can enhance the electrochemical performance of commercial activated carbon electrodes by adding pseudocapacitance. The findings aim to contribute to the development of high-performance, cost-effective, printed, and flexible supercapacitors.

1.1 Aim and scope of the thesis

This thesis is conducted as a part of the ARMS project (Atomic layer-coated gRaphene electrode-based Micro-flexible and Structural supercapacitors), which aims to develop eco-friendly supercapacitors with energy densities exceeding 50 Wh/kg by integrating graphene-rich bio-based carbon materials with ultrathin ALD technology. Accordingly, this thesis focuses on ALD-TiO_2 coatings on the commercial AC YP-80F for use as a negative electrode in asymmetric SCs. To guide this investigation, the following research questions are addressed:

- Does the ALD-deposited TiO_2 coating contribute pseudocapacitance to the AC electrode?

- How does the electrochemical performance of the ALD-modified TiO_2-AC electrodes compare to that of pristine AC, and what are the optimal ALD parameters for performance enhancement?
- What are the structural and morphological changes induced by varying the number of ALD cycles and the deposition temperature on the YP-80F, and how do these changes affect the electrochemical performance of the resulting TiO_2-AC composite?

To answer these questions, this work is structured around four interconnected aims:

1. **Synthesis and Fabrication:** Systematically vary key ALD parameters, i.e. temperature and number of cycles, to produce a series of coated samples for comprehensive analysis.
2. **Electrochemical Characterization:** Test the electrodes in three-electrode and two-electrode asymmetric configurations to measure key performance metrics, including specific capacitance, charge storage behaviour, cyclic stability, and impedances.
3. **Material Characterization:** Analyse the synthesized composites Raman spectroscopy, X-Ray Diffraction (XRD), ellipsometry (TiO_2 thickness), Field Emission Scanning Electron Microscopy (FESEM), and Energy-Dispersive X-Ray spectroscopy (EDX) to quantify the impact of ALD on the carbon substrate and coating properties.
4. **Data Analysis and Interpretation:** Integrate and analyse all experimental data to determine optimal deposition conditions and to establish a coherent explanation linking ALD process parameters, material properties, and electrochemical performance.

Guided by these aims, this thesis works to answer the proposed research questions and understand the structure-performance relationship for ALD-deposited TiO_2-AC electrodes, with the expectation that TiO_2 will contribute pseudocapacitance to enhance overall charge storage while preserving the conductive carbon framework. By addressing these questions, this study aims to provide critical insights into the ALD engineering of metal oxide coatings on activated carbons; an underexplored topic, and to motivate further research into ALD-enhanced carbon composites for next-generation energy storage.

1.2 Structure of the thesis

This thesis begins with the introduction provided above. Chapter 2 outlines the relevant theoretical background, aiming to equip the reader with the necessary foundation to better understand the subsequent literature review and experimental analysis. The chapter first explains the working principles and charge storage mechanisms of supercapacitors. It then details the theory and operation of the characterization techniques used in this work. Chapter 3 constitutes the literature review, which systematically builds the research rationale. It progresses from a broad overview of carbon materials to a specific focus on ACs. The review then examines TMOs, narrowing down to TiO_2, before establishing the rationale for employing ALD. The chapter concludes with a survey of prior studies on using ALD to modify ACs for supercapacitor applications. Chapter 4 details the experimental methodology, including electrode ink formulation, pouch cell fabrication, and the characterization procedures and the characterization procedures. Chapter 5 presents the experimental results and discusses their interpretation. Chapter 6 provides the conclusions drawn from the research, critically reviews the limitations of the study and discusses potential improvements can be made, suggesting directions for future research.

2. FUNDAMENTALS AND CHARACTERIZATION THEORY

To meet the growing global demand for efficient and sustainable energy, advanced energy storage systems are increasingly critical. Among these, supercapacitors (or ultracapacitors) have gained prominence by bridging the gap between traditional capacitors and batteries, combining high power density, rapid charge-discharge capability, substantial energy storage, and exceptional cycle life [34]. Supercapacitors are mainly classified based on their charge-storage mechanisms, namely EDLC, pseudocapacitors, and then hybrid supercapacitors which are a combination of both mechanisms, as shown in Figure 1, along with the materials associated with each charge-storage mechanism.

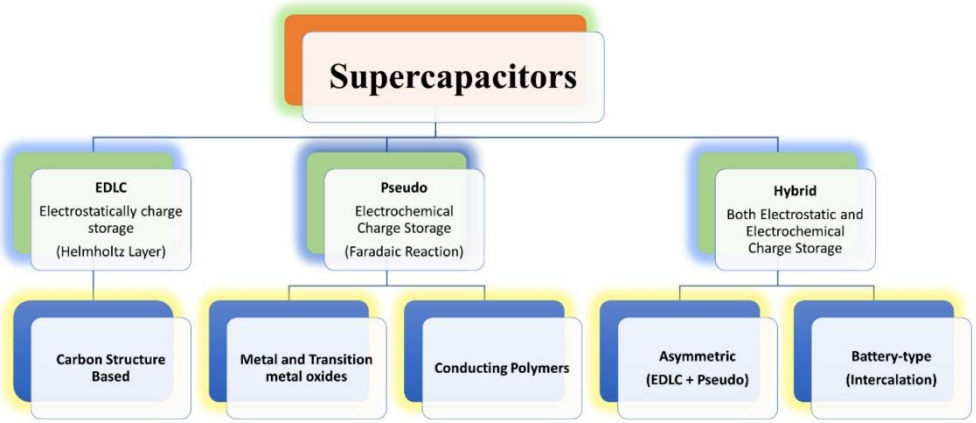

Figure 1. Classification of supercapacitors [35]

This chapter proceeds by describing these charge storage mechanisms. It then discusses the electrochemical evaluation techniques for supercapacitors, and finally describes the necessary material characterization techniques used to analyze their structural and morphological properties.

2.1 EDLC

Before discussing EDL phenomenon, it is important to understand the basic plate capacitor model, because all subsequent models for describing EDLC behavior are derived from this principle [36]. The simplest capacitor consists of two parallel conducting plates separated by a dielectric insulator. Applying a voltage accumulates opposite charges on the plates, creating a static electric field. Its capacitance (C), defined as the ratio of stored charge (Q) to applied voltage (V), is given by:

$$C = \frac{Q}{V} = \varepsilon_0 \varepsilon_r \frac{A}{d} \quad (1)$$

where ε_0 is the vacuum permittivity, ε_r is the dielectric's relative permittivity, A is the plate area, and d is their separation. This linear relationship between voltage and stored charge is a key characteristic for capacitive storage, as it does not hold valid for batteries and other energy storage systems [37]. This parallel-plate model also assumes A >> d and negligible fringing fields. The stored energy is:

$$E = \frac{1}{2} CV^2 \quad (2)$$

Similarly, EDLCs store energy electrostatically at the electrode/electrolyte interface. Electrolyte ions with a charge opposite to the electrode are attracted to its surface, while those with the same charge are repelled, forming two distinct, parallel charge layers separated by a nanometer-thick solvent-based dielectric [38], [39], [40], [41]. Unlike traditional capacitors however, EDLCs achieve significantly higher energy storage due to two factors: the extremely small separation between these charge layers and the use of porous, high-surface-area electrode materials that provide a greater number of charge storage sites [42].

The first and simplest model describing the EDL was proposed by Hermann von Helmholtz (Figure 2a) in 1853 to originally explain the distribution of charges at colloid interfaces [36]. It was later adapted for electrode interfaces [36]. It precisely postulates that the charges on the electrode side are balanced by a dense layer of counter-ions on the electrolyte side. Thus, compact layer of electrolyte ions forms adjacent to the electrode surface. It also proposes a linear decay of electric potential across this electrode-electrolyte interface, and that its areal capacitance (also called the Stern layer capacitance) is determined solely by the electrolyte's dielectric constant and the effective charge separation distance [36]. The equation for Stern layer capacitance is given below:

$$C_{Stern} = \frac{\varepsilon_0 \varepsilon_r}{H} \quad (3)$$

where H is the radius of the solvated ions.

The Helmholtz model was later understood to have neglected the influence of thermal motion, as described by Boltzmann statistics, and this lead to an incorrect assumption that the ions in the electrolyte are static. Gouy [37] addressed this by incorporating a thermal fluctuation factor into the double-layer theory. In this refined model (Figure 2b), ions were treated as point charges forming a three-dimensional, diffuse cloud in the electrolyte. This diffuse region holds a net charge equal and opposite to the excess electronic charge on the electrode surface. However, the Gouy model itself overestimated the total

capacitance due to an inaccurate representation of the potential profile in the immediate vicinity of the electrode/electrolyte interface.

Stern resolved this overestimation issue in 1924 by unifying the earlier Helmholtz and Gouy-Chapman theories [37]. He proposed that the electrode–electrolyte interface consists of two distinct regions: an inner layer in which finite-sized ions adsorb according to Langmuir's isotherm, forming a compact layer similar to Helmholtz's model, and an outer region where ions form a diffuse cloud described by the Gouy-Chapman theory [36], [37]. This integration, known as the Gouy-Chapman-Stern (GCS) model (Figure 2c), is the basis of the modern understanding of the electrical double layer [43]. In the GCS model, the total interfacial capacitance is the series combination of the compact Stern layer capacitance and the diffuse layer capacitance. The thickness of the diffuse layer is determined by the Debye length, a critical parameter that decreases with higher electrolyte concentration. The total capacitance in the double−layer is therefore a combination of two capacitances in series, as given by the following equation:

$$\frac{1}{C_O} = \frac{1}{C_{Stern}} + \frac{1}{C_D} \tag{4}$$

where C_O is the total capacitance, C_{Stern} is the Helmholtz compact layer capacitance diffusive capacitance C_D. Figure 2 illustrates the three conventional EDL models, namely Helmholtz, Gouy-Chapman, and the GCS models.

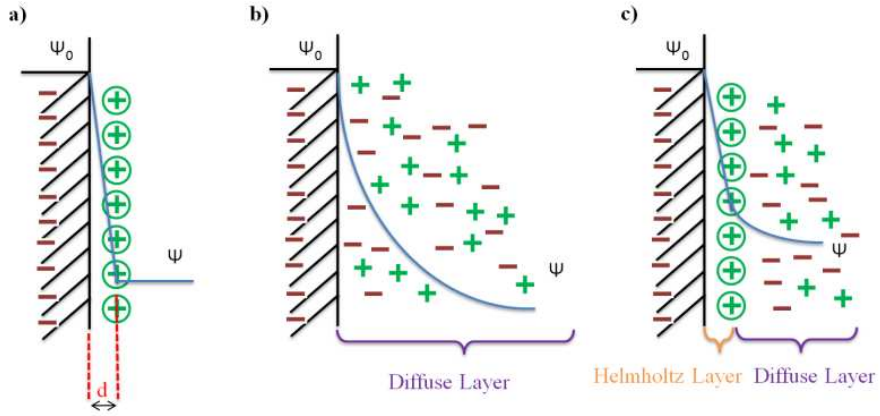

Figure 2. Models of the electrical double layer at a negatively-charged surface: (a) Helm-holtz model with the atomic distance d representing the double-layer, (b) Gouy-Chapman model and (c) Gouy-Chapman-Stern model combining both models. Ψ0 is the total surface potential. [36]

The separation between the compact Helmholtz layer and the diffuse layer can be described by the closest distance that ions in the electrolyte can approach the electrode surface [43]. Grahame further distinguished two planes within the interfacial region (Figure 3), the inner Helmholtz plane (IHP) and the outer Helmholtz plane (OHP), which

correspond to the different minimum approach distances of cations and anions [44]. Anions have smaller distances of approach as compared to hydrated cations, resulting inner-layer capacitances at positively charged electrodes being twice those at negatively charged electrodes. Grahame also showed that some ions can partially lose their solvation shells and penetrate beyond the Stern layer to adsorb specifically at the IHP. These specifically adsorbed ions can participate in faradaic charge-transfer reactions, giving rise to pseudocapacitance, discussed in the next section. In Grahame's model, similar to the GCS model, the electric potential drops linearly across the Stern region (OHP) and decays exponentially through the diffuse layer beyond it.

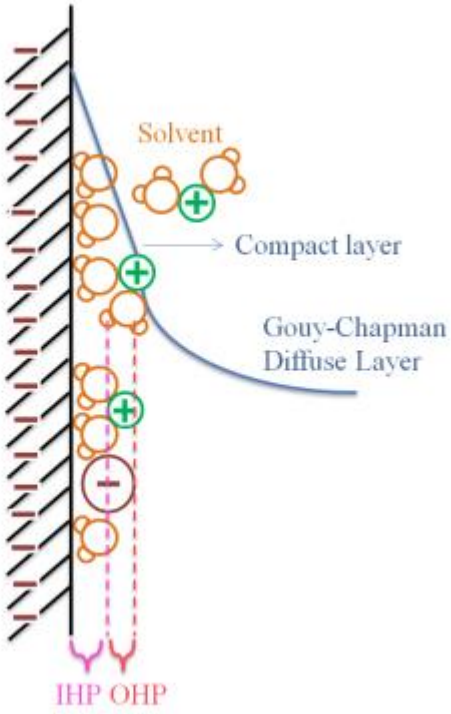

Figure 3. Grahame's model of the electrical double layer, depicting the inner compact layer and the outer Gouy-Chapman diffuse layer in an electrolyte. [36]

2.2 Pseudocapacitors

Pseudocapacitors are energy storage systems that operate through two complementary mechanisms. The first involves fast and reversible redox reactions occurring at or near the electrode–electrolyte interface, enabling efficient charge transfer. The second mechanism is based on ionic separation within the electrolyte and their accumulation on the electrode surface. Because pseudocapacitors combine faradaic redox activity with electrostatic ion separation, they generally achieve much higher capacitance than EDLCs.

Overall charge storage in pseudocapacitors primarily occurs through three processes: underpotential deposition, redox reactions, and ion intercalation. [35]

Underpotential deposition (UPD) refers to the formation of a monolayer of metal atoms on a substrate at a potential higher than the Nernst Potential of that substrate [45]. UPD has several applications, including measurement of the metal surface area [46], [47], [48], analysis of metal traces via stripping voltammetry and biosensor development [35].

Redox reactions involve electron transfer between species and are central to pseudocapacitive charge storage. These processes typically involve the electrochemical adsorption of cations onto oxidized electrode surfaces, accompanied by faradaic charge transfer. The capacitance associated with redox mechanisms can be analyzed by considering the variable oxidation states of transition-metal oxides. [49]

Intercalation involves the insertion of ions from the electrolyte into the pores or layered structure of an active material. While the underlying chemistry is similar to redox reactions, intercalation is distinguished by its rapid ion diffusion kinetics. Although commonly associated with battery-type charge storage, intercalation can also contribute to pseudocapacitive behavior. Ion insertion may follow either intrinsic or extrinsic pathways. At reduced dimensions, the shortened pathways for ion and electron transport enable behavior that transitions from battery-like to pseudocapacitive. [49] [50]

Together, these three mechanisms, visually illustrated in Figure 4, enable pseudocapacitors to achieve enhanced charge storage performance compared with purely electrostatic EDLCs.

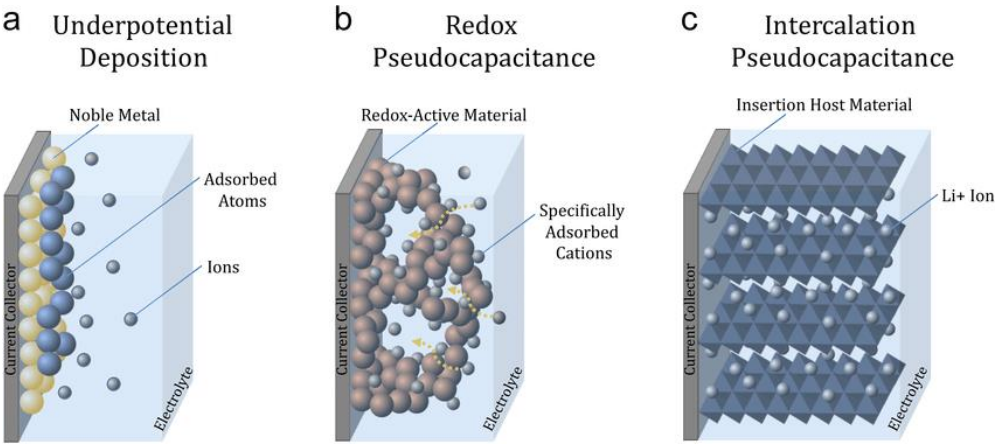

Figure 4. The three primary pseudocapacitive charge storage mechanisms: (a) underpotential deposition, (b) redox pseudocapacitance, and (c) intercalation pseudocapacitance. [51]

2.3 Hybrid supercapacitors

Hybrid supercapacitors were developed to overcome the inherent limitations of pure EDLCs and pseudocapacitors by integrating their two distinct charge storage mechanisms into a single system. They can be categorized into two categories: asymmetric supercapacitors and battery-type hybrid supercapacitors. [35]

Asymmetric supercapacitors integrate one EDLC-type electrode with one pseudocapacitive electrode, creating a synergistic system that enhances both energy and power density while extending cycle life. [35]

Battery-type hybrid supercapacitors consist of two electrodes with distinct charge storage mechanisms; faradaic intercalation in one battery-type electrode and surface ion adsorption on the other capacitive electrode. This dual-mechanism design not only boosts energy density but also improves cycle stability and mitigates current fluctuation effects. [35]

2.4 Materials used for supercapacitor

The choice of materials for supercapacitor manufacturing depends on the device's functional requirements and application objectives. Supercapacitors consist of several essential components: electrodes, electrolytes, separators, current collectors, and supporting substrates (Figure 5). [52]

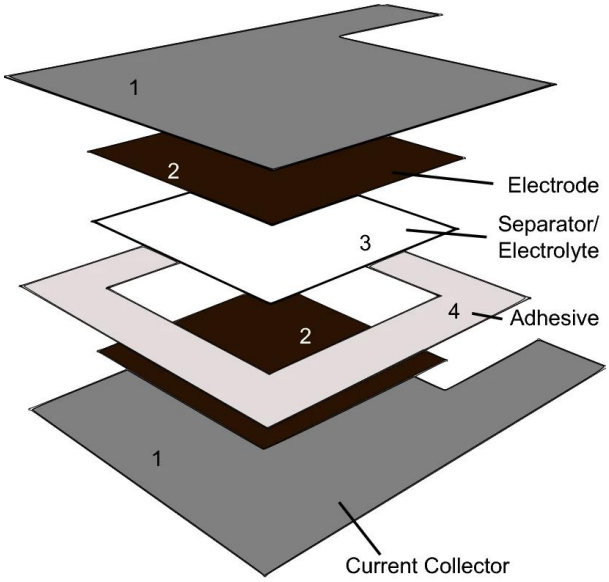

Figure 5. Schematic of a pouch cell supercapacitor, showing its components. [53]

2.4.1 Electrodes

The electrochemical performance of supercapacitor electrodes is governed by their material composition, which directly determines their specific capacitance [54]. When voltage is applied, interfacial charge-storage phenomena (detailed in Sections 2.1 and 2.2) become active at the electrode surface [55]. To optimize performance, electrodes require engineered attributes for example a mesoporous pore structure, high accessible surface area, wide stability windows, electrolyte compatibility, and good conductivity. [56] [57]

Nanostructured electrode materials have emerged as particularly promising candidates due to their exceptional conductivity and enhanced ion adsorption capabilities stemming from their dramatically increased surface-to-volume ratios [58]. The precise control of pore architecture in these nanomaterials represents a crucial design paremater. They must remain sufficiently large to accommodate electrolyte ion transport without causing excessive material densification. Overly constricted pores may compromise ion accessibility and increase resistive losses, while excessively large pores reduce active site density. [59]

For EDLCs, carbon-based materials are preferred due to their stability and non-reactivity, which preserve electrostatic charge storage. Optimal pore sizes are ~0.7 nm in aqueous and ~0.8 nm in organic electrolytes [60]. A balanced hierarchical porous structure, typically containing 20–50% mesopores for rapid ion transport, abundant micropores for high charge storage, and sufficient macropores as ion highways, enables high energy and power densities [61].

Among carbon materials, activated carbon is the most widely used due to its exceptionally high specific surface area, which arises from its hierarchical porous structure containing micropores (< 20 Å), mesopores (20–500 Å), and macropores (>500 Å) [62], [63], [64]. Other notable carbon nanostructures include onion-like carbons (OLCs), carbon nanotubes (CNTs), and graphene oxide (GO). The selection of ACs over other carbon materials will be further discussed in Section 3.1.

2.4.2 Electrolyte

Electrolytes are pivotal in determining the performance of supercapacitors, primarily by defining their energy density, operating voltage window (V), and equivalent series resistance (ESR). Key selection criteria for an optimal electrolyte include high ionic conductivity, a wide potential window, low viscosity, chemical stability, cost-effectiveness,

and environmental safety. Furthermore, the ionic size must be compatible with the electrode's pore structure to maximize capacitance, as smaller ions improve pore accessibility and charge storage. [65]

Effective dissociation of the electrolyte in its solvent is also essential to minimize internal resistance and optimize overall device performance. Among the various classes, aqueous electrolytes are often prioritized to their low viscosity and rapid ionic mobility, leading to superior energy storage characteristics. They are categorized into acidic, alkaline, and neutral electrolytes. [66]

Acidic electrolytes (e.g., H_2SO_4) and alkaline electrolytes (e.g., KOH) are widely employed in supercapacitors. They offer high specific capacitance and ionic conductivity. However, they are corrosive, which limits their cyclic stability. Their corrosive nature also prevents their use in high-voltage applications. [66]

Neutral electrolytes contain lower concentrations of H^+ and OH^- ions. This leads to a larger overpotential for hydrogen and oxygen evolution reactions. Consequently, neutral electrolytes possess a wider electrochemical stable potential window (ESPW). Na_2SO_4 is the most studied neutral electrolyte. [66]

Dawoud et al. showed that despite CNT/MnO_2 electrode achieving a higher specific capacitance (2523 F/g at 5 mV/s) in H_2SO_4, it had inferior cyclic stability performance when compared to the neutral Na_2SO_4 electrolyte. Using Na_2SO_4 electrolyte resulted in a higher capacitance retention (80% after 3000 cycles) than H_2SO_4, making Na_2SO_4 the more favorable choice for long-term, stable device. It was, however, noted that using H_2SO_4 provided with redox peaks, implying pseudocapacitance, unlike Na_2SO_4, which showed no redox peaks, implying an EDLC mechanism [67].

According to Peng et al. the Na_2SO_4 electrolyte offers a higher energy density than other aqueous electrolytes like H_2SO_4 and KOH due to its wider electrochemical potential window [68]. Table 1 lists additional research articles that similarly employ a 1 M Na_2SO_4 electrolyte for supercapacitor studies.

Table 1. Performance summary of supercapacitor electrodes from selected literature using 1 M Na_2SO_4 electrolyte.

Electrode	**Specific capacitance (F/g)**	**Measurement Conditions**	**Energy Density (Wh/kg)**	**Power Density (W/kg)**	**Ref**
V_2O_5@3DGraphene	612.5	-	54.9	898	[69]
Mn_2O_3/peach-like carbon	158.8	1.0 A/g Current density	-	-	[70]
Carbon package from recycled from spent Zn-Mn batteries	100	1.0 A/g Current density	17.8	503	[71]
Activated microporous polyacrylonitrile-based carbon nanofibers	103	1.0 A/g Current density	-	-	[72]

2.4.3 Separator

Separators are a vital component in supercapacitors, preventing short circuits while maintaining effective interfacial contact [73] [74] [75]. An ideal separator requires strong mechanical properties, thermal stability, uniform thickness, high porosity, excellent wettability, sufficient electrolyte storage, and minimal ionic resistance [76] [73]. A porous architecture is critical: macropores aid infiltration, while meso- and micropores shorten ion diffusion paths and reduce collisions, thereby improving performance [78]. Economically, the separator is the second most significant component after the electrolyte, accounting for ~26% of total device cost [79].

Cellulose is an ideal candidate due to its status as the most abundant renewable polymer, offering exceptional biocompatibility, high thermal stability, and inherent hydrophilicity [80]. Its flexibility, absorbency, and biodegradability enhance performance, sustainability, and cost-effectiveness, making it particularly suitable for flexible and wearable SCs [81]. Cellulose-based separators outperform conventional polymer separators, exhibiting porosity up to 75% and electrolyte uptake capacity as high as 300% [82] [83]. Figure

6 illustrates the molecular structure of cellulose, and key properties of cellulose separators.

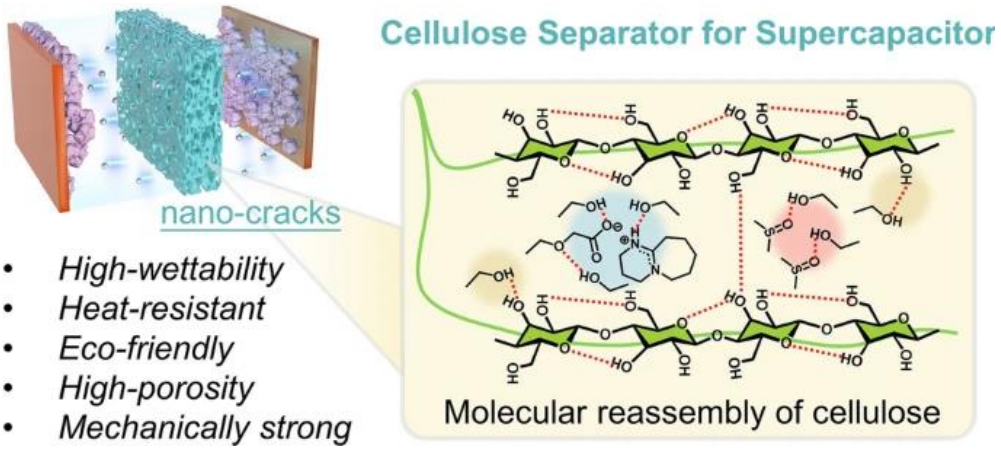

Figure 6. Properties of a cellulose-based supercapacitor separator. [81]

The commercial cellulose-based separators e.g. NKK-TF4030 [84], TF4040 [82], and Dynacap GT 0.45/40 [87] have already been used in supercapacitors as separators.

2.4.4 Current collector

The current collector serves as the crucial electrical interface between the electrode and external circuit, collecting electrons for efficient transfer [87]. Conventional supercapacitors use metallic current collectors, such as aluminum, nickel, copper, and stainless steel [88]. Their stability and conductivity directly influence cell performance [87]. An ideal collector must exhibit high electrical conductivity, excellent electrochemical and chemical stability in the electrolyte, favorable cost, low density, and ease of processing, with specific material requirements differing between aqueous and organic electrolytes [89].

Standard metal collectors have drawbacks, including corrosion susceptibility, high interfacial resistance, limited gravimetric energy density, and poor suitability for flexible devices [90] [91]. Carbon-based collectors offer a promising alternative, facilitating flexible device fabrication and reducing interfacial resistance with the active electrode material. [92] [93] [94]. However, their significantly higher electrical resistance compared to metals increases the ESR of the device, which remains a key challenge for their widespread adoption.

2.5 Printed supercapacitors

Printed electronics (PE) is an emerging field recognized for its effectiveness in fabricating microscale and nanoscale devices, offering distinct advantages over traditional methods

including simplicity, cost-effectiveness, material efficiency, versatility, eco-friendliness, and scalability for large-area, high-volume production [95]. This technology facilitates the fabrication of diverse supercapacitor architectures, such as micro, asymmetric, and flexible designs, on various flexible substrates. Scalable solution-based processes like coating and printing enable economical, large-area manufacturing of electronic components [96]. Printing is distinguished from coating by its ability to produce patterned, two-dimensional images [95], and techniques are broadly categorized as contact or non-contact (Figure 7), each with unique properties like line width and speed. The choice of method for SCs depends heavily on the required film thickness, as SCs typically need active layers on the order of tens of micrometers; commercial AC electrodes, for example, are often around 100 µm thick [97]. Among available techniques, screen printing is particularly suitable for producing the necessary thick (10–100 µm), patterned SC electrodes [98], making it a prominent and widely researched method in the field. [99] [100]

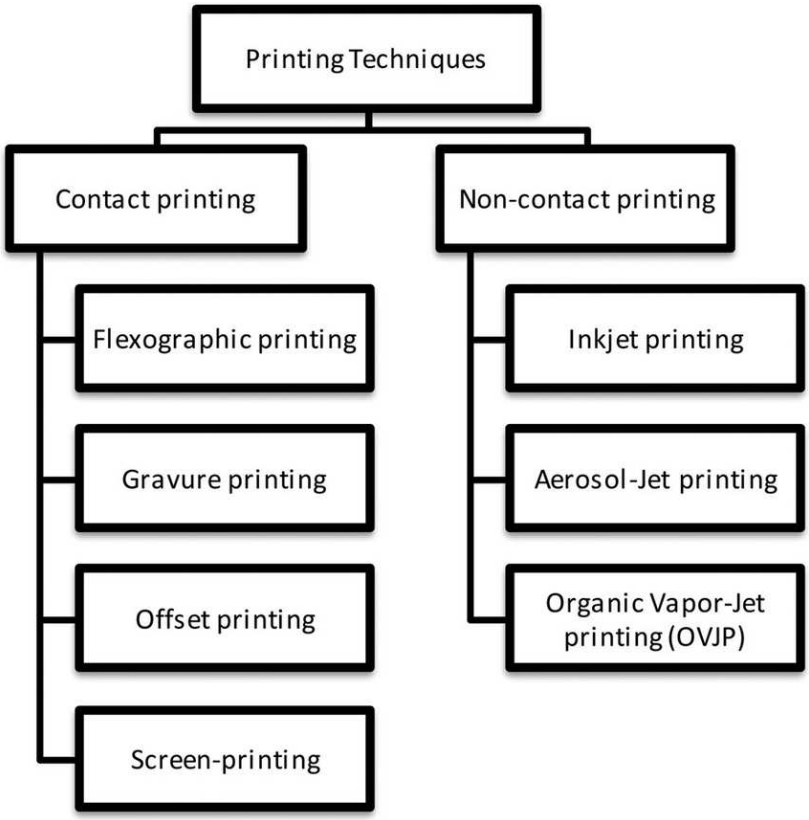

Figure 7. Classification of Printing Electronics [102]

2.5.1 Doctor blading

Blade coating, also known as doctor blade or knife coating, is a method used to deposit a uniform layer of material from a solution, typically achieving thicknesses around 100

µm [102] [103]. In this process, a sharp blade is set at a fixed height above a substrate, which can be either flexible or rigid. The coating solution is placed in front of the blade, which is then moved across the surface, as shown in Figure 8. This action then spreads the solution into a wet film. The final thickness of the film depends on several factors: the gap between the blade and the substrate, the speed at which the blade moves, and the flow properties (viscosity and elasticity) of the solution. [104]

For creating patterns, stencils can be used to guide the ink or paste onto specific areas of the surface [105]. Ideally, the process should waste very little solution (around 5%), but in practice, it can take time to adjust the conditions to reach this level of efficiency. To work well, the inks or pastes used must be quite thick, with viscosities often between 1000 and 10,000 mPa·s. This thickness is usually achieved by adding binders and thickeners, such as glycerol, ethylene glycol, or ethyl cellulose. [103] [106]

One of the biggest advantages of blade coating is its simplicity and low cost. The equipment is affordable and easy to operate, and small, lab-scale coaters are readily available for experiments. This makes it very useful for quickly preparing test electrodes by hand. However, the process is not without challenges. Because it is an open system, solvents can evaporate during coating, which may change the ink's consistency. Also, the flow of material under the blade is complex, and if the substrate is not perfectly even, it can be difficult to achieve a completely uniform film.

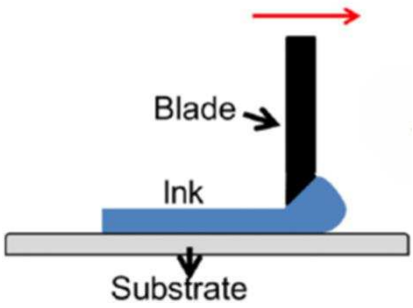

Figure 8. Doctor blading technique for fabricating printed electronics. The direction of motion of doctor blade is shown by the red arrow. [108]

2.6 Characterization techniques

Comprehensive supercapacitor evaluation requires both electrochemical and materials characterization to quantify energy storage behavior and correlate it with structural and compositional features. Understanding these characterization theories is essential for

accurate data interpretation and establishing reliable structure–property relationships in ALD-modified electrodes.

2.6.1 CV

CV is a fundamental electrochemical technique widely used to investigate the charge storage behavior and performance of supercapacitors. In CV, the potential applied to an electrochemical cell is swept linearly between two set voltage limits at a controlled rate, known as the scan rate, and then swept back to the initial potential, forming a cycle. The voltage limit is called voltage window. During this process, the resulting current is measured as a function of the applied voltage, producing a voltammogram that serves as a fingerprint of the electrochemical processes occurring at the electrode–electrolyte interface. [108]

The experimental setup for CV typically involves either a two-electrode or a three-electrode configuration. Key components of the three-electrode setup include the working electrode, an inert counter electrode, a stable reference electrode, and an electrolyte (Figure 9). The choice of cell configuration and materials directly influences the quality and interpretability of the CV data. [109]

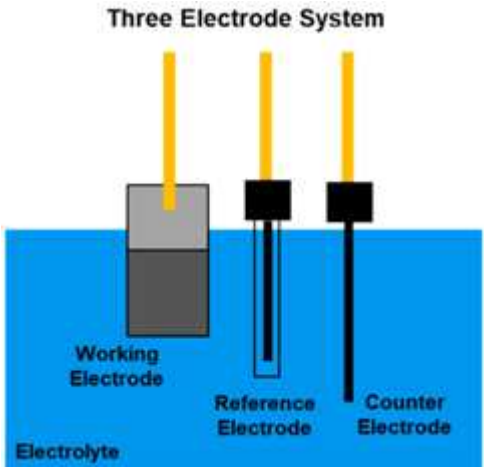

Figure 9. Standard three-electrode electrochemical cell configuration [110]

From the CV curve, several critical electrochemical properties can be extracted. The shape of the voltammogram reveals the dominant charge storage mechanism. A rectangular or box-like shape (Figure 10a) indicates ideal capacitive (non-Faradaic) behavior typical of EDLCs. A quasi-rectangular or leaf-like shape with broad humps (Figure 10b) suggests pseudocapacitive contributions from surface redox reactions, and well-defined oxidation and reduction peaks (Figure 10c) signify battery-like (Faradaic) processes. [109]

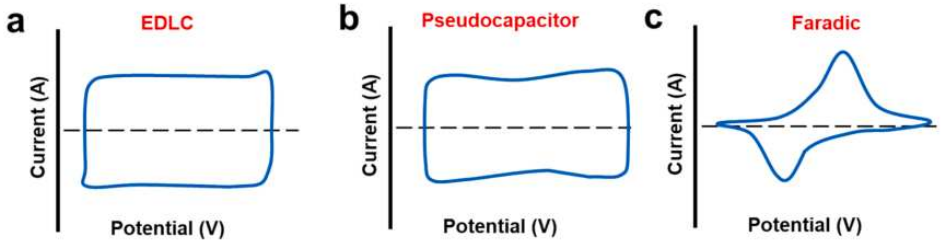

Figure 10. Cyclic Voltammograms for (a) EDLC, (b) pseudocapacitors and (c) battery-like supercapacitors [110]

Additionally, parameters such as specific capacitance or specific capacity can be calculated by integrating the area under the CV curve, while the dependence of peak current on scan rate provides insight into whether the charge storage is governed by surface adsorption or diffusion-controlled processes. Specific capacitance can be calculated using CV curves, using the formula below.

$$C_S = \frac{\int_{V_1}^{V_2} I(V)\, dV}{2mv(\Delta V)} \tag{5}$$

where Cs is the specific capacitance, the whole numerator is area enclosed by the CV curve, m is the mass of active material, ß 9is the voltage window and v is the scan rate. [110]

2.6.2 GCD

GCD is an electrochemical technique used to evaluate the performance of supercapacitors by applying a constant current to charge the device and then discharging it under the same or a symmetric current condition [106]. During GCD, the voltage response of the electrode or full cell is recorded over time, yielding characteristic charge–discharge profiles that reveal critical information about capacitance, internal resistance, coulombic efficiency, and energy–power characteristics. In ideal EDLCs, the GCD curves exhibit symmetrical, linear triangular shapes (Figure 11A), reflecting rapid, non-Faradaic ion adsorption/desorption at the electrode–electrolyte interface. In contrast, pseudocapacitive or battery-type electrodes display non-linear (Figure 11B) or plateau-like regions in the discharge curves, indicative of Faradaic redox reactions [112].

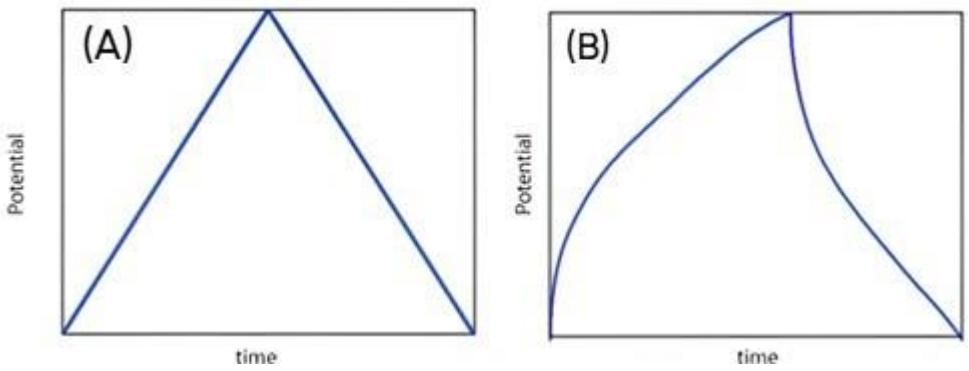

Figure 11. Typical GCD curves of (A) EDLC materials and (B) pseudocapacitive materials. [114]

The symmetry between charge and discharge times reflects the reversibility and efficiency of the electrochemical processes, while deviations can signal side reactions, polarization effects, or poor kinetics. Key parameters such as specific capacitance, specific capacity and power density are derived directly from the discharge time, applied current, and operational voltage window using the equations given below [115] [116].

$$C_s = \frac{It}{m(\Delta V)} \tag{6}$$

$$P = \frac{C(\Delta V)^2}{2t} \tag{7}$$

where I is the constant discharge current, C_s is the specific capacitance, P is the power density, t is the discharge time, ΔV is the operational voltage window, and m is the mass of active material.

GCD is particularly valuable for assessing real-world applicability because it mimics actual charge–discharge cycles, provides insight into cycling stability over thousands of repetitions, and helps identify undesirable effects like voltage drops (IR drop), which reflect internal resistance and kinetic limitations. It enables clear differentiation between storage contributions, validates reversibility, and guides electrode balancing in asymmetric or full-cell configurations, and complements cyclic voltammetry in the comprehensive electrochemical characterization of supercapacitors.

2.6.3 FESEM

The Field Emission Scanning Electron Microscope (FESEM) generates high-resolution surface images by scanning a focused electron beam over a sample. Its key component is a cold field emission (FE) gun, which uses a strong electrical field on a sharp tip to produce a brighter, smaller, and more coherent electron beam than the thermal filaments of conventional SEMs. The beam, focused by electromagnetic lenses to a diameter as

fine as 10 Å and steered in a raster pattern, interacts with the sample surface in a vacuum chamber. [117]

This interaction produces secondary electrons (SE) for high-resolution topographic imaging and backscattered electrons (BSE) (Figure 12) for atomic number-based compositional contrast. These signals are detected and converted into a pixel-based image, with magnification determined by the ratio of the display size to the scanned area.

The primary advantage of FESEM is its superior resolution, which enables magnifications up to 500,000× and a best secondary electron (SE) resolution of approximately 1.5 nm. A second major advantage is its capability to perform high-resolution imaging at very low accelerating voltages, typically as low as ~1 keV. This low-voltage capability is critical for examining non-conductive, volatile, or vacuum-sensitive materials, such as polymers and nanomaterials, without the need for a conductive coating [118]

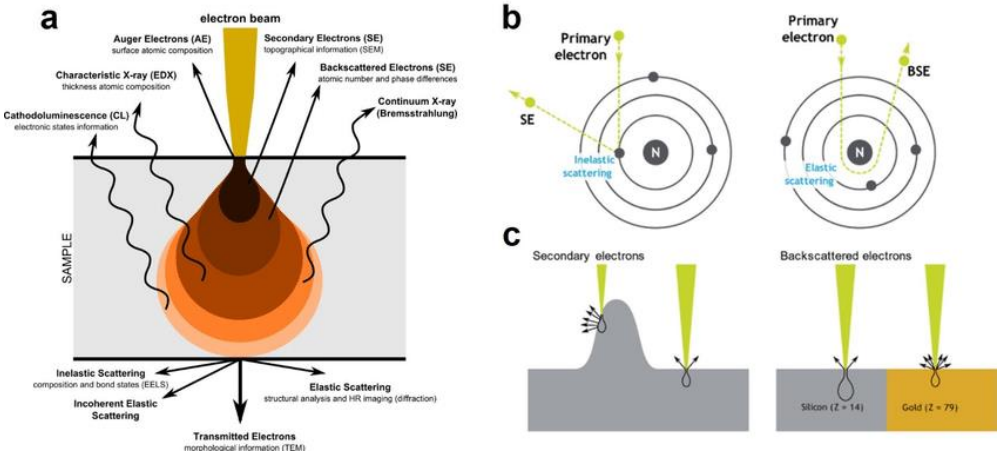

Figure 12. Signal generation in electron microscopy: (a) types of signals produced by electron beam interaction and their uses; (b, c) mechanisms of inelastic scattering (SE generation) and elastic scattering (BSE generation and atomic number contrast). [119]

Energy-dispersive X-ray spectroscopy (EDX) is conventionally integrated with field-emission scanning electron microscopy (FESEM) to provide morphological and elemental analysis. EDX results comprise characteristic X-ray spectra (Figure 12a) that reveal the elemental composition of sampled volumes, with peaks at specific energies corresponding to each detected element [120]. These data yield quantitative information on elemental presence, relative weight percentages, and spatial distribution through elemental mapping, thereby enabling assessment of material purity, stoichiometric ratios, and identification of contaminants or secondary phases. The detection limit and spatial resolution are influenced by factors including beam energy, sample thickness, and matrix effects, with results typically presented as both spectral plots quantified in weight and atomic percentages, and as color-coded maps showing elemental localization. [117]

2.6.4 Raman spectroscopy

Raman scattering is a phenomenon based on the inelastic scattering of monochromatic light, usually from a laser source, by molecules in a sample. When light interacts with molecular vibrations, rotations, or other low-frequency modes, most photons are elastically scattered (Rayleigh scattering) with no change in energy. However, a small fraction of photons exchange energy with the molecules, leading to a shift in the scattered light's frequency. If the photon loses energy to the molecule, it produces a Stokes line (lower energy), whereas if it gains energy from an already excited molecule, it results in an anti-Stokes line (higher energy). Figure 13 illustrates this Raman scattering phenomenon.

A Raman spectrum, which plots Raman Shift (cm^{-1}) against Intensity (a.u.), serves as a molecular fingerprint of the sample. The position of the peaks on the x-axis (Raman Shift) identifies specific molecular vibrations and functional groups, while the shape of these peaks reveals the structural order. Sharp peaks indicate a uniform, crystalline environment, and broad peaks signify disorder. In the context of carbon samples, this structural information is linked to defects within the two-dimensional carbon lattice, classified as zero-dimensional (0D, e.g., vacancies, dopants) or one-dimensional (1D, e.g., grain borders), which drive the transition from ordered carbon structures (e.g. pristine graphene) to disordered forms. [121]

The intensity ratio between the disorder-induced D band (~1350 cm^{-1}) and the crystalline G band (~1580 cm^{-1}), known as the ID/IG ratio, is a critical metric that quantifies this structural disorder. However, as in [122] we use the integrated intensity (peak area) ratio rather than the intensity ratio. This approach is preferred because the integrated area of a peak corresponds to the probability of the Raman scattering process occurring. Consequently, comparing these areas, rather than just peak heights, yields a better of defects, allowing for a clearer distinction between point-like and line-like defects. This ratio provides better insights into the density of defects, the size of crystalline domains, and the presence of functional groups that break the symmetry of the perfect sp^2 carbon lattice. Thus, by analyzing peak positions, shapes, and the ID/IG ratio, Raman spectroscopy provides a picture of a carbon material's chemical structure, defect density, and crystallinity. [122]

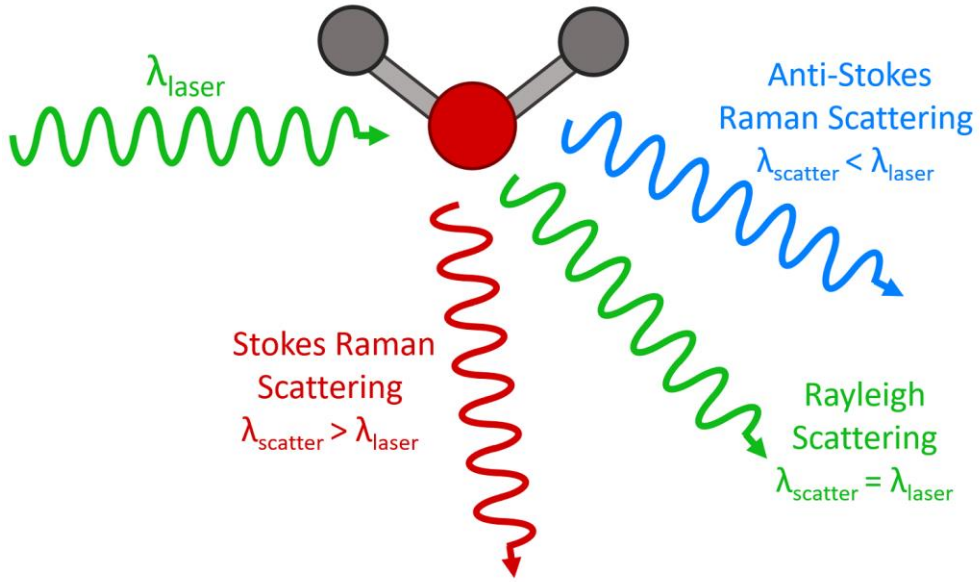

Figure 13. Schematic illustrating the principle of Raman scattering, namely Stokes scattering (lower energy, longer wavelength), anti-Stokes scattering (higher energy, shorter wavelength), and Rayleigh scattering (elastic, same wavelength). [123]

2.6.5 Ellipsometry

Ellipsometry is a powerful and non-destructive optical technique used primarily to determine the thickness and optical properties of thin films. Ellipsometry works by analyzing the change in the polarization state of light as it reflects off a sample's surface [124]. The process begins with a known, polarized light source, labeled as the input light, $E_{in}(t)$ in Figure 14. This incident light beam is typically linearly polarized and strikes the sample at an angle away from the normal. Upon reflection, the light's polarization state is altered to become elliptically polarized, resulting in the output light, $E_{out}(t)$ (Figure 14). This change occurs because the electrical field components of the light parallel (p) and perpendicular (s) to the plane of incidence interact differently with the thin film structure; the p-component (E_1p) and s-component (E_1s) experience different amounts of attenuation and phase shift. [125]

The fundamental measurements of ellipsometry are the angles Psi (Ψ) and Delta (Δ), which are defined by the ratio of the reflection coefficients for the p- and s-polarizations (r_p and r_s). This relationship is given by the equation [124]:

$$\rho = \frac{r_p}{r_s} = tan(\psi)e^{i}\Delta \tag{8}$$

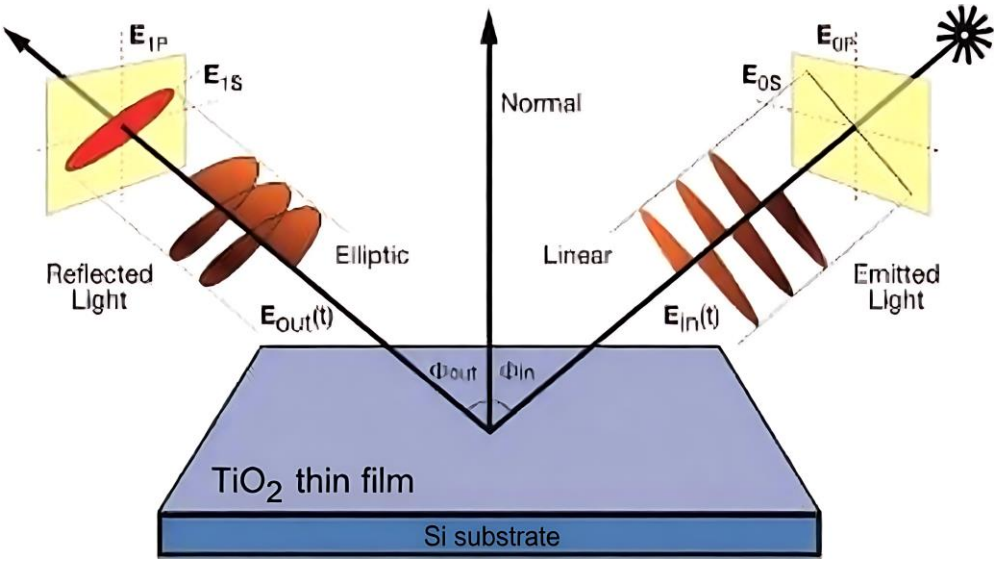

Figure 14. Ellipsometry principle and measurement. [125]

Here, tan(Ψ) represents the amplitude ratio, describing how the attenuation of the p- and s-components differ, and Δ represents the phase shift difference between the two components. The ellipsometer measures these Ψ and Δ values. To determine the thickness of the TiO_2 film, these measured values are then fitted to a theoretical optical model. This model describes the sample structure using parameters like the film thickness and its refractive index. A regression analysis is performed where the model's parameters are varied until the calculated Ψ and Δ values from the model match the experimentally measured ones. The thickness corresponding to this best fit is then reported as the measured thickness of the TiO_2 thin film. Therefore, ellipsometry is an indirect but highly sensitive technique that uses the perturbation of light's polarization by a thin film to extract precise information about its thickness and optical properties.[125]

2.6.6 XRD

X-ray diffraction (XRD) is a non-destructive analytical technique that characterizes crystalline materials by measuring how X-rays scatter at specific angles when interacting with ordered atomic planes [126]. The resulting diffractogram displays diffraction intensity versus the scattering angle (2θ), where each peak represents constructive interference from a set of crystal planes satisfying Bragg's law ($n\lambda = 2d\sin\theta$) [127]. To interpret the pattern, the position of peaks (2θ values) reveals the interplanar spacing (d) and crystal structure. The intensity indicates the relative abundance of each phase; and the peak width is inversely related to crystallite size. Narrower peaks suggest larger crystals, while broadening can signify nanoscale crystallites or structural defects [128]. Phase identification is achieved by comparing the experimental pattern against reference databases or literature standards, matching both peak positions and relative intensities [128].

3. LITERATURE REVIEW

Building upon the theoretical foundation established earlier, this chapter presents a literature review to develop the rationale for using an ALD TiO_2–AC composite in supercapacitors. It narrows the focus to the materials selected for this work, followed by a detailed description of the ALD process.

3.1 Carbon materials for supercapacitor electrodes

Carbon materials are the common choice for supercapacitor electrodes, primarily due to their high specific surface area for efficient charge accumulation, excellent electrical conductivity for rapid charge-discharge cycles, and remarkable chemical stability for long-term performance. While a high surface area is crucial for capacitance, it is not the sole determinant; the pore size distribution, pore shape, and overall conductivity are equally critical in maximizing specific capacitance. Furthermore, the versatility of carbon, from ACs to graphene and CNTs, allows for property tailoring, where porous structures enhance charge storage and nanostructures facilitate electron transport. Their abundance, affordability, and tunable surface chemistry make them exceptionally attractive for scalable, commercial energy storage devices. [129]

OLCs are spherical nanoparticles (4–25 nm) with concentric sp^2 carbon shells, providing high electrical conductivity for use as conductive agents and microelectrodes. In supercapacitors, OLCs enhance specific capacitance by 28.4% compared to Super-P carbon black by improving charge transfer and energy storage [130] [131]. Their exohedral, nonporous structure offers easy electrolyte access to the surface [132], and in situ studies show ions accumulate at the OLC surface without altering bulk concentration, enabling high-rate performance even in ionic liquids or at low temperatures [133] [134].

A primary limitation is their moderate specific surface area (~500 m^2/g), which restricts energy density to <10 Wh/kg. KOH activation can increase capacitance fivefold [135], but this method suffers from significant mass loss and low yield. Due to their high conductivity and spherical structure, OLCs are promising as composite components with metal oxides or conductive polymers. Additionally, their use as anodes paired with metal oxide cathodes in asymmetric configurations effectively balances energy and power density [136].

CNTs possess exceptional properties, including a thermal conductivity over five times that of copper and a tensile strength exceeding 100 GPa [137]. Their high surface area,

low resistance, low density, and chemical stability make them valuable for energy and electronics applications. They are commonly synthesized via CVD, which offers controllable conditions and high yield but often produces CNTs with low crystallinity.

For supercapacitors, the positive curvature of CNTs supports superior high-power performance. Reducing CNT diameter can increase capacitance [138], while elevated temperature and pressure enhance ion access at the cost of reduced cycle life [139] [140]. Aligned CNT structures benefit from high packing density, yielding lower ESR and improved power performance [141] [142] [143].

A key limitation of CNTs is their reliance on physical ion adsorption, which restricts capacitance compared to faradaic materials. To overcome this, composites with metal oxides combine the conductivity and structure of CNTs with the high pseudocapacitance of oxides for enhanced electrochemical performance. [144] [145]

Graphene is an ideal supercapacitor electrode due to its ultra-high theoretical specific surface area of 2675 m^2/g and exceptional electrical conductivity, which could enable a theoretical electric double-layer capacitance of 550 F/g [146]. Its flexibility supports use in wearable electronics, such as graphene paper for all-solid-state supercapacitors [147], and graphene fibers for linear supercapacitors [148] [149]. Its optical transparency also enables transparent conductive films [150].

However, a major challenge is the restacking of graphene sheets during the reduction of GO, caused by strong π–π interactions. This agglomeration significantly reduces achievable capacitance below the theoretical value. A key mitigation strategy is forming graphene-metal oxide composites, where the TMO prevents graphene aggregation while graphene enhances the oxide's poor conductivity and surface area. [151] [152] [153]

AC is the most commonly used electrode material for EDLCs, favored for its outstanding physico-chemical properties including high electrical conductivity, chemical inertness, and a tunable, high surface area [154]. Its structural characteristics underpin its electrochemical performance. AC possesses an exceptionally high specific surface area, typically ranging from 500 to 3000 $m^2\ g^{-1}$ [155], which provides an extensive interface for electrostatic charge storage, directly enhancing capacitance Secondly, its well-developed and adjustable pore structure facilitates rapid ion diffusion, enabling the high power density and swift charge/discharge rates essential for applications demanding rapid energy bursts. These attributes yield high gravimetric capacitances of 200–550 $F\ g^{-1}$ in aqueous electrolytes and 130–230 $F\ g^{-1}$ in non-aqueous systems, allowing supercapacitors to complement or compete with batteries in specific roles. [156]

The material is also produced cost-effectively at scale through the high-temperature carbonization of precursors under inert conditions. Sources range from synthetic polymers and natural materials (e.g., coconut shells) to abundant waste biomass and fruit residues, with activation processes further refining the porous structure [157] [158].

A comparison of commercially available ACs is given below in Table 2.

Table 2. Electrochemical performances of various commercial activated carbons.

Commercial Carbon	**BET Surface Area (m^2/g**	**Specific Capacitance (F/g)**	**Voltage window**	**Electrolyte**	**Cycling Stability (%)**	**Ref.**
Kuraray YP-80F	2220	118	0--1.0V	1:5 wt ratio H_2O:NaCl	-	[159]
Kuraray YP-50F	2079	77	0--1.5V	0.5 M CH_3CO-ONa	99	[160]
Kansai MSP20X	2266	122	0--0.7V (vs. Ag/AgCl)	1 M $CaCl_2$	-	[161]
CEP21	2305	120	0--0.7V (vs. Ag/AgCl)	1 M $CaCl_2$	-	[161]
Kuraray P60	1765	74	0--0.7V (vs. Ag/AgCl)	1 M $CaCl_2$	-	[161]
Norit SX Plus	1096	63	0--0.7V (vs. Ag/AgCl)	1 M $CaCl_2$	-	[161]
Norit S51HF	660	44	0--0.7V (vs. Ag/AgCl)	1 M $CaCl_2$	-	[161]

SEM micrographs of some commercially available activated carbons are also given in Figure 15.

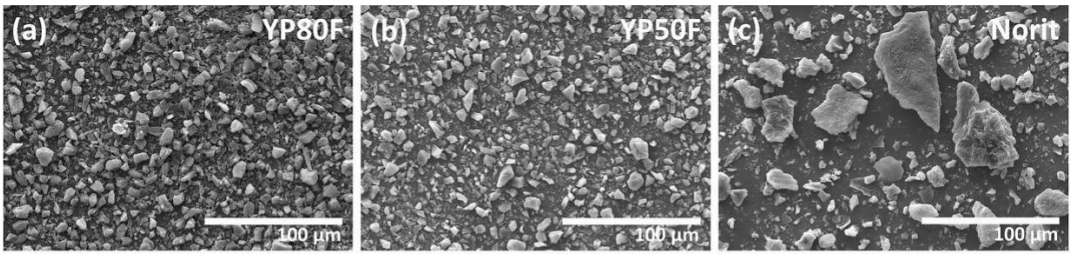

Figure 15. SEM micrographs at 500× magnification of (a) YP80F, (b) YP50F and (c) Norit. [162]

3.2 TMO-Carbon composites for supercapacitors

While the specific capacitance of carbon materials can be enhanced by increasing surface area, optimizing pore structure, and improving electrolyte wettability, these improvements are inherently limited. To achieve a substantial increase in capacitance, carbon materials must be combined with pseudocapacitive materials. Preparing TMO-carbon composites is a highly effective strategy for this purpose. In these composites, the carbon component provides efficient charge transfer channels and enhances rate capability due to its high specific surface area and electrical conductivity. [163]

TMOs like ruthenium oxide, nickel oxide, cobalt oxide, and vanadium oxide involve a combination of EDLC and dominant pseudocapacitance. This grants TMOs a higher theoretical capacitance and energy density than carbon-based materials or conducting polymers. Their overall performance, including power density, cycle life, and rate capability, is further determined by their structure, surface area, and metal oxidation states. Characterized by exceptional pseudocapacitive behavior, high ionic conductivity, and large charge storage capacity, TMOs are thus appealing candidates for high-performance supercapacitors. [164]

The incorporation of carbon nanotubes (CNTs) into NiO was shown to significantly enhance its supercapacitive performance. Compared to bare NiO, the NiO/CNTs nanocomposite exhibited a more ideal, rectangular-shaped cyclic voltammetry (CV) curve and reduced IR loss (voltage drop). These improvements are attributed to the CNT network, which boosts electrical conductivity and increases the specific surface area to provide more active sites for redox reactions. Consequently, the specific capacitance increased from 122 F g^{-1} to 160 F g^{-1} at a scan rate of 2 mV s^{-1} with a 10% CNT addition. [165]

Veeresh et al. [166] synthesized a GO/Co_3O_4 nanocomposite via a hydrothermal method. Using a PVA/KOH gel electrolyte, the electrode exhibited a high specific surface area and uniform morphology, achieving a specific capacitance of 1012 F g^{-1} at 2 A g^{-1}. The device demonstrated an energy density of 18.9 Wh kg^{-1}, a power density of 1364.8

W kg^{-1}, 96.9% coulombic efficiency, and retained 70.3% capacitance after 4000 cycles. Separately, Dong et al. [167] developed Co_3O_4 nanowires on reduced graphene oxide (rGO), which showed enhanced morphology and a capacitance of 1100 F g^{-1} at 10 A g^{-1}. The use of a 3D porous graphene foam mitigated issues like aggregation and inter-layer resistance. Micrometers-long Co_3O_4 nanowires (200–300 nm thick) were uniformly deposited on the graphene scaffold.

Numerous studies have demonstrated the enhanced electrochemical performance of supercapacitor electrodes based on composites of transition metal oxides (TMOs) and activated carbon (AC). Huang et al. [168] fabricated a bamboo-derived AC-MnO_2 nanocomposite, where MnO_2 nanoparticles were deposited onto the carbon core via a redox reaction. This composite achieved a high specific capacitance of 221.45 F g^{-1} at 1 A g^{-1} and maintained 89.29% capacitance after 1,000 cycles. Similarly, a composite of copper oxide and bamboo leaf-derived AC exhibited a specific capacitance of 147 F g^{-1} with exceptional cycling stability, retaining 93% of its capacity after 10,000 cycles [169].

Jiang et al. [170] synthesized a hybrid of Fe_2O_3 and hemp straw-based AC (HAC). The AC component effectively minimized ion diffusion distances and prevented particle agglomeration, leading to improved electrochemical activity. The Fe_2O_3/HAC composite delivered a specific capacitance of 256 F g^{-1} at 1 A g^{-1}, outperforming its individual components and exhibiting good cyclability.

3.3 Titanium Dioxide

TiO_2 is a prominent electrode material for supercapacitors, valued for its low cost, natural abundance, non-toxicity, high photochemical stability, and pseudocapacitive behavior [171]. It exists in three primary polymorphs, brookite, anatase, and rutile, each having its own distinct crystal structure (Figure 16).

- Brookite has an orthorhombic structure with lattice parameters a = 9.174 Å, b = 5.439 Å, c = 5.163 Å.
- Anatase is tetragonal with lattice parameters a = b = 3.784 Å, c = 9.515 Å.
- Rutile is also tetragonal with lattice parameters a = b = 4.593 Å, c = 2.958 Å.

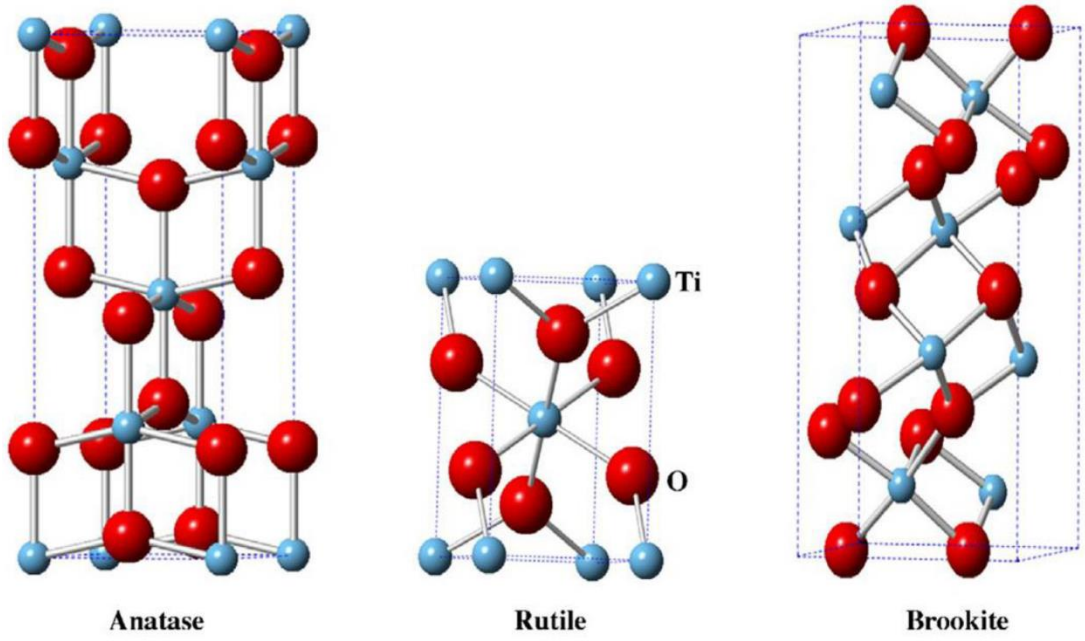

Figure 16. Crystal structures of different TiO_2 polymorph phases. [172]

All three phases consist of TiO_6 octahedra, but their connectivity differs: in rutile, octahedra form linear chains by sharing two opposite edges, which are then connected at corners. Anatase features no corner-sharing but has four shared edges per octahedron. Brookite displays a combination of corner-sharing and edge-sharing, with chains aligned parallel to the c-axis. [172]

The suitability of TiO_2 for supercapacitor electrodes is further enhanced by the ease of fabricating diverse nanostructures, such as 3D nanocomposites, 2D nanosheets, 1D nanotubes/nanorods, and 0D nanoparticles. Its pseudocapacitive charge storage mechanism involves reversible electron transfer via the Ti^{4+}/Ti^{3+} redox couple. [173] [174]

A highly promising strategy to improve performance is the hybridization of TiO_2 with porous carbon materials (e.g., activated carbon, graphene, carbon nanotubes). This composite approach synergistically combines the pseudocapacitive contribution of TiO_2 with the high surface area and excellent electrical conductivity of carbon-based Electric Double-Layer Capacitor (EDLC) materials, leading to enhanced specific capacity and electron transfer for advanced energy storage devices. [172]

Saliu et al. [175] demonstrated that a starch template dramatically enhances TiO_2 performance, with an A-TiO_2 composite (72% anatase, 28% rutile) achieving 388 F/g, 194 Wh/kg, and 4473 W/kg while maintaining 99% capacitance retention after 20,000 cycles, far outperforming unactivated U-TiO_2 (83 F/g) and template-free TiO_2 (74 F/g). Kumar et al. [176] reported that an anatase TiO_2/sucrose-derived carbon composite (ICS-TiO_2) reached 227 F/g in a symmetric cell (max 277.72 F/g) with 9.64 Wh/kg and 867.90 W/kg,

retaining 6.91 Wh/kg even at 200 mV/s despite higher series resistance (11.3 Ω vs. 7.5 Ω for bare TiO_2). Bortamuly et al. [177] reported a TiO_2/bio-activated carbon nanocomposite with 214 F/g and 92% retention after 5000 cycles, though the dominant charge storage mechanism remained unresolved.

3.4 Atomic Layer Deposition

Atomic Layer Deposition (ALD) is a vapor-phase technique for depositing high-quality, uniform, and highly conformal thin films, distinguished from CVD by its sequential, alternate introduction of gaseous precursors [179]. Developed in the mid-1970s by Suntola et al. as "atomic layer epitaxy" for depositing ZnS on flat-panel displays [178], ALD has evolved into a mature technique for scientific and industrial applications [28].

ALD growth is governed by surface-limited chemisorption, enabling atomic-level precision that overcomes conventional deposition challenges: CVD's high processing temperatures (>300 °C) create internal stresses from thermal expansion mismatch, while PVD's line-of-sight limitation yields inadequate step coverage for complex nanostructures. This multi-step method has demonstrated significant potential across numerous fields including microelectronics, photovoltaics, optoelectronics, fuel cells, nanogenerators, photoelectrochemical solar cells, lithium-ion batteries, and supercapacitors. [28]

A comparison of ALD with CVD and PVD is given in Table 3.

Table 3. Comparison of ALD with conventional deposition techniques, namely CVD and PVD. [196]

Film Deposition Techniques	**Deposition Principle**	**Deposition Pattern**	**Uniformity**	**Conformality**	**Expansibility**	**Degree of Vaccum**	**Film Thickenss**
PVD	Physical vapour deposition	Nucleation growth	High number of pinholes and particles exist	Low and only for flat substrate	Medium	High requirement	Nanometer level
CVD	Gas-phase chemical reaction	Nucleation growth	Low number of pinholes and particles exist	Medium	Low	Medium	Nanometer level
ALD	Surface saturated reaction	Layer-by-layer growth	Low number of pinholes and no particles	High	High	Low	Ångström level

3.4.1 Mechanism

Self-Limiting Reactions

Atomic Layer Deposition (ALD) is fundamentally based on sequential, self-terminating gas-solid reactions, which distinguish it from other deposition techniques. The process employs two gaseous precursors, labeled A and B in Figure 17, which are introduced into the reactor in a strictly separated, alternating sequence (ABAB...). Each precursor pulse constitutes a "half-reaction" where the molecules chemisorb onto the active sites of the substrate surface. A key feature of this mechanism is its self-terminating nature; the reaction will naturally cease once all available reactive surface sites have been occupied, preventing the deposition of more than a monolayer (or a fraction of one) per

pulse. This self-limitation occurs irrespective of the amount of excess precursor supplied or the duration of the pulse beyond what is required for surface saturation. Between each precursor pulse, the reactor is purged with an inert gas to thoroughly remove any unreacted precursor and reaction by-products, which is critical to prevent gas-phase reactions and maintain the self-limiting characteristic. [179]

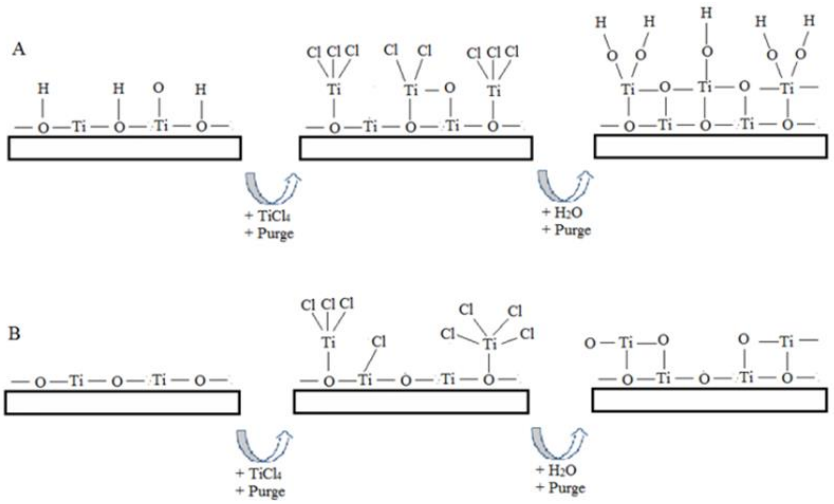

Figure 17. TiO_2 ALD process sequence showing (A) $TiCl_4$ precursor pulse, which chemisorbs onto surface hydroxyl groups, and (B) H_2O co-reactant pulse, which hydrolyzes Ti-Cl bonds to form Ti-O bridges while regenerating hydroxyl sites for subsequent cycles. [179]

Saturation

Saturation is the practical manifestation and essential outcome of a successful self-limiting reaction. It describes the state where the substrate surface has absorbed the maximum possible amount of precursor molecules during a single pulse. When saturation is achieved, the Growth Per Cycle (GPC), i.e. the amount of material deposited in one complete AB cycle, becomes constant. This constant GPC is the hallmark of a well-behaved ALD process, enabling precise and predictable thickness control simply by counting the number of cycles. Saturation is primarily caused by two factors. The first is steric hindrance, where the large ligands of the already-chemisorbed precursor molecules physically shield adjacent reactive sites, acting like umbrellas that block further adsorption. The second factor is the finite number of reactive surface sites, such as hydroxyl (-OH) groups; once all these specific sites have reacted, the process has no choice but to stop, thereby ensuring a self-limited and saturated layer. [179]

For example, Vitto et al. [33] tested different pulse times for both the precursors of TiO_2 deposition. $TiCl_4$ and H_2O pulse times were varied (Figure 18), and the optimum pulse time for both precursors was 450 ms the time where no further GPC increase (or decrease) was observed. However, it is important to note that this self-limiting region was estimated using a separate, flat silicon wafer. It does not guarantee identical saturation

behavior within the confined nanopores of a carbon substrate, where transport limitations and distinct surface chemistry can alter the deposition process.

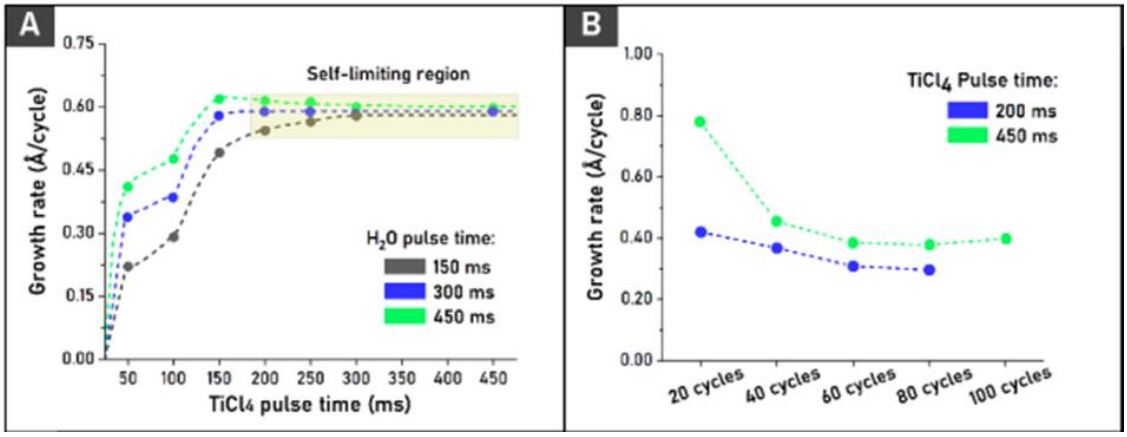

Figure 18. GPC in terms of (a) TiCL4 pulse time and (b) number of ALD cycles. The plateau region confirms that precursor exposure beyond the saturation does not increase growth, indicating the self-limiting region. [33]

Temperature Window

The ALD temperature window defines the specific range of deposition temperatures within which the self-limiting reactions and saturation operate optimally, leading to a constant GPC. Operating within this window is critical for achieving high-quality, conformal films. If the temperature is too low, below the window (L1 and L2 in Figure 19), the process is hampered by precursor condensation or physisorption on the surface, and the thermal energy may be insufficient for the precursors to overcome the activation energy required for complete chemisorption. Both low-temperature issues can lead to non-ideal growth and a deviation from the ALD mode to a parasitic CVD mode. Conversely, if the temperature is too high above the window (H1 and H2 in Figure 19), the thermal stability of the precursors is compromised, leading to precursor decomposition or desorption, which destroys the self-limiting mechanism. Therefore, the ideal ALD window is a temperature range where precursors are sufficiently volatile and reactive to achieve full surface saturation without condensing, yet thermally stable enough to avoid decomposition or desorption. [33] [179]

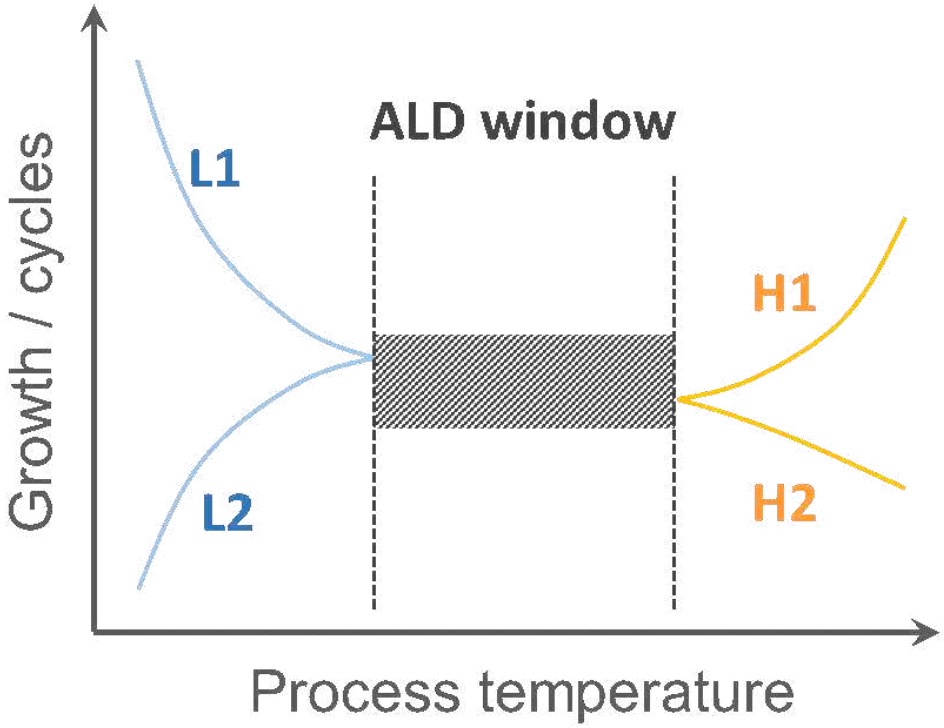

Figure 19. TiO_2 ALD temperature window showing stable GPC plateau between L1–H1. Below L1, incomplete chemisorption occurs; above H2, precursor decomposition leads to uncontrolled growth, compromising self-limiting deposition. [180]

The surface reactions involved TiO2 ALD films are [33]:

1. TiOH (s) + $TiCl_4$ (g) → TiO—$TiCl_3$ (s) + HCl (g)
2. TiCl (s) + H_2O (g) → Ti—OH (s) + HCl (g)

The cycle begins on a hydroxyl (OH)-terminated surface, where $TiCl_4$ reacts to form a titanium chloride intermediate, releasing HCl gas (Reaction 1). This is followed by a water pulse, which hydrolyzes this intermediate to regenerate the hydroxyl-terminated surface, again releasing HCl (Reaction 2).

A single TiO_2 ALD cycle consists of four distinct stages as shown in Figure 20:

i. Exposure of the surface to the $TiCl_4$ precursor.
ii. An inert nitrogen purge to remove any unreacted $TiCl_4$ and the HCl by-product.
iii. Exposure of the surface to the H_2O precursor.
iv. A second nitrogen purge to remove excess H_2O and HCl.

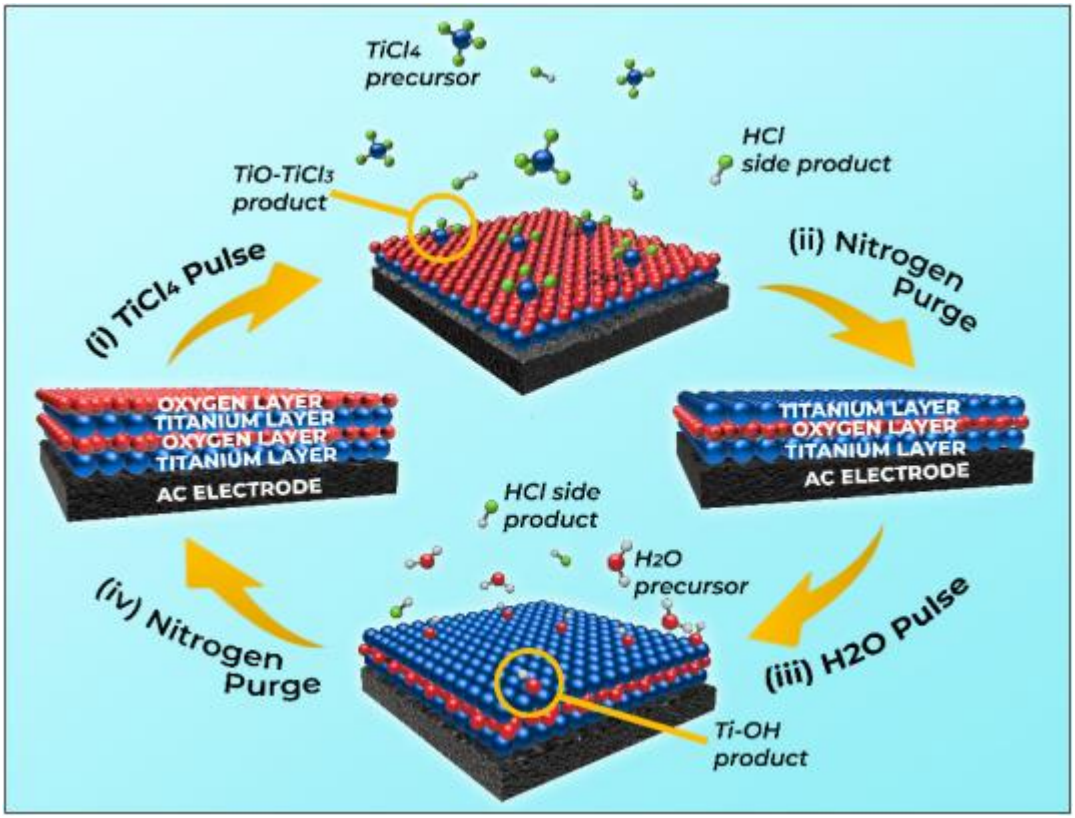

Figure 20. Schematic illustration of one complete ALD cycle of TiO_2. This cycle is repeated to achieve the required film thickness. [33]

3.4.2 ALD on ACs for supercapacitors

In a study [181], Al_2O_3 was deposited on YP-50F activated carbon using atomic layer deposition (ALD) at 150 °C with trimethylaluminum and water. Coatings were applied for 2, 5, 10, 20, 50 and 100 ALD cycles. While the Al_2O_3 layer was barely detectable after 2 cycles, transmission electron microscopy revealed a visible thin film after 20 cycles, growing at a rate of approximately 1 Å per cycle, though the coating was noted to be inhomogeneous. The electrochemical performance was significantly enhanced by a 20-cycle ALD coating. The electrolyte used for testing was 1 M TEABF4/acetonitrile organic electrolyte. The coated electrode retained 84% of its capacitance after 1000 cycles at 4 V, a substantial improvement over the 48% retention of uncoated carbon. The ALD coating enabled stable operation at 4 V. It is mentioned that activated carbon electrodes typically operate below 3 V, so roughly a 1 V higher operating window was achieved. Furthermore, charge retention after 12 hours more than doubled, from less than 25% for bare cells to 53% for the coated ones. Analysis linked this improved charge-retention to a slower self-discharge dominated by ion diffusion mechanism. These improvements were attributed to the ALD coating's dual role. The Al_2O_3 layer not only improved performance at a high voltage of 4 V by acting as a thickened Stern layer but also suppressed

the surface oxygen functional groups of the activated carbon, improving the cyclic retention. However, an overly thick coating was found to block the AC nanopores and consequently degrade the cycling performance. Pore blocking became significant at a coating thickness of 10 nm (100 ALD cycles), where micropore volume decreased noticeably and capacitance dropped, though cycling retention remained stable.

Before this, Hong et al. [182] deposited a 2nm Al_2O_3 coating on activated carbon at 180°C. 1.0 M tetraethylammonium tetrafluoroborate (Et_4NBF_4)/acetonitrile organic electrolyte was used. XPS and Boehm titration confirmed the coating substituted more than half of the oxygen functional groups that cause faradaic degradation, while BET, BJH, and HK analyses revealed this ultrathin layer did not block mesopores or micropores. The coating delivers measurable improvements, extending stable operation to 3V (a 39% energy density boost over typical 2.5–2.7V) and achieving 74% voltage retention after 50h versus 56% for bare AC. After 5,000 cycles, capacitance retention is superior (88% vs 75%), and resistance remains stable (1.05 vs 1.84 Ω cm²), but specific capacitance is slightly reduced (37 vs 38 F/g) and initial resistance is higher (0.92 vs 0.53 Ω cm²). While 3V is high, it falls short of the 3.5–4.4V achieved in other studies cited by the authors themselves. The coating's key advantage is suppressing swelling phenomenally (4% vs 644%) and stabilizing long-term performance by replacing oxygen functional groups, but this comes at the cost of modest initial performance penalties and a voltage ceiling that, while improved, does not push absolute limits.

Daubert et al. [183] investigated using ALD of vanadium oxide (V_2O_5), to enhance the performance of supercapacitors made from two types of activated carbon: mesoporous Darco G60 and highly microporous DLC Supra 50. The V_2O_5 ALD process was optimized at 150°C to add pseudocapacitive charge storage to the carbon electrodes. The mesoporous G60 carbon showed significant improvement, with a 46% increase in specific capacitance after 75 ALD cycles while maintaining excellent long-term stability (89% capacitance retention over 10,000 cycles). In contrast, the microporous Supra carbon showed only minimal capacitance gains from the ALD coating. This difference in performance is attributed to how the ALD process interacts with different pore sizes. The precursors readily coated the larger mesopores of G60, adding pseudocapacitance without sacrificing the carbon's double-layer capacitance. However, the tiny micropores of the Supra carbon (mean micropore size is ~11 Å) physically restricted precursor entry (longest dimension VTIP molecule is 9.6 Å,). Instead of coating the interior, the V_2O_5 primarily deposited at the pore openings, blocking them and reducing the accessible surface area, which negated the benefits of added pseudocapacitance. It was therefore demonstrated

that activated carbon's pore structure is critical if one wants to achieve the desired capacitive performance via ALD.

Wu et al. [184] examined the effect of precursor pulse times of ALD deposition of crystalline zinc oxide (ZnO) on YP-50F AC between 70–150 °C. While a 100 ms pulse failed to produce crystalline structure, a 400 ms pulse readily formed a distinct crystalline ZnO phase even at 70°C. Also, material characterization confirmed that >20 cycles coatings preserved the AC's microporous structure and high surface area. Electrochemical analysis revealed that a 6-cycle ZnO coating delivered the best performance, showing the largest CV loop area, ideal charge-discharge characteristics, superior charge retention maintaining 2 V after 10,000 seconds, and lower impedance (3-10 Ω) compared to pristine AC (9.1 Ω). Although a 20-cycle coating showed longer GCD times at 3.2 V, its was less favourable in terms of CV loop area. Coatings applied at 150°C yielded higher capacitance due to more optimal crystalline formation enhancing ion migration. Thus, it was concluded that ZnO-coated AC electrodes enabled improved cyclic capacitance retention (50%) at extended operating voltage.

Vitto et al. [33] explored the effect of ALD-deposited TiO_2 on YP-80F porous activated carbon supercapacitors. The specific capacitance increased from 113 F/g of bare AC to 182 F/g and 187 F/g for 60 and 80 TiO_2 ALD cycles, respectively. This shows that beyond 60-cycles deposited AC, there was not much improvement in specific capacitance. However, it was also observed that the contribution to specific capacitance by TiO_2 conformal layer increased as the upper limit potential increased from 1.2V to 1.4 V. An increase in ESR was observed with greater TiO_2 thickness (80-100 ALD cycles). It was deduced that the ALD process increased the number of oxygen-containing functional groups. These functional groups facilitated electrolyte decomposition and undesirable parasitic faradaic side-reactions, which was identified as a cause for the elevated ESR. These functional groups also decreased the conductivity of electrodes. BET analysis showed a decrease in surface area and pore volume of 100-cycles deposited TiO_2, due to pore blocking. CV analysis showed electrolyte degradation and parasitic faradaic reactions when upper limit potential was increased. This could also be attributed to small working potential of NaCl electrolyte.

In light of the existing literature, Table 4 compiles the optimal ALD coating thicknesses reported across different studies for various metal oxides on activated carbon.

Table 4. Literature-reported optimal ALD coating thicknesses for metal oxides on activated carbon. Values represent the thickness (in nm) that yielded the best electrochemical performance in each study.

Metal Oxide	Deposited thickness (nm)	Reference
Al_2O_3	2	[181] [14] [182]
V2O5	0.5-0.75 1.5-2.25	[183]
ZnO	1-3	[184]
TiO_2	≈2.3	[33]
Al_2O_3, ZnO-Al_2O_3, TiO_2	1-3	[185]

4. EXPERIMENTAL AND METHODS

This chapter outlines the experimental procedures employed in this study, beginning with electrode fabrication methods. It subsequently details the specific conditions and parameters for electrochemical and materials characterization techniques. Figure 21 presents a flow chart of our experimental plan to facilitate reader understanding.

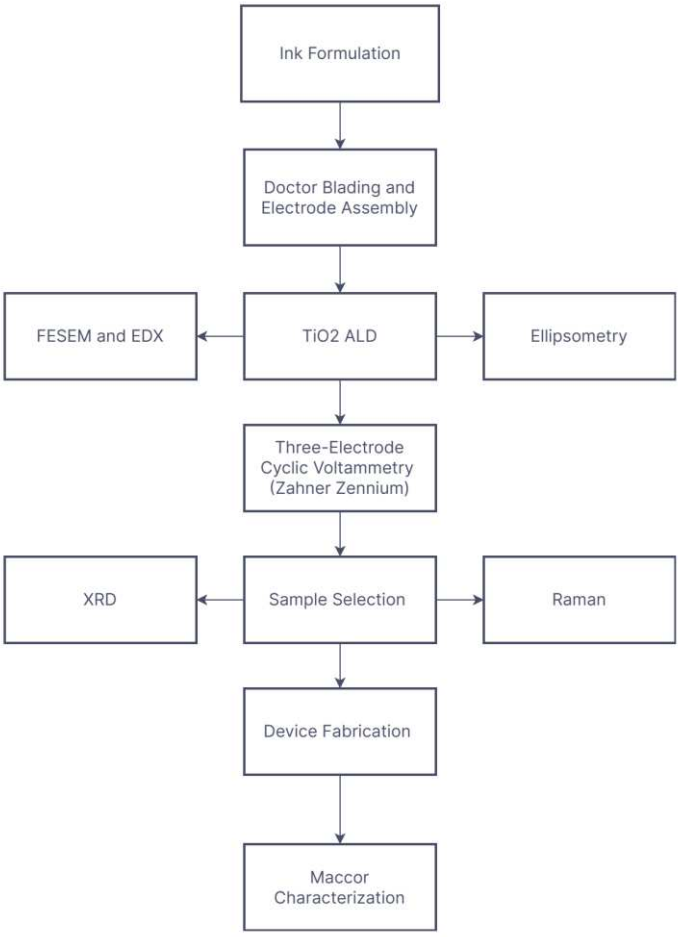

Figure 21. Sequential workflow diagram of the research methodology for the fabrication and characterization of supercapacitor devices.

4.1 Ink formulation and electrode assembly

The AC electrode ink was formulated using YP-80F as the primary active material, constituting 90% of the solid weight, with the remaining 10% consisting of a styrene-butadiene rubber and carboxymethyl cellulose (SBR/CMC) binder system.

The preparation began by creating a pre-diluted aqueous binder solution containing 2 wt% CMC and 40 wt% SBR. To synthesize the final ink, 28 grams of this CMC solution

and 0.12 grams of Triton X-100 surfactant were gradually incorporated into 14 grams of YP-80F powder. The mixture was then diluted with approximately 30 grams of deionized (DI) water and homogenized using an Ultra-Turrax T 10 basic homogenizer. Following this, 3.2 grams of the SBR solution was added while stirring continued. The ink's viscosity was carefully adjusted to the target value by the slow addition of further DI water. The finalized ink was stored in a syringe within a desiccator to await use.

The fabrication process of a single electrode, shown schematically in Figure 22, began with the creation of a 50 µm thick Kapton stencil, into which the electrode patterns were precision-cut using a Silhouette Cameo 3 machine. This stencil was then aligned over the clean Polyethylene terephthalate (PET) film substrate (125 µm thick, Melinex ST506, DuPont Teijin Films). Graphite paste (LOCTITE EDAG PF 407C) was applied generously over the stencil, and a 220 mm doctor blade was used to force the ink through the cutouts in the Kapton stencil to print the current collector patterns. These printed collectors were subsequently cured in an oven at 95°C for one hour. Following this, the prepared YP-80F activated carbon-based ink was printed directly onto the dried graphite current collector layer. This printed electrode layer was then left to dry overnight at ambient temperature. [33]

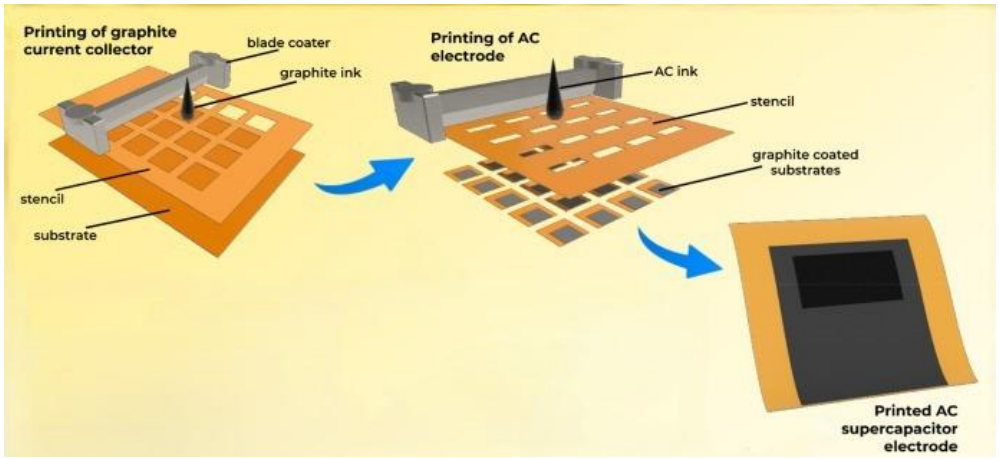

Figure 22. Schematic illustration of a single electrode fabrication [33]

4.2 TiO_2 ALD process

A Beneq TFS 200 ALD system was used to deposit TiO_2 nanofilms. The deposition was performed directly onto the prefabricated supercapacitor electrodes. For the purpose of monitoring film thickness using ellipsometry, 50 mm silicon wafers were coated simultaneously as reference samples. The process utilized $TiCl_4$ and DI water as the precursors in a sequential, self-limiting reaction cycle to achieve atomic-level control over the film

growth. Three different temperatures and nine different number of cycles for each temperature were used to deposit TiO_2 on prefabricated electrodes, with the mass of YP-80F remaining in 3.6 ± 0.3 mg range for each electrode. The masses of each electrode are also given below in Table 5.

Table 5. Mass of each prefabricated electrode used for ALD in milligrams (mg)

Temperature (°C)	**Number of Cycles**								
	5	**10**	**15**	**20**	**40**	**60**	**80**	**100**	**120**
100	3.6	3.7	3.5	3.5	3.6	3.7	3.6	3.6	3.4
120	3.7	3.3	3.7	3.5	3.6	3.6	3.6	3.5	3.8
140	3.5	3.6	3.6	3.5	3.6	3.5	3.5	3.5	3.6

4.3 Three-electrode CV

The first electrochemical test was CV, carried out in a three-electrode configuration, using a Zahner Zennium electrochemical workstation. The setup consisted of a silver/silver-chloride (Ag/AgCl, Redoxme AB) reference electrode and a platinum coil (Redoxme AB) counter electrode. 1 M Na_2SO_4 aqueous solution served as the electrolyte. The measurements were conducted within a potential window of -1.0 V to 0.0 V (vs. Ag/AgCl) to characterize the samples as negative electrode materials, using a scan rate of 10 mV/s.

The two electrodes which showed the highest specific capacitance from each temperature class, were then chosen for device fabrication and characterization, and materials characterization like XRD and Raman. However, to broaden the structural and morphological analysis, a refinement criterion was applied. If the two highest-performing samples within a temperature class differed by ≤10 ALD cycles, the second-best performer was replaced with a moderately performing sample exhibiting a larger cycle-count difference (>10 cycles). Additionally, to enable meaningful cross-temperature comparisons, preference was given, where possible, to selecting at least one sample per temperature class with the same ALD cycle count. In this context, cyclic voltammetry served not only as a performance analysis but also as a crucial step guiding sample selection for further electrochemical and structural analysis.

4.4 Device fabrication

After the three electrode CV, the samples were selected according to the criterion mentioned in Section 4.2, and seven asymmetric device were fabricated. Each ALD-coated sample served as the negative electrode against a bare YP-80F positive electrode of similar mass. A symmetric device with two bare YP-80F electrodes was also fabricated as a control for performance comparison.

The method of device fabrication followed here is reported by H. Pourkheirollah et al. [159]. The device fabrication began with an aluminum/polyethylene terephthalate (Al/PET) flexible laminate substrate, featuring a 9 µm aluminum layer and a 50 µm PET layer (Fig. 23a). This substrate was first pre-heated at 95 °C for 15 minutes (Fig. 23b). A graphite ink current collector was then doctor-bladed onto the PET side, using the aluminum layer as a backing (Fig. 23c), and was dried at 95 °C for one hour to form a 25–35 µm thick layer (Fig. 23d).

Subsequently, an AC ink electrode layer was applied atop the current collector using the same blade-coating method (Fig. 23e) and was dried overnight at room temperature, resulting in a 30–40 µm thick film. A layer of adhesive was then applied over the PET and a portion of the current collector (Fig. 23f). Following this, an aqueous electrolyte was dispensed onto the electrode surface (Fig. 23g). A commercial cellulose separator (Dynacap GT 0.45/40, Glatfelter) was placed onto the electrolyte-soaked electrode, ensuring both components are fully impregnated (Fig. 23h).

The final assembly involved sealing two identical electrodes face-to-face with the adhesive, with one electrode pair including the separator between (Fig. 23i). The completed supercapacitor, including its packaging, had final dimensions of 50 mm in length, 50 mm in width, and a thickness ranging from 0.35 to 0.45 mm.

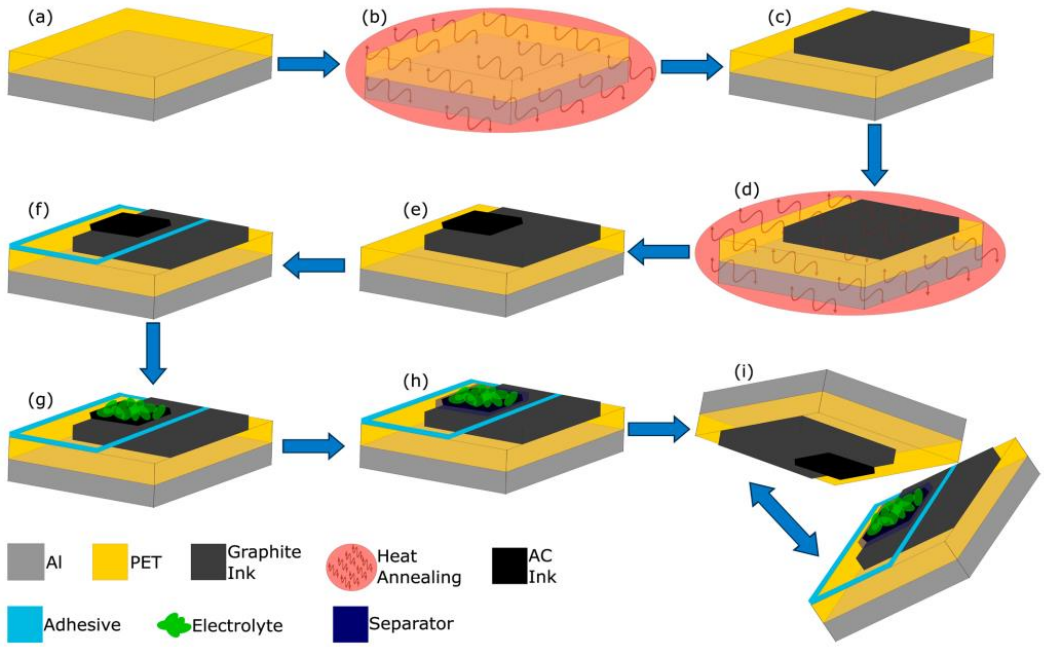

Figure 23. The supercapacitor fabrication process follows these sequential steps: (a) Starting with an Al/PET substrate; (b) Pre-heating the substrate; (c) Depositing a graphite ink current collector on the PET side; (d) Drying the graphite layer; (e) Depositing an AC ink to form the electrode layer; (f) Applying an adhesive; (g) Adding an aqueous electrolyte onto the electrode; (h) Placing a cellulose paper separator; and finally, (i) Assembling and sealing two electrodes face-to-face. [159]

The active mass of the fabricated devices is given below.

Table 6. Masses of fabricated two-electrode SC devices

Device	**Active mass (mg)**
Bare YP-80F	5.6
100°C – 10 Cycles	6.0
100°C – 40 Cycles	6.5
120°C – 15 Cycles	6.4
120°C – 40 Cycles	6.4
140°C – 40 Cycles	5.8
140°C – 60 Cycles	6.9

4.5 Device performance characterization

The electrochemical characterizations carried out are CV and GCD, the theories of whom were mentioned Chapter 2. The assembled supercapacitor devices were electrochemically characterized using a Maccor 4300 workstation (Maccor Inc., USA) in a two-electrode configuration according to IEC 62391-1 [186]. The measurement sequence comprised galvanostatic charge-discharge (GCD) cycles at 1, 3, and 10 mA within a voltage window of 0 to +1.2 V. At each current level, the fourth cycle included a 30-minute hold at the upper voltage limit (+1.2 V) prior to discharge. Specific capacitance was calculated from the 1 mA discharge curve between 80% and 40% of maximum voltage. ESR was determined from the initial IR drop measured at 10 mA after the voltage hold, as the standard recommends higher current for ESR measurement. Leakage current was recorded during the final one-hour hold period. Following the GCD protocol, cyclic voltammograms were acquired at scan rates of 100, 50, 10, and 5 mV/s (four cycles each). [33] [187]

To ensure fair comparison of intrinsic material properties and remove the effects of variation in active mass of the devices, a voltage-specific capacity graph derived from the discharge curve of absolute raw GCD of the devices was also given (Figure 28b) [188].

Cyclic stability was measured over 10,000 GCD cycles (capacitance measured every 100 cycles), with the plotted curve displaying every 500th cycle and adjacent averaging filter applied for noise reduction (Figure 29).

4.6 Materials characterization

Reinshaw inVia Qontor spectrometer (equipped with a 50x objective confocal microscope) was used for Raman Analysis. A green, 532 nm diode-pumped solid-state laser, operating at 1.429 mW, was used as excitation source. Spectra were collected from 100-3700 cm^{-1} (stitched from two grating positions) and a more focused range from 50-1853 cm^{-1} (without stitching).

XRD analysis was conducted using an X-Ray diffractometer MiniFlex 600 (RIGAKU) with parameters set to a step size of 0.020°, a scan speed of 3°/min, a current of 15 mA, a voltage of 40kV, and a 2θ range of 20°–65° (with a supplementary short scan from 20°–30° at a step size of 0.01° and a scan speed of 1°/min).

For FESEM and energy-dispersive X-ray spectroscopy (EDS), the samples were cut into ~7 × 7 mm pieces and mounted on aluminum stubs (Agar, AGG301F) using conductive carbon adhesive discs (Agar, AGG3347N). To ensure proper electrical grounding and reduce charging during imaging, conductive carbon glue (Agar, AG16050) was applied

between the sample edge and the stub. A thin carbon coating (~10 nm) was then deposited on the sample surface using a high-vacuum sputter coater (Leica EM ACE600) with carbon thread pulses. Surface morphology of both AC and TAC samples was imaged with a Zeiss Ultra Plus FESEM operated at 10 kV and a working distance of 8.3 mm. Elemental mapping was performed using the integrated Oxford Instruments X-MaxN EDS detector. The samples selected for FESEM were 100°C-20 cycles, 100°C-100 cycles, 140°C-20 cycles and 140°C-100 cycles, both before and after cyclic voltammetry, to observe any change in morphology caused by electrode-electrolyte interaction due to cycling. The samples chosen for EDX were 100°C-20 cycles, 100°C-80 cycles, 140°C-20 cycles and 140°C-80 cycles.

5. RESULTS AND DISCUSSION

The following chapter presents the results of various electrochemical and material characterization studies and provides a detailed discussion and interpretation of the findings.

5.1 CV

Figure 24 shows the voltammograms from three-electrode CV.

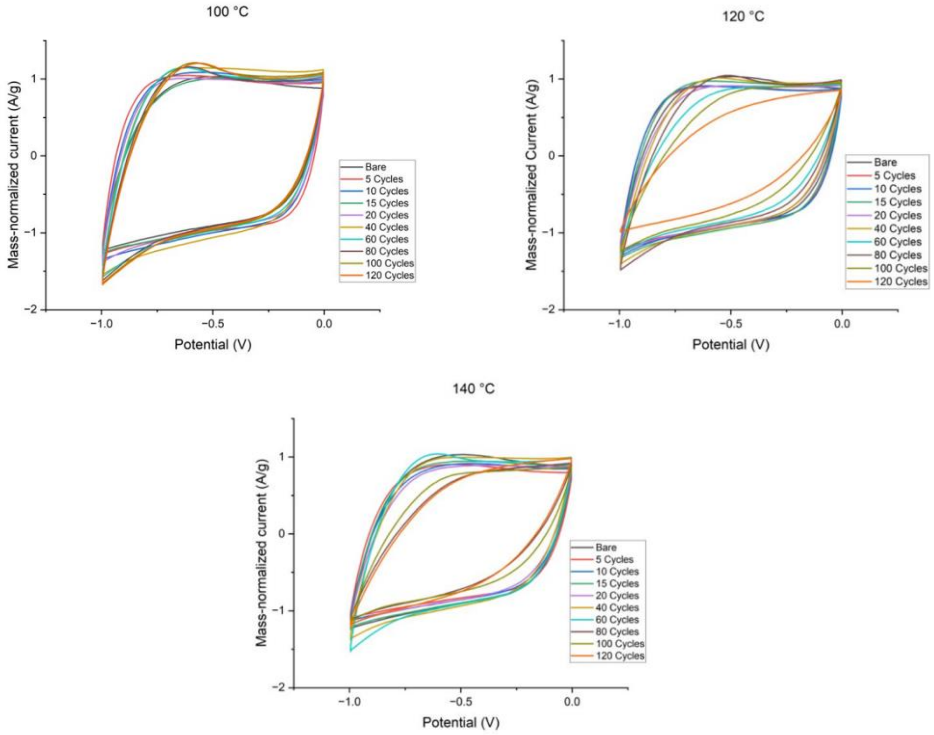

Figure 24. Voltammograms from three-electrode CV, grouped by ALD temperature.

All cyclic voltammetry curves exhibit a quasi-rectangular shape, confirming that the charge storage is dominated by EDLC from the carbonaceous substrates [189]. A key finding is that an optimal number of ALD cycles, which may vary with deposition temperature, enhances electrode performance. This is evidenced by a larger CV curve area, indicating a higher specific capacitance compared to the bare activated carbon. Crucially, this improvement occurs without the characteristic faradaic peaks of TiO_2 pseudocapacitance, indicating that the higher capacitance stems not from redox activity, but from the TiO_2 layer enhancing the electrochemical activity of the carbon surface. However, exceeding this optimal cycle count leads to a progressive decline in performance. The CV area shrinks, shown by a reduced current response, signaling a loss of specific capaci-

tance. Concurrently, the curves distort further from an ideal rectangular shape to an elliptical one, suggesting a rise in internal resistance as the thicker TiO_2 layer likely begins to clog the carbon's pore structure.

The specific capacitance for each sample was determined by integrating the area enclosed by CV curves and then applying the equation (5) from section 2.6.1. For a clearer comparative picture, the specific capacitance values for each sample are presented in Table 7 and graphically plotted against the number of ALD cycles in Figure 25.

Table 7. Specific capacitance values (F/g) from three-electrode CV

Number of Cycles	**Temperature (°C)**		
	100	**120**	**140**
0	76.0	76.0	76.0
5	86.2	75.8	70.4
10	86.7	76.4	69.8
15	76.8	78.6	73.9
20	82.3	71.5	67.7
40	89.9	74.1	75.3
60	84.5	62.2	76.6
80	80.1	70.1	49.3
100	82.4	54.2	54.4
120	81.0	41.6	50.0

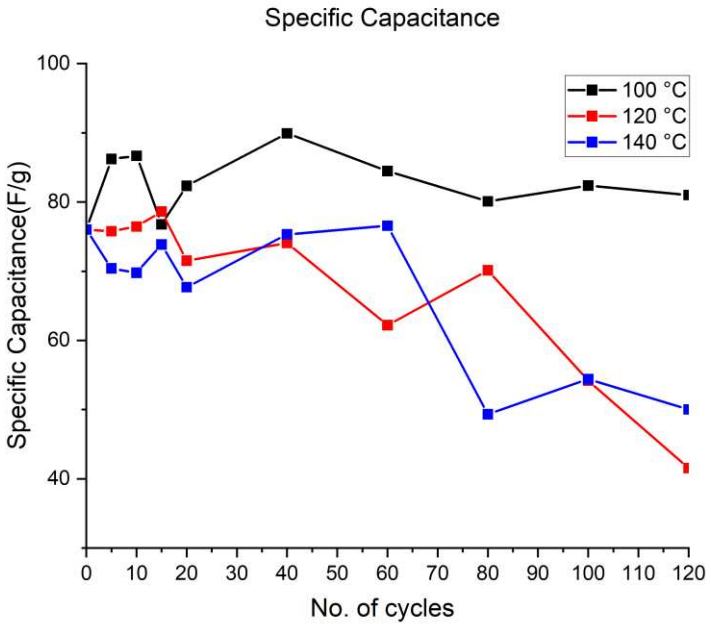

Figure 25. Graphical representation of specific capacitance versus ALD cycle number for electrodes processed at different ALD temperatures.

The specific capacitance exhibits a non-linear dependence on TiO_2 ALD cycles across all temperature regimes. The sample with 40 ALD cycles at 100°C demonstrates the most significant enhancement of around 18% increase over the bare electrode. In contrast, the sample with 40 cycles at 140°C shows only a minimal improvement of around 0.7%, while the 15-cycle sample at 120°C shows around 3.5% increase. No clear linear or proportional relationship exists between cycle number and capacitance, suggesting competing mechanisms (e.g. surface modification, pore clogging) that affect the CV curve area.

Based on the three electrode CV results, two samples from each temperature class were selected for further electrochemical and material characterizations. The selection criterion mentioned in Section 4.3 was followed. The final selection for further analyses includeed the 100 °C-10 cycles, 100 °C-40 cycles, 120 °C-15 cycles, 120 °C-40 cycles, 140 °C-40 cycles, and 140 °C-60 cycles samples.

Supercapacitor devices of six selected samples were made as mentioned in Section 4.4 and their electrochemical performance was evaluated as mentioned in 4.5.

The specific capacitance results from the procedure are shown below in Table 8.

Table 8. Specific Capacitances (F/g) of the fabricated SC devices.

SC Device	**Specific Capacitance**
100°C – 10 Cycles	24.2
100°C – 40 Cycles	26.7
120°C – 15 Cycles	18.6
120°C – 40 Cycles	24.3
140°C – 40 Cycles	27.9
140°C – 60 Cycles	27.6
Bare YP-80F	26.7

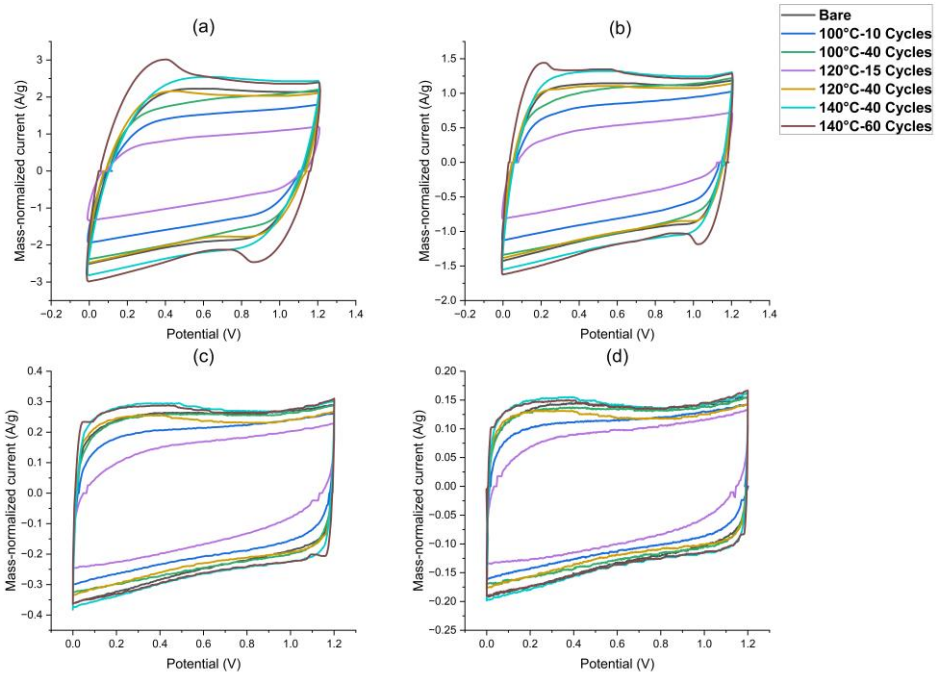

Figure 26. CV curves of SC devices at (a) 100 mV/s, (b) 50 mV/s, (c) 10 mV/s and (d) 5 mV/s

The highest CV curve areas are for 140°C-40 Cycles and 140°C-60 Cycles. The lowest CV curve areas are for 120°C-15 Cycles and 100°C-10 Cycles. However, a peculiar thing to note is the humps found for 140°C-60 Cycles sample at 100 and 50 mv/s scan rates. This is due to the potentiostat limitations. The Maccor 4300 system is optimized for battery testing and may not fully capture rapid electrochemical phenomena. The quick charging and discharging of supercapacitors, characterized by a small time constant (RC), can result in current transients that are recorded as anomalous peaks in the CV curves. This is the reason that these peaks disappear at slower scan rates.

5.2 Ellipsometry

The thickness measured on Si dummy wafers is depicted in Figure 27a below. The results in Figure 27b show that GPC stabilized around 0.4 Å/cycle, consistent with values reported by Ritala et al. for the same precursors [190].

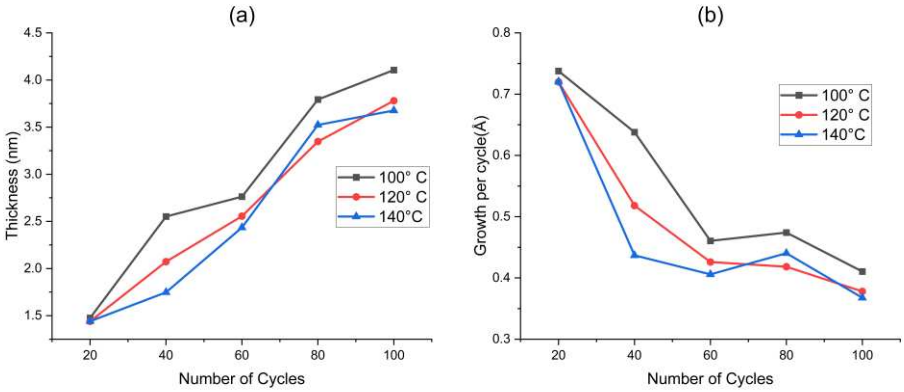

Figure 27. Thickness in (a) nanometers and (b) GPC, measured from Si dummy wafers.

The thickness values in Table 9 correspond to the two best-performing samples from each temperature, selected based on their capacitance in cyclic voltammetry (Section 4.5.1).

Table 9. Numerical values of ALD layer on the two selected samples from each temperature class.

Sample	Average thickness (nm)
100 °C-10 Cycles	
100°C-40 Cycles	≈2.6
120°C-15 Cycles	
120°C-40 Cycles	≈2.1
140°C-40 Cycles	≈1.7
140°C-60 Cycles	≈2.4

These values can also be compared to Table 3, which lists thicknesses reported in the literature for other supercapacitors that have also used ALD-coated metal oxides on activated carbon. The film thicknesses for the 5, 10, and 15-cycle samples could not be measured due to an unexpected malfunction of the ellipsometer.

5.3 GCD

The GCD curves of the supercapacitor devices are shown below.

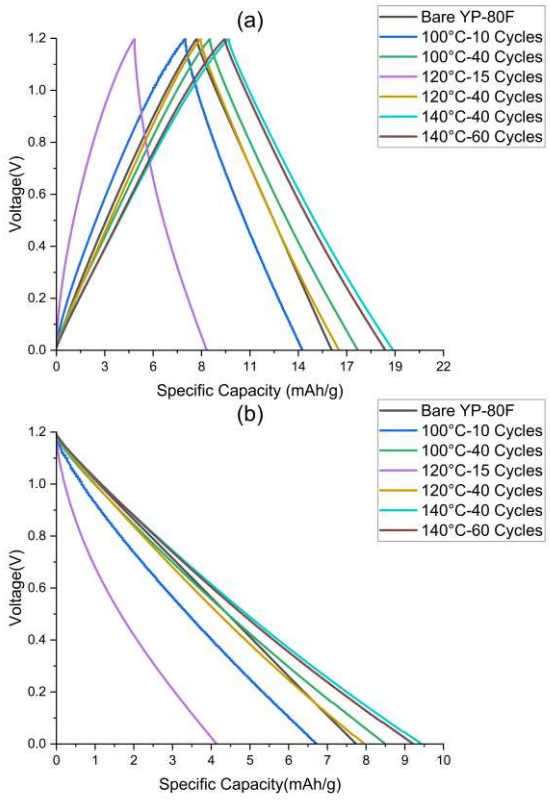

Figure 28. GCD curves from the fabricated SC devices, with (a) showing the GCD. After normalizing the discharge time by the active electrode mass, the voltage-specific capacity graph (b) is obtained.

Figure 28a. shows symmetrical triangles, representing EDLC behaviour (refer to Figure 11A). According to Figure 28b, electrodes coated at 120 °C show the worst overall performance. The 120°C – 15 cycles sample has the lowest specific capacity of all tested samples, and the 120°C – 40 cycles sample has a specific capacity nearly equal to that of the bare YP-80F. The 100 °C series shows moderate but varying performance, with the 100°C – 10 cycles sample possessing lower specific capacity and the 100°C – 40 cycles sample exceeding the bare material. The 140 °C series shows the best performance, with both the tested samples delivering the highest specific capacitances among all ALD-coated electrodes.

Overall, this variability indicates that the ALD process parameters have a non-linear effect on the resulting electrochemical performance, with no simple correlation emerging from the GCD results.

5.4 Cyclic stability

The numerical values of capacitance retention of each sample after 10000 cycles are given below in Table 10.

Table 10. Cyclic stability of the selected SC devices.

Sample	Capacitance retention (%)
Bare YP-80F	95.7
100°C-10 Cycles	101.3
100°C-40 Cycles	96.9
120°C-15 Cycles	95.1
120°C-40 Cycles	97.8
140°C-40 Cycles	96.9
140°C-60 Cycles	97.7

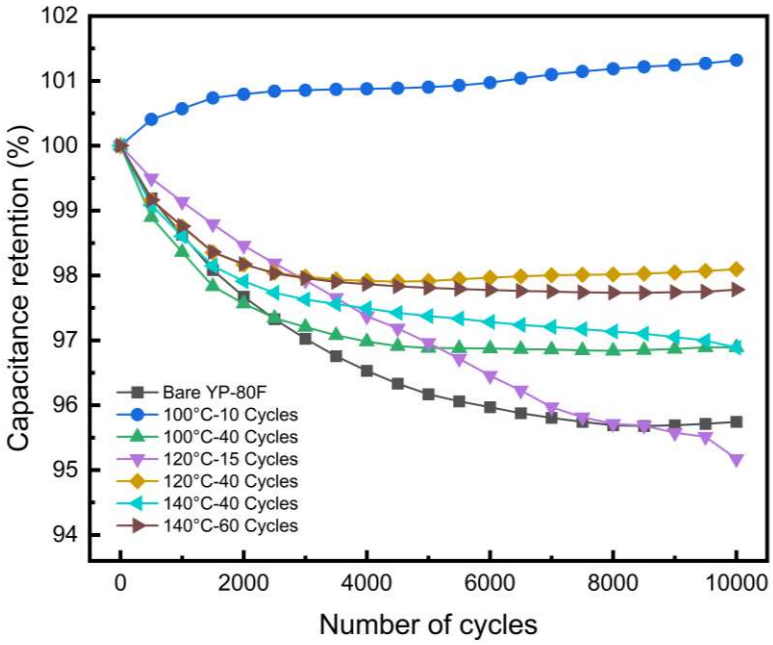

Figure 29. Cyclic stability graph of fabricated SC devices.

The bare YP-80F retains 95.7% of its initial capacitance after 10,000 cycles. Most ALD-coated samples perform slightly better, except 120°C-15 cycles sample. This indicates that ALD TiO_2 does not provide a significant enhancement in capacitance retention. 100°C-10 cycles sample, however, exhibits peculiar behaviour, achieving 101.3% retention.

The observation of capacitance retention exceeding 100% during extended cycling is well-documented in supercapacitor literature and reflects electrode activation. For instance, a graphene oxide-polyaniline (GO@PANI) nanocomposite demonstrated 118.6% capacitance retention after 10,000 cycles at 3 A g^{-1} with coulombic efficiency approaching 100% [191]. Similarly, a Co-HAB MOF supercapacitor retained 105.1% of its initial areal capacitance after 10,000 cycles at 0.75 mA cm^{-2} [192]. This phenomenon is consistently attributed to the activation of the electrode material through uninterrupted diffusion of electrolyte into open-porous channels, leading to enhanced wetting and an increasing number of charge storage sites [193].

Electrochemical impedance spectroscopy (EIS) is particularly valuable for studying this activation process. For example, in the GO@PANI system, EIS recorded after 1,000 cycles showed significantly reduced resistances compared to the pristine state, verifying that the electrode becomes progressively more activated and chemically stable even after 10,000 cycles [193]

5.5 Impedances

The impedances, also taken from Maccor 4300 GCD measurements, are given below in Table 11.

Table 11. Leakage current and ESR of SC devices

Sample	**ESR (Ω)**	**Leakage current (uA)**
Bare YP-80F	10.85	4.17
100 °C – 10 Cycles	11.91	6.69
100 °C – 40 Cycles	8.95	6.21
120 °C – 15 Cycles	12.87	7.21
120 °C – 40 Cycles	8.51	5.47
140 °C – 40 Cycles	9.95	4.97
140 °C – 60 Cycles	5.39	7.61

ESR results suggest that moderate-to-high cycle counts improve charge transport pathways at the electrode-electrolyte interface. However, lower-cycle depositions (10–15 cycles) result in elevated ESR values. It is however, important to note that the measured

ESR also includes impedance from the current collector, and the consistency of the contribution of the collector to ESR across tests has not been established.

All ALD-treated samples demonstrate higher leakage current values than pristine YP-80F, with the 120°C–15 cycles configuration showing a very high leakage current. The 140°C–40 cycles sample has the lowest capacitance amongst all the samples, while the 140°C–60 cycles sample exhibits unsually higher leakage, which can be considered as a measurement anomaly. The data indicates that no single optimal ALD condition simultaneously minimizes both parameters, as improvements in ESR might be offset by compromised leakage characteristics.

5.6 FESEM

Figure 30 shows the FESEM micrographs.

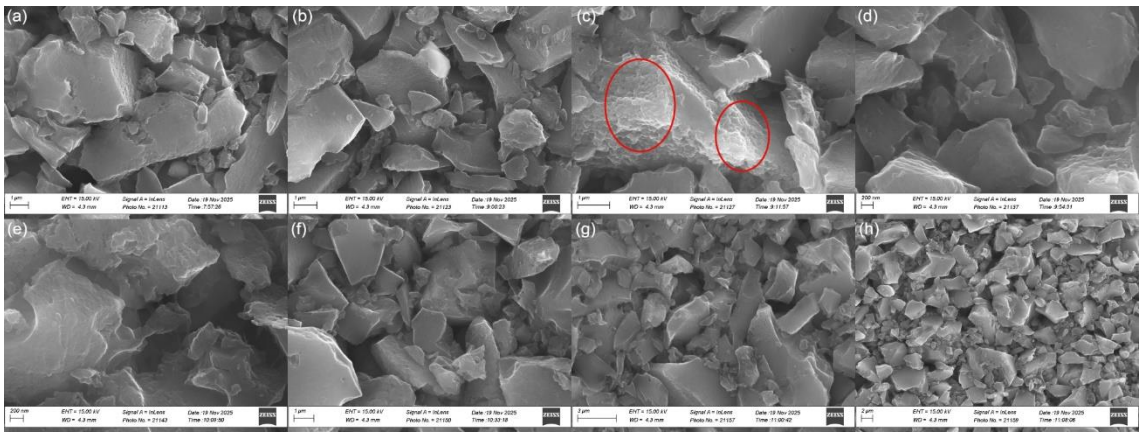

Figure 30. FESEM micrographs for electrode samples. Each subfigure corresponds to the specified sample and magnification, as follows: (a) 100°C–20 cycles before CV, 1.0 µm; (b) 100°C–20 cycles after CV, 1.0 µm; (c) 100°C–100 cycles before CV, 1.0 µm; (d) 100°C–10

FESEM micrographs obtained aligned with SEM micrographs of commercial ACs given in Figure 15. However, FESEM proved inconclusive in detecting any conformal TiO_2 deposition. The micrographs did not display any distinct morphology characteristic of TiO_2. The presence of an occasional bubble-like features in Figure 30c, enclosed by red circles, cannot be definitively attributed to the TiO_2 coating. Given that ALD typically yields a uniform and conformal surface layer, the absence of a consistent, observable texture across the carbon substrate suggested that the coating was either too thin to resolve or lacked distinct topographic contrast. HR-TEM could prove superior in visualizing the ALD-deposited layer, as was done in [33]. Therefore, to determine the success of the ALD process and confirm the presence of titanium, EDX spectroscopy and elemental mapping were conducted.

5.7 EDX

Elemental mapping (Table 12) provided definitive evidence for the uniform spatial distribution of titanium (Ti), which confirmed consistent TiO_2 coverage across the AC substrate. This was further supported by the homogeneous distribution of chlorine (Cl), a byproduct of the $TiCl_4$ and H_2O precursor reaction, which validates the completion of the intended ALD reaction.

Table 12. Elemental mapping showing spatial distribution of C, Ti, O and Cl

	C	Ti	O	Cl
100°C-20 cycles			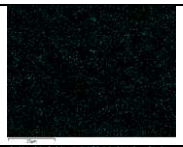	
100°C-80 cycles	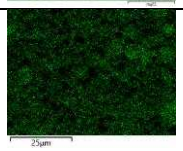		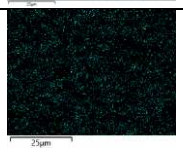	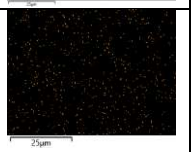
140°C-20 cycles	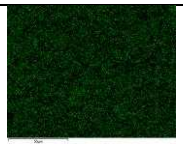		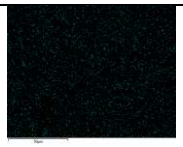	
140°C-80 cycles	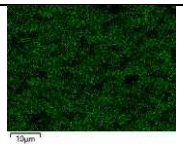	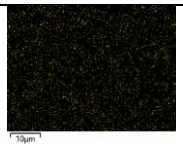	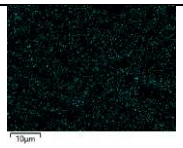	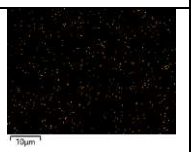

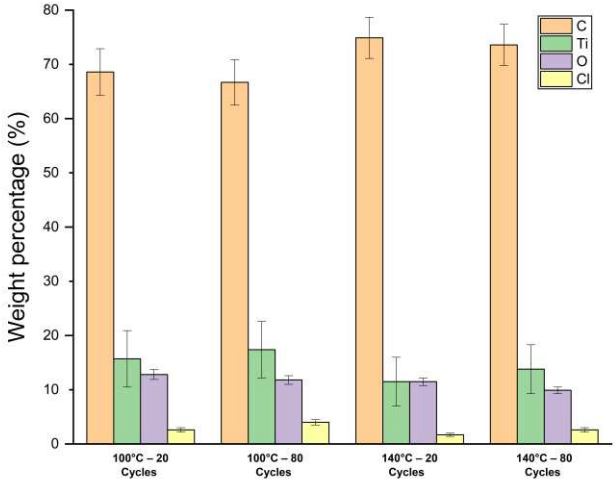

Figure 31. Weight percentage of different elements in TiO_2-ALDed samples, obtained from EDX

Furthermore, the weight percentage analysis (Figure 31) also confirmed a successful ALD TiO_2 operation. An increase in titanium weight percentage with increasing number of cycles from 20 to 80 at both deposition temperatures was observed. This increase was accompanied by a corresponding decrease in carbon content. The concurrent rise in chlorine content also validated the deposition process. However, while EDX quantitatively tracks elemental composition changes, it cannot provide insights into coating morphology or uniformity.

5.8 Raman

The Raman spectra (Figure 32) are dominated by two key components, the broad D (~1350 cm^{-1}) and G (~1580 cm^{-1}) bands of the YP-80F substrate. Most samples show no TiO_2 crystalline peaks. This means that for most of the samples, the TiO_2 coating is not highly crystalline anatase but rather a disordered, amorphous layer, which is common for low-temperature ALD processes. 120°C-40 cycles (After CV) sample (Figure 32 After CV) showed the distinct, sharp peak of crystalline anatase TiO_2 However, this was noted as an outlier, since further measurements on the same sample (Figure 32) did not detect any anatase measurements, suggesting this isolated crystallinity is not the representative of the whole sample.

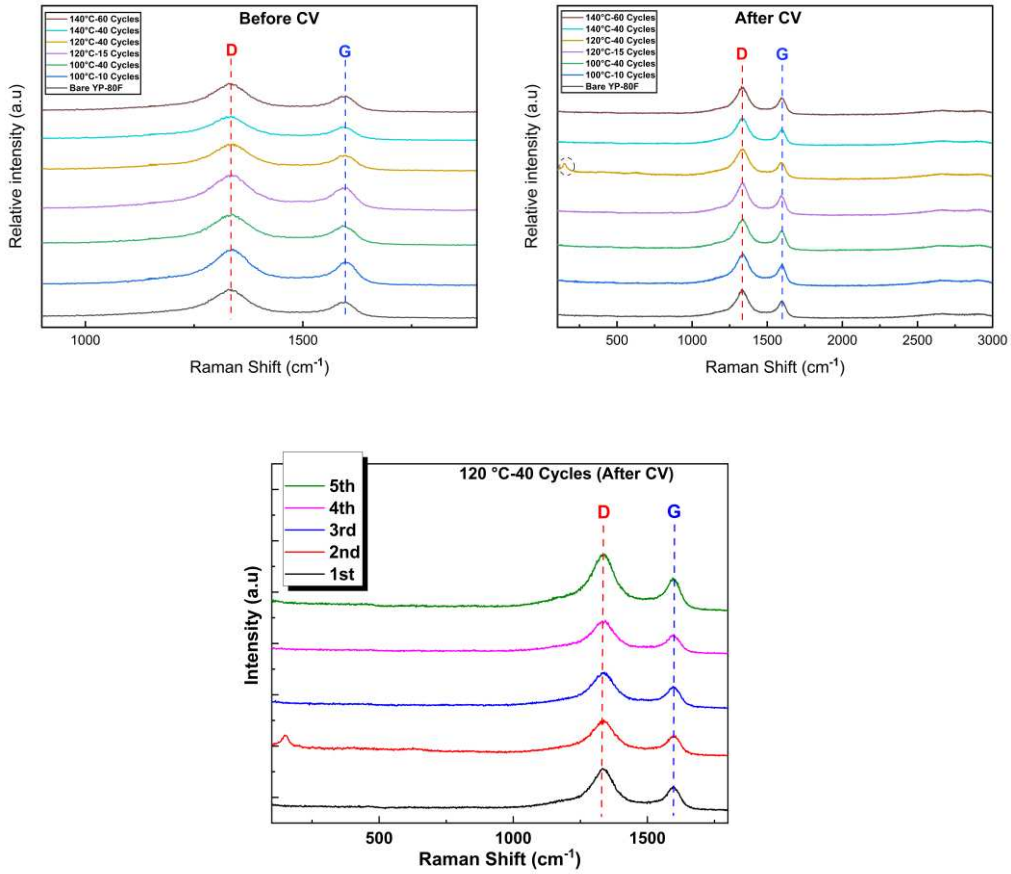

Figure 32. Raman spectrographs of the samples before and after CV, and 120 °C-40 Cycles after CV.

Furthermore, comparing the (ID/IG) ratio of samples before (b) and after (a) CV would also reveal if the amorphous TiO_2 layer provided any protective effect against carbon corrosion during the electrochemical cycling. These would be shown in Table 13.

Table 13. ID/IG ratios of samples before and after CV

Sample	I_D	I_G	$FWHM_G$ (cm^{-1})	I_D/I_G
YP-80F	3.56×10^5	1.56×10^5	47.5	2.29
100 °C-10 Cycles-a	9420	3270	46.9	2.88
100 °C-10 Cycles-b	11200	4930	49.8	2.27
100 °C-40 Cycles-a	8640	3390	50.5	2.55
100 °C-40 Cycles-b	6960	2740	52.5	2.54
120 °C-15 Cycles-a	8150	2830	49.2	2.88
120 °C-15 Cycles-b	8660	3370	51.0	2.57
120 °C-40 Cycles-a	7030	2500	51.5	2.81
120 °C-40 Cycles-b	6660	2320	52.6	2.87
140 °C-40 Cycles-a	7090	2400	49.0	2.95
140 °C-40 Cycles-b	6540	2180	49.5	2.99
140 °C-60 Cycles-a	6350	2350	48.4	2.71
140 °C-60 Cycles-b	7010	2610	51.6	2.68

Some information from the ID/IG ratio can be extracted regarding the effectiveness of the TiO_2 layer in protecting the underlying carbon structure from electrochemical degradation during cyclic voltammetry (CV). This ratio is a common indicator of disorder in carbon materials. For samples with a lower number of TiO_2 -ALD cycles, e.g. 100°C-10 cycles and 120°C-15 cycles, the ID/IG ratio increased significantly after CV (from 2.27 to 2.88 and from 2.57 to 2.88, respectively). This suggests that the cycling introduces substantial structural defects or disorder in these less protected activated carbon samples. For samples with a thicker TiO_2 layer (higher number of cycles), like 100°C-40 cycles (from ~2.54 to 2.55) and 140°C-60 Cycles (from 2.68 to 2.71), the ID/IG ratio remains remarkably stable. In fact, for the 120°C-40 cycles and 140°C-40 cycles samples, the ratio even slightly decreased after CV, which could suggest a minor annealing effect or the removal of unstable defect sites. This overall stability demonstrates that a thicker TiO_2 layer, achieved with a higher number of deposition cycles, provides effective protection, maintaining the structural integrity of the carbon during electrochemical cycling.

The interpretation of the TiO_2 coating itself from Raman data is however, limited. While most TiO_2-coated AC samples exhibit a higher ID/IG ratio than the pristine carbon, suggesting an increase in surface defects, this signal originates from the underlying activated carbon, not the TiO_2 coating itself, as amorphous TiO_2 is Raman-inactive [194]. Furthermore, the protective phenomenon provided by the deposited TiO_2 should further be verified through other characterizations. XPS could detect chemical changes on the carbon surface indicative of oxidation [33].

5.9 XRD

The results of XRD, taken from the Si dummy samples, are given in Figure 33. Reference spectra for graphite (RRUFFID No. R050503) and silicon (RRUFFID No. R050145) are also added.

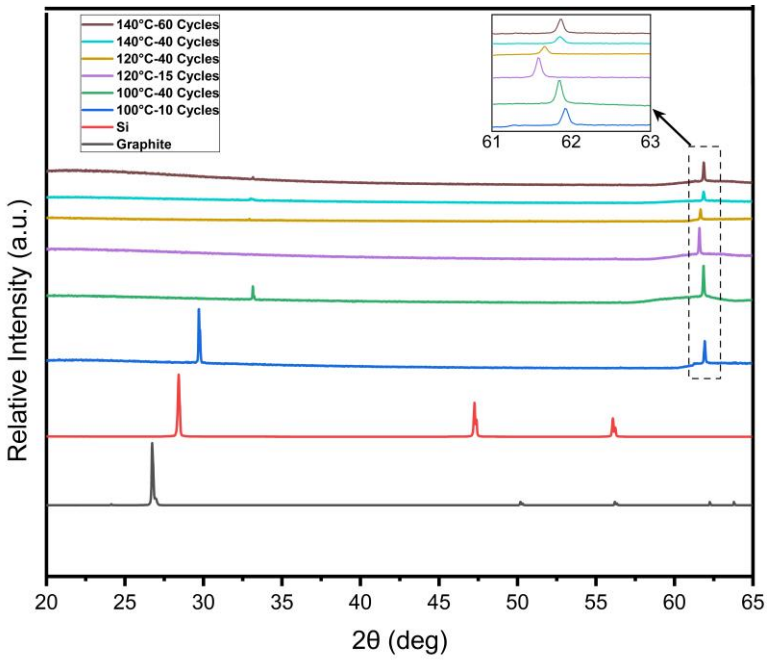

Figure 33. XRD diffractogram for ALD-deposited TiO_2 layers, taken from an S dummy sample

It must be noted that the results from the Rigaku Miniflex 600 are not reliable for these thin film samples. Sporadic peak around 33° in some samples may correspond to the Si (200) peak from the underlying silicon wafer, and it can seem that its signal decreases at higher number of ALD-cycles. However, no clear peaks corresponding to crystalline TiO_2 phases (e.g., anatase or rutile) can be resolved, even in slow-speed measurements. Instead, the noticeable amorphous hump in the low 20-degree region of the diffractograms provides evidence for the presence of a non-crystalline material. Thus, the only tentative conclusion from XRD regarding the coating itself is that it consists of an amorphous film, with no detectable crystalline TiO_2 present, and this could alternatively be attributed to the layer being too thin to produce measurable diffraction peaks For thin film analysis, GIXRD (Grazing-Incidence X-ray Diffraction) would be more reliable because of its limited penetration depth, enhanced surface sensitivity, and substrate signal suppression [195].

6. CONCLUSIONS AND FUTURE RESEARCH

The electrochemical characterizations of ALD-deposited TiO_2 on commercial YP-80F activated carbon electrodes demonstrated minimal performance enhancement. Analysis of specific capacitance values, derived from both three-electrode and two-electrode configurations, revealed no clear, consistent trend correlating ALD parameters (temperature and cycle number) with improved charge storage capability. Similarly, cyclic stability testing showed no meaningful improvement in capacitance retention for the modified electrodes compared to pristine YP-80F. Notably, the leakage current increased for all ALD-treated samples relative to the bare electrode, indicating potential degradation of interfacial properties. However, within the two-electrode device characterizations, the 140 °C temperature class (specifically the 40 and 60 ALD cycles samples) exhibited marginal performance among the tested conditions. The unusually high leakage current observed for the 140 °C–60 cycles sample may reasonably be attributed to measurement error or device-specific anomalies.

Based on these electrochemical results, it can be tentatively suggested that ALD-deposited TiO_2 does not significantly enhance the electrochemical performance of YP-80F as a negative electrode material under the investigated conditions. However, this conclusion is substantially limited by the experimental design and scope of this work. Several critical factors prevent a definitive judgment.

First, the statistical robustness of the data is insufficient. A proper evaluation would require a minimum of three replicate samples for each specific ALD condition (temperature and cycle number) to statistically account for measurement variability and random instrumental errors. This replication was not performed due to time constraints, leaving the results vulnerable to single-sample anomalies and precluding reliable statistical analysis.

Second, the electrochemical characterization protocols lacked consistency. The two-electrode device testing should have been conducted within the same voltage window (-1.0 V to 0 V vs. Ag/AgCl) used for the three-electrode CV screening to enable direct, fair comparison and proper correlation between screening and device-level performance. The difference in voltage windows prevents a fair comparison.

Regarding materials characterizations, FESEM imaging failed to reveal any distinct morphological features attributable to the ALD coating, likely due to the ultrathin, conformal nature of the deposited layers. However, EDX elemental mapping successfully confirmed the presence and uniform distribution of titanium, validating that the ALD process

occurred as intended. Raman spectroscopy indicated increasing defect density on the activated carbon substrate with higher ALD cycle counts, though no clear, systematic trend emerged. Both XRD and Raman analyses consistently showed that the deposited TiO_2 was amorphous rather than crystalline, which may partially explain the lack of pseudocapacitive enhancement.

The materials characterization plan could be significantly strengthened in future work. XPS would provide critical insight into surface functional groups due to ALD procedure. HR-TEM could directly visualize the conformality and thickness of the TiO_2 nanofilms, while GIXRD would offer far more reliable results for phase identification in thin-film samples compared to conventional XRD. Additionally, EIS analysis before and after cyclic stability tests could help in better understanding the electrode-electrolyte interaction phenomena, and thence the device performance**.**

Thus, based solely on the available results from this study, it cannot be definitively concluded that ALD-deposited TiO_2 enhances the performance of YP-80F electrodes. While the data tentatively suggests that ALD-TiO_2 is not an effective modification strategy under the tested conditions, the noted experimental limitations preclude a complete and final determination. Future investigations can be carried out to address these methodological gaps to conclusively establish the viability of ALD-TiO_2/AC for negative electrode application in supercapacitors.

REFERENCES

[1] S. Verma et al., ‘A comprehensive review on energy storage in hybrid electric vehicle’, J. Traffic Transp. Eng. Engl. Ed., vol. 8, no. 5, pp. 621–637, Oct. 2021, doi: 10.1016/j.jtte.2021.09.001.

[2] R. Gupta, A. Kumar, A. Biswas, A. S. Verma, and T. Kumar, ‘Advances in nanostruc-tured energy harvesting and energy storage for portable electronic devices’, Polym. Bull., vol. 82, no. 16, pp. 10721–10761, Nov. 2025, doi: 10.1007/s00289-025-05983-1.

[3] J. Maeng et al., ‘A supercapacitor size minimization and energy management strategy for E-STATCOM connected to weak grid’, Int. J. Electr. Power Energy Syst., vol. 172, p. 111174, Nov. 2025, doi: 10.1016/j.ijepes.2025.111174.

[4] H. Rashid Khan and A. Latif Ahmad, ‘Supercapacitors: Overcoming current limitations and charting the course for next-generation energy storage’, J. Ind. Eng. Chem., vol. 141, pp. 46–66, Jan. 2025, doi: 10.1016/j.jiec.2024.07.014.

[5] O. B. Okafor, A. P. I. Popoola, O. M. Popoola, and S. O. Adeosun, ‘The Influence of Graphene–Titanium Nitride and Synthesis Parameters on the Electrochemical Properties of Pol-yaniline Nanocomposite’, J. Electron. Mater., vol. 54, no. 12, pp. 11778–11794, Dec. 2025, doi: 10.1007/s11664-025-12417-1.

[6] B. Y. León Ávila, C. A. García Vázquez, O. Pérez Baluja, D. T. Cotfas, and P. A. Cotfas, ‘Energy harvesting techniques for wireless sensor networks: A systematic literature review’, Energy Strategy Rev., vol. 57, p. 101617, Jan. 2025, doi: 10.1016/j.esr.2024.101617.

[7] C. V. V. Muralee Gopi, S. Alzahmi, V. Narayanaswamy, R. Vinodh, B. Issa, and I. M. Obaidat, ‘Supercapacitors: A promising solution for sustainable energy storage and diverse applications’, J. Energy Storage, vol. 114, p. 115729, Apr. 2025, doi: 10.1016/j.est.2025.115729.

[8] S. Rani et al., ‘Flexible self-powered supercapacitors integrated with triboelectric nanogenerators’, Energy Storage Mater., vol. 74, p. 103977, Jan. 2025, doi: 10.1016/j.ensm.2024.103977.

[9] S. Najib and E. Erdem, ‘Current progress achieved in novel materials for supercapacitor electrodes: mini review’, Nanoscale Adv., vol. 1, no. 8, pp. 2817–2827, 2019, doi: 10.1039/C9NA00345B.

[10] K. Kierzek and G. Gryglewicz, ‘Activated Carbons and Their Evaluation in Electric Double Layer Capacitors’, Molecules, vol. 25, no. 18, p. 4255, Sept. 2020, doi: 10.3390/molecules25184255.

[11] ‘Kuraray Activated Carbon powder YP-80F, high power grade’, Cambridge Energy Solutions. Accessed: Dec. 15, 2025. [Online]. Available: https://www.cam-energy.com/shop/ku-yp-80-kuraray-activated-carbon-powder-yp-80f-high-power-grade-1801

[12] ‘YP-80F Activated Carbon for Supercapacitors’. Accessed: Dec. 15, 2025. [Online]. Available: https://www.aooser.com/product/YP-80F-Activated-Carbon-for-Supercapacitors.html

[13] S. Mallick, S. Bag, and C. Retna Raj, ‘Supercapacitors for energy storage: Fundamen-tals and materials design’, J. Chem. Sci., vol. 137, no. 3, p. 65, Aug. 2025, doi: 10.1007/s12039-025-02394-7.

[14] F. Zhang, G. Song, D. Gandla, Y. Ein-Eli, and D. Q. Tan, ‘Synergy of Oxygen Plasma and Al2O3 Atomic Layer Deposition on Improved Electrochemical Stability of Activated Car-bon-Based Supercapacitor’, Front. Energy Res., vol. 9, p. 653203, Apr. 2021, doi: 10.3389/fenrg.2021.653203.

[15] S. Balasubramaniam, A. Mohanty, S. K. Balasingam, S. J. Kim, and A. Ramadoss, ‘Comprehensive Insight into the Mechanism, Material Selection and Performance Evaluation of Supercapatteries’, Nano-Micro Lett., vol. 12, no. 1, p. 85, Dec. 2020, doi: 10.1007/s40820-020-0413-7.

[16] A. González, E. Goikolea, J. A. Barrena, and R. Mysyk, ‘Review on supercapacitors: Technologies and materials’, Renew. Sustain. Energy Rev., vol. 58, pp. 1189–1206, May 2016, doi: 10.1016/j.rser.2015.12.249.

[17] A. Güngör, A. U. Ammar, A. M. Rostas, and E. Erdem, ‘Defect structures in superca-pacitor electrodes: non-oxide 2D materials and metal oxides’, J. Mater. Chem. A, vol. 13, no. 42, pp. 36030–36055, 2025, doi: 10.1039/D5TA04716A.

[18] L. Zhang, Q. Song, C. Wang, X. Liu, X. Jiang, and J. Gong, 'The Electrode Materials of Supercapacitor Based on TiO2 Nanorod/MnO2 Ultrathin Nanosheet Core/Shell Arrays', J. Nanomater., vol. 2020, pp. 1–11, Dec. 2020, doi: 10.1155/2020/6642236.

[19] J. Zhi, H. Cui, Z. Wang, and F. Huang, 'Surface confined titania redox couple for ultra-fast energy storage', Mater. Horiz., vol. 5, no. 4, pp. 691–698, 2018, doi: 10.1039/C8MH00112J.

[20] A. Mir et al., 'Strategic Ti3+ incorporation in TiO_2 nanotube arrays via microwave-promoted borohydride reduction for high-performance energy storage', Electrochimica Acta, vol. 546, p. 147743, Jan. 2026, doi: 10.1016/j.electacta.2025.147743.

[21] L. Fornasini et al., 'In situ decoration of laser-scribed graphene with TiO2 nanoparticles for scalable high-performance micro-supercapacitors', Carbon, vol. 176, pp. 296–306, May 2021, doi: 10.1016/j.carbon.2021.01.129.

[22] C. C. Raj, V. Srimurugan, A. Flamina, and R. Prasanth, 'Tuning the carrier density of TiO2 nanotube arrays by controlling the oxygen vacancies for improved areal capacitance in supercapacitor applications', Mater. Chem. Phys., vol. 248, p. 122925, July 2020, doi: 10.1016/j.matchemphys.2020.122925.

[23] P. Pazhamalai, K. Krishnamoorthy, V. K. Mariappan, and S.-J. Kim, 'Blue TiO2 nanosheets as a high-performance electrode material for supercapacitors', J. Colloid Interface Sci., vol. 536, pp. 62–70, Feb. 2019, doi: 10.1016/j.jcis.2018.10.031.

[24] Q. Ke, M. Zheng, H. Liu, C. Guan, L. Mao, and J. Wang, '3D TiO2@Ni(OH)2 Core-shell Arrays with Tunable Nanostructure for Hybrid Supercapacitor Application', Sci. Rep., vol. 5, no. 1, p. 13940, Sept. 2015, doi: 10.1038/srep13940.

[25] J. Aftab et al., 'Synergetic electrochemical performance of tungsten oxide/tungsten di-sulfide/MWCNTs for high-performance aqueous asymmetric supercapattery devices', J. Alloys Compd., vol. 965, p. 171366, Nov. 2023, doi: 10.1016/j.jallcom.2023.171366.

[26] C. V. V. M. Gopi et al., 'Recent advances in pseudocapacitive electrode materials for high energy density aqueous supercapacitors: Combining transition metal oxides with carbon nanomaterials', Mater. Today Sustain., vol. 28, p. 100981, Dec. 2024, doi: 10.1016/j.mtsust.2024.100981.

[27] L. Xu, M. Jia, Y. Li, S. Zhang, and X. Jin, 'Design and synthesis of graphene/activated carbon/polypyrrole flexible supercapacitor electrodes', RSC Adv., vol. 7, no. 50, pp. 31342–31351, 2017, doi: 10.1039/C7RA04566B.

[28] Z. Li, J. Su, and X. Wang, 'Atomic layer deposition in the development of supercapaci-tor and lithium-ion battery devices', Carbon, vol. 179, pp. 299–326, July 2021, doi: 10.1016/j.carbon.2021.03.041.

[29] R. Taylor, S. B. Venkata Siva, and P. S. Rama Sreekanth, '5.14 Carbon Matrix Composites', in Comprehensive Composite Materials II, Elsevier, 2018, pp. 339–378. doi: 10.1016/B978-0-12-803581-8.03905-9.

[30] D. Escorcia-Díaz, S. García-Mora, L. Rendón-Castrillón, M. Ramírez-Carmona, and C. Ocampo-López, 'Advancements in Nanoparticle Deposition Techniques for Diverse Substrates: A Review', Nanomaterials, vol. 13, no. 18, p. 2586, Sept. 2023, doi: 10.3390/nano13182586.

[31] R. W. Johnson, A. Hultqvist, and S. F. Bent, 'A brief review of atomic layer deposition: from fundamentals to applications', Mater. Today, vol. 17, no. 5, pp. 236–246, June 2014, doi: 10.1016/j.mattod.2014.04.026.

[32] D. Gandla and D. Q. Tan, 'Progress Report on Atomic Layer Deposition Toward Hybrid Nanocomposite Electrodes for Next Generation Supercapacitors', Adv. Mater. Interfaces, vol. 6, no. 16, p. 1900678, Aug. 2019, doi: 10.1002/admi.201900678.

[33] R. I. M. Vitto et al., 'Interfacial engineering of conformal titanium oxide nanofilms on porous carbon supercapacitor electrodes via atomic layer deposition', J. Power Sources, vol. 662, p. 238691, Jan. 2026, doi: 10.1016/j.jpowsour.2025.238691.

[34] K. Dissanayake and D. Kularatna-Abeywardana, 'A review of supercapacitors: Materials, technology, challenges, and renewable energy applications', J. Energy Storage, vol. 96, p. 112563, Aug. 2024, doi: 10.1016/j.est.2024.112563.

[35] N. Singh et al., 'A comprehensive review on supercapacitors: Basics to recent ad-vancements', J. Energy Storage, vol. 121, p. 116498, June 2025, doi: 10.1016/j.est.2025.116498.

[36] D. I. Abouelamaiem, 'Exploring the Synergy of Functionalised Bio-carbons and their Performance in Supercapacitor Devices'.

[37] A. Kattainen, ‘Deep-eutectic-solvent-based supercapacitor for single-use medical diagnostics’, 2025, Accessed: Dec. 15, 2025. [Online]. Available: https://trepo.tuni.fi/handle/10024/228594

[38] A. G. Pandolfo and A. F. Hollenkamp, ‘Carbon properties and their role in supercapacitors’, J. Power Sources, vol. 157, no. 1, pp. 11–27, June 2006, doi: 10.1016/j.jpowsour.2006.02.065.

[39] S. Roldán, M. Granda, R. Menéndez, R. Santamaría, and C. Blanco, ‘Supercapacitor modified with methylene blue as redox active electrolyte’, Electrochimica Acta, vol. 83, pp. 241–246, Nov. 2012, doi: 10.1016/j.electacta.2012.08.026.

[40] S. Roldán, C. Blanco, M. Granda, R. Menéndez, and R. Santamaría, ‘Towards a Further Generation of High-Energy Carbon-Based Capacitors by Using Redox-Active Electrolytes’, Angew. Chem. Int. Ed., vol. 50, no. 7, pp. 1699–1701, Feb. 2011, doi: 10.1002/anie.201006811.

[41] M. Chiku, ‘Electrical Double-Layer Capacitors (EDLC)’, in Encyclopedia of Applied Electrochemistry, G. Kreysa, K. Ota, and R. F. Savinell, Eds, New York, NY: Springer New York, 2014, pp. 384–386. doi: 10.1007/978-1-4419-6996-5_505.

[42] J. W. Graydon, M. Panjehshahi, and D. W. Kirk, ‘Charge redistribution and ionic mobility in the micropores of supercapacitors’, J. Power Sources, vol. 245, pp. 822–829, Jan. 2014, doi: 10.1016/j.jpowsour.2013.07.036.

[43] R. Parsons, ‘The kinetics of electrode reactions and the electrode material’, Surf. Sci., vol. 2, pp. 418–435, Jan. 1964, doi: 10.1016/0039-6028(64)90083-4.

[44] D. C. Grahame, ‘The Electrical Double Layer and the Theory of Electrocapillarity.’, Chem. Rev., vol. 41, no. 3, pp. 441–501, Dec. 1947, doi: 10.1021/cr60130a002.

[45] V. Sudha and M. V. Sangaranarayanan, ‘Underpotential Deposition of Metals: Structural and Thermodynamic Considerations’, J. Phys. Chem. B, vol. 106, no. 10, pp. 2699–2707, Mar. 2002, doi: 10.1021/jp013544b.

[46] H. Li et al., ‘Carbon electrode with conductivity improvement using silver nanowires for high-performance supercapacitor’, Appl. Phys. A, vol. 124, no. 11, p. 763, Nov. 2018, doi: 10.1007/s00339-018-2182-4.

[47] D. Chen, Q. Tao, L. W. Liao, S. X. Liu, Y. X. Chen, and S. Ye, ‘Determining the Active Surface Area for Various Platinum Electrodes’, Electrocatalysis, vol. 2, no. 3, pp. 207–219, Sept. 2011, doi: 10.1007/s12678-011-0054-1.

[48] M. Shao, J. H. Odell, S.-I. Choi, and Y. Xia, ‘Electrochemical surface area measure-ments of platinum- and palladium-based nanoparticles’, Electrochem. Commun., vol. 31, pp. 46–48, June 2013, doi: 10.1016/j.elecom.2013.03.011.

[49] K. K. Kar, Ed., Handbook of Nanocomposite Supercapacitor Materials II: Performance, vol. 302. in Springer Series in Materials Science, vol. 302. Cham: Springer International Publishing, 2020. doi: 10.1007/978-3-030-52359-6.

[50] V. Augustyn, P. Simon, and B. Dunn, ‘Pseudocapacitive oxide materials for high-rate electrochemical energy storage’, Energy Environ. Sci., vol. 7, no. 5, p. 1597, 2014, doi: 10.1039/c3ee44164d.

[51] P. GIANNAKOU, ‘Printed Transition Metal Oxide Electrochemical Capacitors for Energy Harvesting Applications’, 2021, doi: 10.15126/THESIS.900042.

[52] H. Pourkheirollah, Printed Supercapacitors for Energy Storage and Functional Applications, Modeling, Analysis, and Integration. Tampere University, 2023. Accessed: Dec. 16, 2025. [Online]. Available: https://trepo.tuni.fi/handle/10024/152842

[53] A. Willfahrt, E. Steiner, J. Hötzel, and X. Crispin, ‘Printable acid-modified corn starch as non-toxic, disposable hydrogel-polymer electrolyte in supercapacitors’, Appl. Phys. A, vol. 125, no. 7, p. 474, July 2019, doi: 10.1007/s00339-019-2767-6.

[54] L. Lai et al., ‘Preparation of Supercapacitor Electrodes through Selection of Graphene Surface Functionalities’, ACS Nano, vol. 6, no. 7, pp. 5941–5951, July 2012, doi: 10.1021/nn3008096.

[55] K. D. Verma, P. Sinha, S. Banerjee, and K. K. Kar, ‘Characteristics of Electrode Materials for Supercapacitors’, in Handbook of Nanocomposite Supercapacitor Materials I, vol. 300, K. K. Kar, Ed., in Springer Series in Materials Science, vol. 300. , Cham: Springer International Publishing, 2020, pp. 269–285. doi: 10.1007/978-3-030-43009-2_9.

[56] F. Qi et al., ‘Graphitization induced by KOH etching for the fabrication of hierarchical porous graphitic carbon sheets for high performance supercapacitors’, J. Mater. Chem. A, vol. 6, no. 29, pp. 14170–14177, 2018, doi: 10.1039/C8TA01186A.

[57] X. He, H. Ma, J. Wang, Y. Xie, N. Xiao, and J. Qiu, ‘Porous carbon nanosheets from coal tar for high-performance supercapacitors’, J. Power Sources, vol. 357, pp. 41–46, July 2017, doi: 10.1016/j.jpowsour.2017.04.108.

[58] E. Yilmazoğlu and S. Karakuş, ‘Recent Developments in Nanostructured Materials for Supercapacitor Electrodes’, J. Turk. Chem. Soc. Sect. Chem., vol. 10, no. 4, pp. 1107–1122, Nov. 2023, doi: 10.18596/jotcsa.1320655.

[59] D. Ionescu and D. Butnicu, ‘Influence of the Electrodes Porosity on the Supercapaci-tors’ Charging Performance’, in 2024 IEEE 30th International Symposium for Design and Tech-nology in Electronic Packaging (SIITME), Sibiu, Romania: IEEE, Oct. 2024, pp. 471–474. doi: 10.1109/SIITME63973.2024.10814760.

[60] R. Mysyk, E. Raymundo-Piñero, and F. Béguin, ‘Saturation of subnanometer pores in an electric double-layer capacitor’, Electrochem. Commun., vol. 11, no. 3, pp. 554–556, Mar. 2009, doi: 10.1016/j.elecom.2008.12.035.

[61] G. Gryglewicz, J. Machnikowski, E. Lorenc-Grabowska, G. Lota, and E. Frackowiak, ‘Effect of pore size distribution of coal-based activated carbons on double layer capacitance’, Electrochimica Acta, vol. 50, no. 5, pp. 1197–1206, Jan. 2005, doi: 10.1016/j.electacta.2004.07.045.

[62] C. Arbizzani, ‘New trends in electrochemical supercapacitors’, J. Power Sources, vol. 100, no. 1–2, pp. 164–170, Nov. 2001, doi: 10.1016/S0378-7753(01)00892-8.

[63] E. Raymundo-Piñero, K. Kierzek, J. Machnikowski, and F. Béguin, ‘Relationship be-tween the nanoporous texture of activated carbons and their capacitance properties in different electrolytes’, Carbon, vol. 44, no. 12, pp. 2498–2507, Oct. 2006, doi: 10.1016/j.carbon.2006.05.022.

[64] E. Frackowiak and F. Béguin, ‘Carbon materials for the electrochemical storage of energy in capacitors’, Carbon, vol. 39, no. 6, pp. 937–950, May 2001, doi: 10.1016/S0008-6223(00)00183-4.

[65] C. Zhong, Y. Deng, W. Hu, J. Qiao, L. Zhang, and J. Zhang, ‘A review of electrolyte materials and compositions for electrochemical supercapacitors’, Chem. Soc. Rev., vol. 44, no. 21, pp. 7484–7539, 2015, doi: 10.1039/C5CS00303B.

[66] A. Mendhe and H. S. Panda, ‘A review on electrolytes for supercapacitor device’, Dis-cov. Mater., vol. 3, no. 1, p. 29, Oct. 2023, doi: 10.1007/s43939-023-00065-3.

[67] H. D. Dawoud, T. Al Tahtamouni, and N. Bensalah, ‘Sputtered manganese oxide thin film on carbon nanotubes sheet as a flexible and binder-free electrode for supercapacitors’, Int. J. Energy Res., vol. 43, no. 3, pp. 1245–1254, Mar. 2019, doi: 10.1002/er.4364.

[68] L. Peng et al., ‘Mixed-Biomass Wastes Derived Hierarchically Porous Carbons for High-Performance Electrochemical Energy Storage’, ACS Sustain. Chem. Eng., vol. 7, no. 12, pp. 10393–10402, June 2019, doi: 10.1021/acssuschemeng.9b00477.

[69] H. A. Ghaly, A. G. El-Deen, E. R. Souaya, and N. K. Allam, ‘Asymmetric supercapaci-tors based on 3D graphene-wrapped V2O5 nanospheres and Fe3O4@3D graphene electrodes with high power and energy densities’, Electrochimica Acta, vol. 310, pp. 58–69, July 2019, doi: 10.1016/j.electacta.2019.04.071.

[70] P. Wang et al., ‘Manganese oxide(Ⅲ)/carbon hybrids with interesting morphologies as improved active materials for supercapacitors’, Int. J. Hydrog. Energy, vol. 44, no. 26, pp. 13623–13631, May 2019, doi: 10.1016/j.ijhydene.2019.03.240.

[71] X. Guo, Z. Luan, Y. Lu, L. Fu, and L. Gai, ‘NaTi2(PO4)3/C‖carbon package asymmetric flexible supercapacitors with the positive material recycled from spent Zn–Mn dry batteries’, J. Alloys Compd., vol. 782, pp. 576–585, Apr. 2019, doi: 10.1016/j.jallcom.2018.12.163.

[72] Y.-J. Heo, H. I. Lee, J. W. Lee, M. Park, K. Y. Rhee, and S.-J. Park, ‘Optimization of the pore structure of PAN-based carbon fibers for enhanced supercapacitor performances via electrospinning’, Compos. Part B Eng., vol. 161, pp. 10–17, Mar. 2019, doi: 10.1016/j.compositesb.2018.10.026.

[73] Y. Song et al., ‘Simultaneously Blocking Chemical Crosstalk and Internal Short Circuit via Gel-Stretching Derived Nanoporous Non-Shrinkage Separator for Safe Lithium-Ion Batter-ies’, Adv. Mater., vol. 34, no. 2, p. 2106335, Jan. 2022, doi: 10.1002/adma.202106335.

[74] H. Wu, J. Mu, Y. Xu, F. Xu, S. Ramaswamy, and X. Zhang, ‘Heat-Resistant, Robust, and Hydrophilic Separators Based on Regenerated Cellulose for Advanced Supercapacitors’, Small, vol. 19, no. 1, p. 2205152, Jan. 2023, doi: 10.1002/smll.202205152.

[75] S. Zhong et al., ‘Recent progress in thin separators for upgraded lithium ion batteries’, Energy Storage Mater., vol. 41, pp. 805–841, Oct. 2021, doi: 10.1016/j.ensm.2021.07.028.

[76] D. Guo, L. Mu, F. Lin, and G. Liu, ‘Mesoporous Polyimide Thin Films as Dendrite-Suppressing Separators for Lithium–Metal Batteries’, ACS Nano, vol. 18, no. 1, pp. 155–163, Jan. 2024, doi: 10.1021/acsnano.3c04159.

[77] M. Liu, K. Turcheniuk, W. Fu, Y. Yang, M. Liu, and G. Yushin, ‘Scalable, safe, high-rate supercapacitor separators based on the Al2O3 nanowire Polyvinyl butyral nonwoven membranes’, Nano Energy, vol. 71, p. 104627, May 2020, doi: 10.1016/j.nanoen.2020.104627.

[78] R. Mendoza, J. Oliva, and V. Rodriguez-Gonzalez, ‘Effect of the micro-, meso- and macropores on the electrochemical performance of supercapacitors: A review’, Int. J. Energy Res., vol. 46, no. 6, pp. 6989–7020, May 2022, doi: 10.1002/er.7670.

[79] C. Lekakou et al., ‘AUTOSUPERCAP: Development of High Energy and High Power Density Supercapacitor Cells’, in Electric Vehicle Batteries: Moving from Research towards In-novation, E. Briec and B. Müller, Eds, in Lecture Notes in Mobility. , Cham: Springer Internation-al Publishing, 2015, pp. 33–43. doi: 10.1007/978-3-319-12706-4_3.

[80] H. Tu, M. Zhu, B. Duan, and L. Zhang, ‘Recent Progress in High-Strength and Robust Regenerated Cellulose Materials’, Adv. Mater., vol. 33, no. 28, p. 2000682, July 2021, doi: 10.1002/adma.202000682.

[81] X. Wang, W. Zheng, H. Zhao, J. Li, S. Chen, and F. Xu, ‘Robust and High-Wettability Cellulose Separators with Molecule-Reassembled Nano-Cracked Structures for High-Performance Supercapacitors’, Nano-Micro Lett., vol. 17, no. 1, p. 153, Dec. 2025, doi: 10.1007/s40820-025-01650-2.

[82] D. Xu, G. Teng, Y. Heng, Z. Chen, and D. Hu, ‘Eco-friendly and thermally stable cellu-lose film prepared by phase inversion as supercapacitor separator’, Mater. Chem. Phys., vol. 249, p. 122979, July 2020, doi: 10.1016/j.matchemphys.2020.122979.

[83] ‘Characteristics of Separator Materials for Supercapacitors | springerprofessional.de’. Accessed: Dec. 16, 2025. [Online]. Available: https://link.springer.com/chapter/10.1007/978-3-030-43009-2_11

[84] H. Wu, H. Huang, Y. Xu, F. Xu, and X. Zhang, ‘Ultrathin separator with efficient ion transport and superior stability prepared from cotton cellulose for advanced supercapacitors’, Chem. Eng. J., vol. 470, p. 144089, Aug. 2023, doi: 10.1016/j.cej.2023.144089.

[85] L. Yao et al., ‘Structural pseudocapacitors with reinforced interfaces to increase multi-functional efficiency’, Sci. Adv., vol. 9, no. 25, p. eadh0069, June 2023, doi: 10.1126/sci-adv.adh0069.

[86] D. Zhao et al., ‘High Performance, Flexible, Solid-State Supercapacitors Based on a Renewable and Biodegradable Mesoporous Cellulose Membrane’, Adv. Energy Mater., vol. 7, no. 18, p. 1700739, Sept. 2017, doi: 10.1002/aenm.201700739.

[87] C. Mevada et al., ‘A 3D-printed fully biocompatible supercapacitor’, J. Mater. Chem. A, vol. 12, no. 36, pp. 24357–24369, 2024, doi: 10.1039/D4TA02944E.

[88] A. Abdisattar et al., ‘Recent advances and challenges of current collectors for supercapacitors’, Electrochem. Commun., vol. 142, p. 107373, Sept. 2022, doi: 10.1016/j.elecom.2022.107373.

[89] K. K. Kar, Ed., Handbook of Nanocomposite Supercapacitor Materials III: Selection, vol. 313. in Springer Series in Materials Science, vol. 313. Cham: Springer International Publishing, 2021. doi: 10.1007/978-3-030-68364-1.

[90] K. K. Kar, Ed., Handbook of Nanocomposite Supercapacitor Materials I: Characteristics, vol. 300. in Springer Series in Materials Science, vol. 300. Cham: Springer International Publishing, 2020. doi: 10.1007/978-3-030-43009-2.

[91] J. Yu et al., ‘Metallic Fabrics as the Current Collector for High-Performance Graphene-Based Flexible Solid-State Supercapacitor’, ACS Appl. Mater. Interfaces, vol. 8, no. 7, pp. 4724–4729, Feb. 2016, doi: 10.1021/acsami.5b12180.

[92] A. Tanwilaisiri, Y. Xu, D. Harrison, J. Fyson, and M. Arier, ‘A Study of Metal Free Supercapacitors Using 3D Printing’, Int. J. Precis. Eng. Manuf., vol. 19, no. 7, pp. 1071–1079, July 2018, doi: 10.1007/s12541-018-0127-7.

[93] M. Arvani, J. Keskinen, D. Lupo, and M. Honkanen, ‘Current collectors for low re-sistance aqueous flexible printed supercapacitors’, J. Energy Storage, vol. 29, p. 101384, June 2020, doi: 10.1016/j.est.2020.101384.

[94] M. Muthu Balasubramanian, M. Subramani, D. Murugan, and S. Ponnusamy, ‘Groundnut shell–derived porous carbon-based supercapacitor with high areal mass loading using carbon

cloth as current collector', Ionics, vol. 26, no. 12, pp. 6297–6308, Dec. 2020, doi: 10.1007/s11581-020-03754-8.

[95] R. Quintero, D. Y. Kim, K. Hasegawa, Y. Yamada, A. Yamada, and S. Noda, 'Carbon nanotube 3D current collectors for lightweight, high performance and low cost supercapacitor electrodes', RSC Adv., vol. 4, no. 16, p. 8230, 2014, doi: 10.1039/c3ra47517d.

[96] Y. Khan, A. Thielens, S. Muin, J. Ting, C. Baumbauer, and A. C. Arias, 'A New Frontier of Printed Electronics: Flexible Hybrid Electronics', Adv. Mater., vol. 32, no. 15, p. 1905279, Apr. 2020, doi: 10.1002/adma.201905279.

[97] K. Tufail Chaudhary, 'Thin Film Deposition: Solution Based Approach', in Thin Films, A. Esther Ares, Ed., IntechOpen, 2021. doi: 10.5772/intechopen.94455.

[98] Z. Bo et al., 'Ultrathick MoS2 Films with Exceptionally High Volumetric Capacitance', Adv. Energy Mater., vol. 12, no. 11, p. 2103394, Mar. 2022, doi: 10.1002/aenm.202103394.

[99] L. K. Bommineedi, N. Upadhyay, and R. Minnes, 'Screen Printing: An Ease Thin Film Technique', in Simple Chemical Methods for Thin Film Deposition, B. R. Sankapal, A. Ennaoui, R. B. Gupta, and C. D. Lokhande, Eds, Singapore: Springer Nature Singapore, 2023, pp. 449–507. doi: 10.1007/978-981-99-0961-2_11.

[100] J. Liang, B. Tian, S. Li, C. Jiang, and W. Wu, 'All-Printed MnHCF-MnO x -Based High-Performance Flexible Supercapacitors', Adv. Energy Mater., vol. 10, no. 12, p. 2000022, Mar. 2020, doi: 10.1002/aenm.202000022.

[101] H. Li, S. Liu, X. Li, Z.-S. Wu, and J. Liang, 'Screen-printing fabrication of high volumetric energy density micro-supercapacitors based on high-resolution thixotropic-ternary hybrid interdigital micro-electrodes', Mater. Chem. Front., vol. 3, no. 4, pp. 626–635, 2019, doi: 10.1039/C8QM00639C.

[102] N. Saengchairat, T. Tran, and C.-K. Chua, 'A review: additive manufacturing for active electronic components', Virtual Phys. Prototyp., vol. 12, no. 1, pp. 31–46, Jan. 2017, doi: 10.1080/17452759.2016.1253181.

[103] G. Liu, S. Peng, F. Hou, X. Wang, and B. Fang, 'Preparation and Performance Study of the Anodic Catalyst Layer via Doctor Blade Coating for PEM Water Electrolysis', Membranes, vol. 13, no. 1, p. 24, Dec. 2022, doi: 10.3390/membranes13010024.

[104] G. C. Patil, 'Doctor Blade: A Promising Technique for Thin Film Coating', in Simple Chemical Methods for Thin Film Deposition, B. R. Sankapal, A. Ennaoui, R. B. Gupta, and C. D. Lokhande, Eds, Singapore: Springer Nature Singapore, 2023, pp. 509–530. doi: 10.1007/978-981-99-0961-2_12.

[105] Z. He, Z. Zhang, and S. Bi, 'Tailoring the molecular weight of polymer additives for organic semiconductors', Mater. Adv., vol. 3, no. 4, pp. 1953–1973, 2022, doi: 10.1039/D1MA00964H.

[106] Y. Xi et al., 'Stencil mask defined doctor blade printing of organic single crystal arrays for high-performance organic field-effect transistors', Mater. Chem. Front., vol. 5, no. 7, pp. 3236–3245, 2021, doi: 10.1039/D1QM00097G.

[107] Y. Kang, K. Lee, and T. Liu, 'The effect of polymer additives on the performance of a two-roll coater', J. Appl. Polym. Sci., vol. 43, no. 6, pp. 1187–1195, Sept. 1991, doi: 10.1002/app.1991.070430620.

[108] G. Regmi et al., 'Perspectives of chalcopyrite-based CIGSe thin-film solar cell: a review', J. Mater. Sci. Mater. Electron., vol. 31, no. 10, pp. 7286–7314, May 2020, doi: 10.1007/s10854-020-03338-2.

[109] D. A. Aikens, 'Electrochemical methods, fundamentals and applications', J. Chem. Educ., vol. 60, no. 1, p. A25, Jan. 1983, doi: 10.1021/ed060pA25.1.

[110] A. A. Mohamad, 'Cyclic voltammetry of hybrid supercapacitors: A characteriza-tion review', Inorg. Chem. Commun., vol. 172, p. 113677, Feb. 2025, doi: 10.1016/j.inoche.2024.113677.

[111] 'Supercapacitor Calculations: Capacitance, Energy, Power Density', studylib.net. Accessed: Dec. 16, 2025. [Online]. Available: https://studylib.net/doc/18049885/calculation-the-specific-capacitance-can-be-calculated-fr ...

[112] L. Nánai and K. Hernadi, 'Carbon-Based Electrodes for Supercapacitors, with a Focus on Carbon Nanotubes—A Brief Overview', Materials, vol. 18, no. 22, p. 5215, Nov. 2025, doi: 10.3390/ma18225215.

[113] Y. Zhang, X. Li, Z. Li, and F. Yang, ‘Evaluation of electrochemical performance of supercapacitors from equivalent circuits through cyclic voltammetry and galvanostatic charge/discharge’, J. Energy Storage, vol. 86, p. 111122, May 2024, doi: 10.1016/j.est.2024.111122.

[114] N. H. N. Azman, M. S. Mamat Mat Nazir, L. H. Ngee, and Y. Sulaiman, ‘Gra-phene-based ternary composites for supercapacitors’, Int. J. Energy Res., vol. 42, no. 6, pp. 2104–2116, May 2018, doi: 10.1002/er.4001.

[115] Shanghai Key Lab of Chemical Assessment and Sustainability, School of Chemical Science and Engineering, Tongji University, Shanghai 200092, China et al., ‘Pulsed Laser Deposition of NiSe2 Film on Carbon Nanotubes for High-Performance Supercapacitor’, Eng. Sci., 2018, doi: 10.30919/es8d668.

[116] Z. U. Rehman et al., ‘La0.75Sr0.25Cr0.5Mn0.5O3 perovskite developed for supercapacitor applications’, J. Energy Storage, vol. 32, p. 101951, Dec. 2020, doi: 10.1016/j.est.2020.101951.

[117] J. I. Goldstein, D. E. Newbury, J. R. Michael, N. W. M. Ritchie, J. H. J. Scott, and D. C. Joy, Scanning Electron Microscopy and X-Ray Microanalysis. New York, NY: Springer New York, 2018. doi: 10.1007/978-1-4939-6676-9.

[118] S. Bhattacharya and A. Acharya, ‘Experimental tools for characterizations of glass nanocomposites containing metal oxides’, in Metal Oxide Glass Nanocomposites, Else-vier, 2020, pp. 51–75. doi: 10.1016/B978-0-12-817458-6.00004-4.

[119] S.-H. Kim, ‘Engineering impurities in colloidal nanostructures used in “green hydrogen” generation’, RWTH Aachen University, 2021. doi: 10.18154/RWTH-2021-05784.

[120] D. B. Williams and C. B. Carter, Transmission Electron Microscopy. Boston, MA: Springer US, 2009. doi: 10.1007/978-0-387-76501-3.

[121] Z. Li, L. Deng, I. A. Kinloch, and R. J. Young, ‘Raman spectroscopy of carbon materials and their composites: Graphene, nanotubes and fibres’, Prog. Mater. Sci., vol. 135, p. 101089, June 2023, doi: 10.1016/j.pmatsci.2023.101089.

[122] L. Gustavo Cançado et al., ‘Disentangling contributions of point and line defects in the Raman spectra of graphene-related materials’, 2D Mater., vol. 4, no. 2, p. 025039, Feb. 2017, doi: 10.1088/2053-1583/aa5e77.

[123] ‘What is Raman Spectroscopy? Raman Spectroscopy Principles’. Accessed: Dec. 16, 2025. [Online]. Available: https://www.edinst.com/resource/what-is-raman-spectroscopy/

[124] G. G. Politano and C. Versace, ‘Spectroscopic Ellipsometry: Advancements, Applications and Future Prospects in Optical Characterization’, Spectrosc. J., vol. 1, no. 3, pp. 163–181, Dec. 2023, doi: 10.3390/spectroscj1030014.

[125] P. June 11 and 2013, ‘Spectroscopic Ellipsometry Characterization of Thin Films Used in the Food Packaging Industry’. Accessed: Dec. 16, 2025. [Online]. Available: https://www.americanlaboratory.com/914-Application-Notes/138874-Spectroscopic-Ellipsometry-Characterization-of-Thin-Films-Used-in-the-Food-Packaging-Industry/

[126] ‘X-ray Diffraction (XRD) - Overview’. Accessed: Dec. 16, 2025. [Online]. Avai-lable: https://www.malvernpanalytical.com/en/products/technology/xray-analysis/x-ray-diffraction

[127] ‘X-ray diffraction (XRD)’. Accessed: Dec. 16, 2025. [Online]. Available: https://rigaku.com/resources/techniques/x-ray-diffraction-xrd

[128] ‘X-ray diffraction (XRD) basics and application’, Chemistry LibreTexts. Acces-sed: Dec. 16, 2025. [Online]. Available: https://chem.libretexts.org/Courses/Franklin_and_Marshall_College/Introduction_to_Materials_Characterization__CHM_412_Collaborative_Text/Diffraction_Techniques/X-ray_diffraction_(XRD)_basics_and_application

[129] H. Shi, ‘Activated carbons and double layer capacitance’, Electrochimica Acta, vol. 41, no. 10, pp. 1633–1639, June 1996, doi: 10.1016/0013-4686(95)00416-5.

[130] W. Zhang, J. Wang, L. Bao, Z. Gao, and J. Yu, ‘Nanopores created by carbon onion conductive agent providing enhanced capacitance in supercapacitors’, Diam. Relat. Mater., vol. 96, pp. 231–236, June 2019, doi: 10.1016/j.diamond.2019.05.015.

[131] Y. Yang et al., ‘Three-Dimensional Thin Film for Lithium-Ion Batteries and Supercapacitors’, ACS Nano, vol. 8, no. 7, pp. 7279–7287, July 2014, doi: 10.1021/nn502341x.

[132] K. L. Van Aken, M. Beidaghi, and Y. Gogotsi, ‘Formulation of Ionic-Liquid Electrolyte To Expand the Voltage Window of Supercapacitors’, Angew. Chem. Int. Ed., vol. 54, no. 16, pp. 4806–4809, Apr. 2015, doi: 10.1002/anie.201412257.

[133] F. W. Richey, B. Dyatkin, Y. Gogotsi, and Y. A. Elabd, ‘Ion Dynamics in Porous Carbon Electrodes in Supercapacitors Using in Situ Infrared Spectroelectrochemistry’, J. Am. Chem. Soc., vol. 135, no. 34, pp. 12818–12826, Aug. 2013, doi: 10.1021/ja406120e.

[134] P. Huang et al., ‘On-chip micro-supercapacitors for operation in a wide temperature range’, Electrochem. Commun., vol. 36, pp. 53–56, Nov. 2013, doi: 10.1016/j.elecom.2013.09.003.

[135] Y. Gao et al., ‘Chemical activation of carbon nano-onions for high-rate supercapacitor electrodes’, Carbon, vol. 51, pp. 52–58, Jan. 2013, doi: 10.1016/j.carbon.2012.08.009.

[136] S. Fleischmann et al., ‘Tuning pseudocapacitive and battery-like lithium intercalation in vanadium dioxide/carbon onion hybrids for asymmetric supercapacitor anodes’, J. Ma-ter. Chem. A, vol. 5, no. 25, pp. 13039–13051, 2017, doi: 10.1039/C7TA02564E.

[137] Q. Wang, Z. H. Wen, and J. H. Li, ‘A Hybrid Supercapacitor Fabricated with a Carbon Nanotube Cathode and a TiO2 –B Nanowire Anode’, Adv. Funct. Mater., vol. 16, no. 16, pp. 2141–2146, Oct. 2006, doi: 10.1002/adfm.200500937.

[138] G. Feng, S. Li, J. S. Atchison, V. Presser, and P. T. Cummings, ‘Molecular Insights into Carbon Nanotube Supercapacitors: Capacitance Independent of Voltage and Temperature’, J. Phys. Chem. C, vol. 117, no. 18, pp. 9178–9186, May 2013, doi: 10.1021/jp403547k.

[139] C. Masarapu, H. F. Zeng, K. H. Hung, and B. Wei, ‘Effect of Temperature on the Capacitance of Carbon Nanotube Supercapacitors’, ACS Nano, vol. 3, no. 8, pp. 2199–2206, Aug. 2009, doi: 10.1021/nn900500n.

[140] X. Li, J. Rong, and B. Wei, ‘Electrochemical Behavior of Single-Walled Carbon Nanotube Supercapacitors under Compressive Stress’, ACS Nano, vol. 4, no. 10, pp. 6039–6049, Oct. 2010, doi: 10.1021/nn101595y.

[141] C. Du, J. Yeh, and N. Pan, ‘High power density supercapacitors using locally aligned carbon nanotube electrodes’, Nanotechnology, vol. 16, no. 4, pp. 350–353, Apr. 2005, doi: 10.1088/0957-4484/16/4/003.

[142] N. He et al., ‘Pyrolytic-carbon coating in carbon nanotube foams for better performance in supercapacitors’, J. Power Sources, vol. 343, pp. 492–501, Mar. 2017, doi: 10.1016/j.jpowsour.2017.01.091.

[143] K. Yang et al., ‘Ti3C2T /carbon nanotube/porous carbon film for flexible supercapacitor’, Chem. Eng. J., vol. 427, p. 132002, Jan. 2022, doi: 10.1016/j.cej.2021.132002.

[144] S.-L. Chou, J.-Z. Wang, S.-Y. Chew, H.-K. Liu, and S.-X. Dou, ‘Electrodeposition of MnO2 nanowires on carbon nanotube paper as free-standing, flexible electrode for supercapacitors’, Electrochem. Commun., vol. 10, no. 11, pp. 1724–1727, Nov. 2008, doi: 10.1016/j.elecom.2008.08.051.

[145] Y. Su and I. Zhitomirsky, ‘Hybrid MnO2/carbon nanotube-VN/carbon nanotube supercapacitors’, J. Power Sources, vol. 267, pp. 235–242, Dec. 2014, doi: 10.1016/j.jpowsour.2014.05.091.

[146] J. Chen et al., ‘Pulsed electrochemical fabrication of graphene/polypyrrole composite gel films for high performance and flexible supercapacitors’, Electrochimica Acta, vol. 361, p. 137036, Nov. 2020, doi: 10.1016/j.electacta.2020.137036.

[147] Z. Khanam, J. Liu, and S. Song, ‘Flexible graphene paper electrode prepared via polyvinyl alcohol-assisted shear-exfoliation for all-solid-state polymer supercapacitor application’, Electrochimica Acta, vol. 363, p. 137208, Dec. 2020, doi: 10.1016/j.electacta.2020.137208.

[148] L. Liu, Y. Yu, C. Yan, K. Li, and Z. Zheng, ‘Wearable energy-dense and power-dense supercapacitor yarns enabled by scalable graphene–metallic textile composite electrodes’, Nat. Commun., vol. 6, no. 1, p. 7260, June 2015, doi: 10.1038/ncomms8260.

[149] J. Yu et al., ‘Ultrahigh-rate wire-shaped supercapacitor based on graphene fiber’, Carbon, vol. 119, pp. 332–338, Aug. 2017, doi: 10.1016/j.carbon.2017.04.052.

[150] W. Zhao, M. Jiang, W. Wang, S. Liu, W. Huang, and Q. Zhao, ‘Flexible Transparent Supercapacitors: Materials and Devices’, Adv. Funct. Mater., vol. 31, no. 11, p. 2009136, Mar. 2021, doi: 10.1002/adfm.202009136.

[151] J. Yan, Z. Fan, T. Wei, W. Qian, M. Zhang, and F. Wei, ‘Fast and reversible surface redox reaction of graphene–MnO2 composites as supercapacitor electrodes’, Carbon, vol. 48, no. 13, pp. 3825–3833, Nov. 2010, doi: 10.1016/j.carbon.2010.06.047.

[152] G. Wu, X. Yang, C. Hou, Y. Li, Q. Zhang, and H. Wang, ‘High Volumetric Energy Density Asymmetric Fibrous Supercapacitors with Coaxial Structure Based on Graphene/MnO2

Hybrid Fibers', ChemElectroChem, vol. 7, no. 22, pp. 4641–4648, Nov. 2020, doi: 10.1002/celc.202001139.

[153] D. W. Kim, S. M. Jung, and H. Y. Jung, 'Long term thermostable supercapacitor using in-situ SnO2 doped porous graphene aerogel', J. Power Sources, vol. 448, p. 227422, Feb. 2020, doi: 10.1016/j.jpowsour.2019.227422.

[154] R. Shrestha and N. Phulara, 'Review on Activated Carbon for Supercapacitors', Semicond. Sci. Inf. Devices, vol. 5, no. 2, pp. 11–18, Jan. 2024, doi: 10.30564/ssid.v5i2.6171.

[155] Y. Xu et al., 'Recent progress in electrode materials for micro-supercapacitors', iScience, vol. 27, no. 2, p. 108786, Feb. 2024, doi: 10.1016/j.isci.2024.108786.

[156] F. Zhang, G. Song, D. Gandla, Y. Ein-Eli, and D. Q. Tan, 'Synergy of Oxygen Plasma and Al2O3 Atomic Layer Deposition on Improved Electrochemical Stability of Activated Carbon-Based Supercapacitor', Front. Energy Res., vol. 9, p. 653203, Apr. 2021, doi: 10.3389/fenrg.2021.653203.

[157] G. Obey, M. Adelaide, and R. Ramaraj, 'Biochar derived from non-customized mat-amba fruit shell as an adsorbent for wastewater treatment', J. Bioresour. Bioprod., vol. 7, no. 2, pp. 109–115, May 2022, doi: 10.1016/j.jobab.2021.12.001.

[158] J. Jjagwe, P. W. Olupot, E. Menya, and H. M. Kalibbala, 'Synthesis and Application of Granular Activated Carbon from Biomass Waste Materials for Water Treatment: A Review', J. Bioresour. Bioprod., vol. 6, no. 4, pp. 292–322, Nov. 2021, doi: 10.1016/j.jobab.2021.03.003.

[159] H. Pourkheirollah et al., 'Enhancing specific capacitance and energy density in printed supercapacitors: The role of activated wood carbon and electrolyte dynamics', Carbon Trends, vol. 18, p. 100436, Jan. 2025, doi: 10.1016/j.cartre.2024.100436.

[160] J. Piwek, A. Platek, K. Fic, and E. Frackowiak, 'Carbon-based electrochemical capacitors with acetate aqueous electrolytes', Electrochimica Acta, vol. 215, pp. 179–186, Oct. 2016, doi: 10.1016/j.electacta.2016.08.061.

[161] H. Yoon et al., 'Effect of activated carbon electrode material characteristics on hardness control performance of membrane capacitive deionization', RSC Adv., vol. 13, no. 45, pp. 31480–31486, 2023, doi: 10.1039/D3RA05615E.

[162] H. M. Saif et al., 'Activated carbons for flow electrode capacitive deionization (FCDI) – Morphological, electrochemical and rheological analysis', Desalination, vol. 602, p. 118638, May 2025, doi: 10.1016/j.desal.2025.118638.

[163] R. Wang, X. Li, Z. Nie, Y. Zhao, and H. Wang, 'Metal/Metal Oxide Nanoparticles-Composited Porous Carbon for High-Performance Supercapacitors', J. Energy Storage, vol. 38, p. 102479, June 2021, doi: 10.1016/j.est.2021.102479.

[164] P. Yadav, C. Tyagi, and N. M. Saidi, 'A brief review: transition metal oxides with carbon composite materials for high-performance supercapacitor, applications, fabrication methods, and future perspective', Ionics, vol. 31, no. 7, pp. 6695–6718, July 2025, doi: 10.1007/s11581-025-06393-z.

[165] J. Y. Lee, K. Liang, K. H. An, and Y. H. Lee, 'Nickel oxide/carbon nanotubes nanocomposite for electrochemical capacitance', Synth. Met., vol. 150, no. 2, pp. 153–157, Apr. 2005, doi: 10.1016/j.synthmet.2005.01.016.

[166] S. Veeresh et al., 'Graphene oxide/cobalt oxide nanocomposite for high-performance electrode for supercapacitor application', J. Energy Storage, vol. 52, p. 104715, Aug. 2022, doi: 10.1016/j.est.2022.104715.

[167] X.-C. Dong et al., '3D Graphene–Cobalt Oxide Electrode for High-Performance Supercapacitor and Enzymeless Glucose Detection', ACS Nano, vol. 6, no. 4, pp. 3206–3213, Apr. 2012, doi: 10.1021/nn300097q.

[168] T. Huang, Z. Qiu, D. Wu, and Z. Hu, 'Bamboo-Based Activated Carbon @ MnO2 Nanocomposites for Flexible High-Performance Supercapacitor Electrode Materials', Int. J. Electrochem. Sci., vol. 10, no. 8, pp. 6312–6323, Aug. 2015, doi: 10.1016/S1452-3981(23)06721-4.

[169] Q. Wang, Y. Zhang, J. Xiao, H. Jiang, T. Hu, and C. Meng, 'Copper ox-ide/cuprous oxide/hierarchical porous biomass-derived carbon hybrid composites for high-performance supercapacitor electrode', J. Alloys Compd., vol. 782, pp. 1103–1113, Apr. 2019, doi: 10.1016/j.jallcom.2018.12.235.

[170] X. Jiang, G. Shi, G. Wang, P. Mishra, J. Du, and Y. Zhang, 'Fe2O3/hemp straw-based porous carbon composite for supercapacitor electrode materials', Ionics, vol. 26, no. 8, pp. 4039–4051, Aug. 2020, doi: 10.1007/s11581-020-03547-z.

[171] Poonam, K. Sharma, A. Arora, and S. K. Tripathi, ‘Review of supercapacitors: Materials and devices’, J. Energy Storage, vol. 21, pp. 801–825, Feb. 2019, doi: 10.1016/j.est.2019.01.010.

[172] A. Ajith, E. Thomas, C. H. Suresh, and R. R. Philip, ‘Advances and strategies in nanoarchitectured TiO2-based electrodes for supercapacitors’, J. Energy Storage, vol. 111, p. 115289, Mar. 2025, doi: 10.1016/j.est.2025.115289.

[173] J. Zhi, H. Cui, Z. Wang, and F. Huang, ‘Surface confined titania redox couple for ultrafast energy storage’, Mater. Horiz., vol. 5, no. 4, pp. 691–698, 2018, doi: 10.1039/C8MH00112J.

[174] A. Mir et al., ‘Strategic Ti3+ incorporation in TiO_2 nanotube arrays via microwave-promoted borohydride reduction for high-performance energy storage’, Electrochimica Acta, vol. 546, p. 147743, Jan. 2026, doi: 10.1016/j.electacta.2025.147743.

[175] O. D. Saliu, M. Mamo, P. Ndungu, and J. Ramontja, ‘Starch built TiO2 nanoarchitecture with mixed anatase and rutile phase for high energy density supercapacitor electrode’, J. Energy Storage, vol. 49, p. 104155, May 2022, doi: 10.1016/j.est.2022.104155.

[176] R. Kumar, B. K. Singh, A. Soam, S. Parida, V. Sahajwalla, and P. Bhargava, ‘In situ carbon-supported titanium dioxide (ICS-TiO2) as an electrode material for high perfor-mance supercapacitors’, Nanoscale Adv., vol. 2, no. 6, pp. 2376–2386, 2020, doi: 10.1039/D0NA00014K.

[177] R. Bortamuly et al., ‘Titania supported bio-derived activated carbon as an electrode material for high-performance supercapacitors’, J. Energy Storage, vol. 42, p. 103144, Oct. 2021, doi: 10.1016/j.est.2021.103144.

[178] M. Leskelä and M. Ritala, ‘Atomic layer deposition (ALD): from precursors to thin film structures’, Thin Solid Films, vol. 409, no. 1, pp. 138–146, Apr. 2002, doi: 10.1016/S0040-6090(02)00117-7.

[179] S. Sirviö, ‘Characterization of Atomic Layer Deposited Thin Films: Conformality in High Aspect Ratio Pores and the Electrical Properties of Capacitors’, 2014, Accessed: Dec. 16, 2025. [Online]. Available: https://aaltodoc.aalto.fi/handle/123456789/14207

[180] R. L. P. Ommen J. Ruud van, English: Illustration of the ALD temperature window concept. Inside the ALD window (gray area), the process fulfils the criteria of ALD. Outside the ALD window, the process fails to fulfil the ALD criteria, because of: (L1) reversible multilayer adsorption (physisorption); (L2) activated chemisorption, not saturated; (H1) thermal decomposition of the reactant; or (H2) desorption due to reversible reactions. Adapted from T. Suntola, Materials Science Reports, Vol. 4, Issue 5, 1989, Pages 261-312, Figure 12, https://doi.org/10.1016/S0920-2307(89)80006-4 . 2020. Accessed: Dec. 16, 2025. [Online]. Available: https://commons.wikimedia.org/wiki/File:Illustration_of_the_ALD_temperature_window.png

[181] D. Gandla, G. Song, C. Wu, Y. Ein-Eli, and D. Q. Tan, ‘Atomic Layer Deposition (ALD) of Alumina over Activated Carbon Electrodes Enabling a Stable 4 V Supercapacitor Operation’, ChemistryOpen, vol. 10, no. 4, pp. 402–407, Apr. 2021, doi: 10.1002/open.202000352.

[182] K. Hong, M. Cho, and S. O. Kim, ‘Atomic Layer Deposition Encapsulated Activated Carbon Electrodes for High Voltage Stable Supercapacitors’, ACS Appl. Mater. Interfac-es, vol. 7, no. 3, pp. 1899–1906, Jan. 2015, doi: 10.1021/am507673j.

[183] J. S. Daubert et al., ‘Effect of Meso- and Micro-Porosity in Carbon Electrodes on Atomic Layer Deposition of Pseudocapacitive V2 O5 for High Performance Supercapaci-tors’, Chem. Mater., vol. 27, no. 19, pp. 6524–6534, Oct. 2015, doi: 10.1021/acs.chemmater.5b01602.

[184] C. Wu et al., ‘Enhanced Electrochemical Performance of Supercapacitors via Atomic Layer Deposition of ZnO on the Activated Carbon Electrode Material’, Molecules, vol. 26, no. 14, p. 4188, July 2021, doi: 10.3390/molecules26144188.

[185] D. Q. Tan, G. Song, D. Gandla, and F. Zhang, ‘Commonalities of Atomic Layer Deposition of Oxide Coatings on Activated Carbons for 3.5 V Electric Double Layer Supercapacitors’, Front. Energy Res., vol. 8, p. 596062, Nov. 2020, doi: 10.3389/fenrg.2020.596062.

[186] ‘IEC 62391-1:2006’. Accessed: Dec. 16, 2025. [Online]. Available: https://webstore.iec.ch/en/publication/6971

[187] S. Lehtimäki, A. Railanmaa, J. Keskinen, M. Kujala, S. Tuukkanen, and D. Lupo, ‘Performance, stability and operation voltage optimization of screen-printed aqueous supercapacitors’, Sci. Rep., vol. 7, no. 1, p. 46001, Apr. 2017, doi: 10.1038/srep46001.

[188] C. R. Birkl, D. F. Frost, A. M. Bizeray, R. R. Richardson, and D. A. Howey, ‘Modular converter system for low-cost off-grid energy storage using second life li-ion batter-ies’, in IEEE

Global Humanitarian Technology Conference (GHTC 2014), San Jose, CA: IEEE, Oct. 2014, pp. 192–199. doi: 10.1109/GHTC.2014.6970281.

[189] J. García-Torres, ‘Fabrication and Characterization of Flexible Fiber-Shape Supercapacitors: Learning Basic Concepts of Materials Chemistry and Electrochemistry Applied to Energy Storage’, J. Chem. Educ., vol. 102, no. 2, pp. 821–828, Feb. 2025, doi: 10.1021/acs.jchemed.4c01217.

[190] M. Ritala, M. Leskelä, E. Nykänen, P. Soininen, and L. Niinistö, ‘Growth of titanium dioxide thin films by atomic layer epitaxy’, Thin Solid Films, vol. 225, no. 1–2, pp. 288–295, Mar. 1993, doi: 10.1016/0040-6090(93)90172-L.

[191] H. Gul, A.-H. A. Shah, and S. Bilal, ‘Achieving Ultrahigh Cycling Stability and Extended Potential Window for Supercapacitors through Asymmetric Combination of Conductive Polymer Nanocomposite and Activated Carbon’, Polymers, vol. 11, no. 10, p. 1678, Oct. 2019, doi: 10.3390/polym11101678.

[192] F. Z. Amir and J. C. Willier, ‘Achieving enhanced capacitance retention in an extended potential window for pristine co-HAB metal-organic framework supercapacitors’, FlatChem, vol. 51, p. 100869, May 2025, doi: 10.1016/j.flatc.2025.100869.

[193] M. Fawad Khan et al., ‘Novel MoS2-sputtered NiCoMg MOFs for high-performance hybrid supercapacitor applications’, Sep. Purif. Technol., vol. 310, p. 123101, Apr. 2023, doi: 10.1016/j.seppur.2023.123101.

[194] J. Turner, H. C. Aspinall, S. Rushworth, and K. Black, ‘A hybrid nanoparti-cle/alkoxide ink for inkjet printing of TiO2 : a templating effect to form anatase at 200 °C’, RSC Adv., vol. 9, no. 67, pp. 39143–39146, 2019, doi: 10.1039/C9RA06119C.

[195] ‘Grazing-Incidence-X-ray-Diffraction-GiXRD-A-Practical-Guide-for-Thin-Film-Characterization-Using-Rigaku-SmartLab-SE.pdf’. Accessed: Dec. 16, 2025. [Online]. Available: https://physlab.org/wp-content/uploads/2025/05/Grazing-Incidence-X-ray-Diffraction-GiXRD-A-Practical-Guide-for-Thin-Film-Characterization-Using-Rigaku-SmartLab-SE.pdf

[196] Yu B, Zhang J, Yang Y, Yu D, Mai Y, Chen X. Influences of deposition conditions on atomic layer deposition films for enhanced performance in perovskite solar cells. Energy Materials [Online]. 2024 Jan 1; Available from: https://doi.org/10.20517/energymater.2023.150